TECHNISCHE UNIVERSITÄT DRESDEN

Fractal Dimensions in Classical and Quantum Mechanical Open Chaotic Systems

Dissertationsschrift zur Erlangung

des wissenschaftlichen Grades

Doctor rerum naturalium

Vorgelegt von

Moritz SCHÖNWETTER

geboren am 13. August 1984 in Dachau

Angefertigt in der Arbeitsgruppe

Dynamical Systems and Social Dynamics

am Max-Planck-Institut für Physik komplexer Systeme in Dresden

Juni 2016

Abstract

Fractal Dimensions in Classical and Quantum Mechanical Open Chaotic Systems

Fractals have long been recognized to be a characteristic feature arising from chaotic dynamics; be it in the form of strange attractors, of fractal boundaries around basins of attraction, or of fractal and multifractal distributions of asymptotic measures in open systems. In this thesis we study fractal and multifractal measure distributions in leaky Hamiltonian systems. Leaky systems are created by introducing a fully or partially transparent hole in an otherwise closed system, allowing trajectories to escape or lose some of their intensity. This dynamics results in intricate (multi)fractal distributions of the surviving trajectories. These systems are suitable models for experimental setups such as optical microcavities or microwave resonators. In this thesis we perform an improved investigation of the fractality in these systems using the concept of effective dimensions. They are defined as the dimensions far from the usually considered asymptotics of infinite evolution time t, infinite sample size S, and infinite resolution (infinitesimal box-size ε). Yet, as we show, effective dimensions can be considered as intrinsic to the dynamics of the system. We present a detailed discussion of the behaviour of the numerically observed dimension $D_{\mathrm{obs}}(S, t, \varepsilon)$. We show that the three parameters can be expressed in terms of limiting length scales that define the parameter ranges in which $D_{\mathrm{obs}}(S, t, \varepsilon)$ is an effective dimension of the system. We provide dynamical and statistical arguments for the dependence of these scales on S, t, and ε in strongly chaotic systems and show that the knowledge of the scales allows us to define meaningful effective dimensions. We apply our results to three main fields. In the context of numerical algorithms to calculate dimensions, we show that our findings help to numerically find the range of box sizes leading to accurate results. We further show that they allow us to minimize the computational cost by providing estimates of the required sample-size and iteration time needed. A second application field of our results is systems exhibiting non-trivial dependencies of the effective dimension D_{eff} on t and ε. We numerically explore this in weakly chaotic leaky systems. There, our findings provide insight into the dynamics of the systems, since deviations from our predictions based on strongly chaotic systems at a given parameter range are a sign that the stickiness inherent to such systems needs to be taken into account in that range. Lastly, we show that in quantum analogues of chaotic maps with a partial leak, a related effective dimension can be used to explain the numerically observed deviation from the predictions provided by the fractal Weyl law for systems with fully absorbing leaks. Here, we provide an analytical description of the expected scaling based on the classical dynamics of the system and compare it with numerical results obtained in the studied quantum maps.

Zusammenfassung

Fraktale Dimensionen in Klassischen und Quantenmechanischen Chaotischen Systemen

Es ist seit langem bekannt, dass Fraktale eine charakteristische Begleiterscheinung chaotischer Dynamik sind. Sie treten in Form von seltsamen Attraktoren, von fraktalen Begrenzungen der Einzugsbereiche von Attraktoren oder von fraktalen und multifraktalen Verteilungen asymptotischer Maße in offenen Systemen auf. In dieser Arbeit betrachten wir fraktal und multifraktal verteilte Maße in geöffneten hamiltonschen Systemen. Geöffnete Systeme werden dadurch erzeugt, dass man ein völlig oder teilweise transparentes Loch im Phasenraum definiert, durch das Trajektorien entkommen können oder in dem sie einen Teil ihrer Intensität verlieren. Die Dynamik in solchen Systemen erzeugt komplexe (multi)fraktale Verteilungen der verbleibenden Trajektorien, beziehungsweise ihrer Intensitäten. Diese Systeme sind zur Modellierung experimenteller Aufbauten, wie zum Beispiel optischer Mikrokavitäten oder Mikrowellenresonatoren, geeignet. In dieser Arbeit führen wir eine verbesserte Untersuchung der Fraktalität in derartigen Systemen durch, die auf dem Konzept der effektiven Dimensionen beruht. Diese sind als die Dimensionen definiert, die weit weg von den üblicherweise betrachteten Limites unendlicher Iterationszeit t, unendlicher Stichprobengröße S und unendlicher Auflösung, also infinitesimaler Boxgröße ε auftreten. Dennoch können effektive Dimensionen, wie wir zeigen, als der Dynamik des Systems inhärent angesehen werden. Wir führen eine detaillierte Diskussion der numerisch beobachteten Dimension $D_{\mathrm{obs}}(S, t, \varepsilon)$ durch und zeigen, dass die drei Parameter S, t und ε in Form grenzwertiger Längenskalen ausgedrückt werden können, die die Parameterbereiche definieren, in denen $D_{\mathrm{obs}}(S, t, \varepsilon)$ den Wert einer effektiven Dimension des Systems annimmt. Wir beschreiben das Verhalten dieser Längenskalen in stark chaotischen Systemen als Funktionen von S, t und ε anhand statistischer Überlegungen und anhand von auf der Dynamik basierenden Aussagen. Weiterhin zeigen wir, dass das Wissen um diese Längenskalen die Definition aussagekräftiger effektiver Dimensionen ermöglicht. Wir wenden unsere Ergebnisse hauptsächlich in drei Bereichen an: Im Kontext numerischer Algorithmen zur Dimensionsberechnung zeigen wir, dass unsere Ergebnisse es erlauben, diejenigen ε-Bereiche zu finden, die zu korrekten Ergebnissen führen. Weiterhin zeigen wir, dass sie es uns erlauben, den Rechenaufwand zu minimieren, indem sie uns eine Abschätzung der benötigten Stichprobengröße und Iterationszeit ermöglichen. Ein zweiter Anwendungsbereich sind Systeme, die sich durch eine nichttriviale Abhängigkeit von D_{eff} von t und ε auszeichnen. Hier ermöglichen unsere Ergebnisse ein besseres Verständnis der Systeme, da Abweichungen von den Vorhersagen basierend auf der Annahme von starker Chaotizität ein Anzeichen dafür sind, dass im entsprechenden Parameterbereich die Eigenschaft dieser Systeme, dass Bereiche in ihrem Phasenraum Trajektorien für eine begrenzte Zeit einfangen können, relevant ist. Zuletzt zeigen wir, dass in quantenmechanischen Analoga chaotischer Abbildungen mit partiellen Öffnungen eine verwandte effektive Dimension genutzt werden kann, um die numerisch beobachteten Abweichungen vom fraktalen weyl'schen Gesetz für völlig transparente Öffnungen zu erklären. In diesem Zusammenhang zeigen wir eine analytische Beschreibung des erwarteten Skalierungsverhaltens auf, die auf der klassischen Dynamik des Systems basiert, und vergleichen sie mit numerischen Erkenntnissen, die wir über die Quantenabbildungen gewonnen haben.

Contents

Für Anna.

Chapter 1

Introduction

1.1 Motivation

Fractals and multifractals have long been a topic of interest in different fields from economics [Man04] to biology [Wes99, HRO02], medicine [VGL$^+$15, IAG$^+$99], solid state physics [Zaa10, CKP$^+$14], astronomy [AS81, LKK$^+$15], and many others. Their defining property is that they are self similar or at least qualitatively or statistically self similar on all scales. This self similarity can be quantified by assigning a fractal dimension [Man67]. One possible choice of defining such a fractal dimension is the box-counting dimension D_0 [Ott02]. Some fractals exhibit an even more complicated structure and are therefore not sufficiently characterised by a single fractal dimension. Instead, they are characterised by a full spectrum of fractal dimensions such as the Rényi dimensions D_q [Rén55] or the so called $f(\alpha)$ spectrum [HJK$^+$86b, HJK$^+$86a].

Some years after Mandelbrot publicised the term, attracting limiting sets of dynamical systems were found to be fractal; these strange attractors appear in systems used to model turbulence [RT71]. In the study of the same subject it was later realised that the fractal dimension of a strange attractor can be expressed in terms of the Lyapunov exponents of the system [FKYY83]. This so called Lyapunov-dimension is conjectured to be similar to the information dimension $D_{q=1}$ [Ott02] and it bridged the gap between a geometrical description of the invariant structure and its underlying dynamics. The dynamical systems mentioned so far have in common that they are dissipative and chaotic in the long-time asymptotic regime. Those conditions are, however, not necessary for the appearance of fractal structures. There is a class of systems which exhibit chaotic behaviour only on finite time scales; a phenomenon called transient chaos [LT11, Tél15].

Transient chaos was first studied in the context of crises [GOY82] and fractal boundaries [GOY83] but also commonly appears in open systems (e.g. chaotic scattering). For such systems a similar relation to the Kaplan-Yorke formula was found connecting the fractal dimension $D_{q=1}$ of the saddle with the Lyapunov exponent and the escape rate describing the exponential decay of the chaotic component [KG85]. But also in energy conserving systems, which are Hamiltonian and therefore do not have an attracting set, fractals appear when the systems are opened. In that case, the surviving set, or, in the case of a partially transparent leak, the asymptotic intensity distribution exhibit a (multi)fractal structure. By now fractality is recognised as a general signature of chaotic dynamics [Ott02, LT11, AVS09], although fractality does not necessarily imply chaos [GOPY84].

In this work we discuss Hamiltonian systems which have a leak somewhere within their phase space that either allows trajectories to escape or that absorbs some part of an intensity associated to the trajectory. This class of systems is especially interesting because such systems exhibit transient chaos, but, at the same time, they can be studied using numerically convenient volume preserving maps [Mei92]. Apart from their theoretical significance, these systems are also models for – amongst other physical phenomena [APT13b], such as, for example, reverberation in acoustics – the behaviour of optical cavities [WM08, CW15, SSFH16]. Such cavities are experimentally realised by embedding a disk made of a dielectric material with a refractive index n_1 within a larger disk of dielectric material with a different refractive index $n_2 < n_1$. On the interface between the two materials light rays are either reflected completely if the angle of incidence α fulfills

$$\alpha > \arcsin \frac{n_2}{n_1},$$

in which case the light ray stays within the disk, or transmitted at least partially, i.e., they can escape if their angle of incidence is steep enough. If the boundary shape of the inner disk is circular, such systems can support resonant electromagnetic whispering gallery modes that have very long life-times and a very narrow spectral width which makes this type of micro cavity useful for many optical applications [IM06]. For lasing applications, however, the isotropic emission pattern of such whispering gallery mode resonators is not desired, instead the emission ideally is unidirectional. An almost unidirectional far-field emission pattern is achieved by deforming the micro disk boundary appropriately. While most deformations do not produce the desired result, i.e., unidirectional emission with low spectral width, the limaçon shape was experimentally shown [WH06, SHW+09] to show a preferred direction of emission. In large enough billiards the light propagation can be described by ray dynamics in optical billiard which is chaotic for most shapes of the disk [Sto10, SHF+11]. The validity of the ray approximations allows to model the propagation of light in optical billiards by studying the

dynamics of classical dynamical billiards with a leak. The far field intensity distribution around micro cavity lasers has a very intricate pattern which can be explained by the fractal intensity distribution inside the region of the phase space that allows transmission to the outside [CW15].

Another class of experimental setup that the model systems we study are relevant for are superconducting microwave billiards [DR15] with absorbers [WBK+14]. Because in quasi two-dimensional realisations of such resonators, the Helmholtz equations describing the propagation of electromagnetic waves in such systems are of the same functional form as the two-dimensional Schrödinger equation [Ric99, Stö99], these experimental setups allow experimental measurement of wave functions in an analogue quantum system. The relevance of classical leaky systems in this context arises at wavelengths corresponding to the semiclassical limit in the quantum system. Introducing a small leak in an otherwise closed system of this kind allows the measurement of spectral properties such as scarring [AOCO95] of the closed system; this process is called chaotic spectroscopy [DS92]. In the field of quantum chaos [Stö99] quantised leaky chaotic systems show the influence of fractal structures in the classical phase space on the quantum dynamics in such systems. Probably most famously, this is expressed in the fractal Weyl law which states that the number of surviving eigenstates in such a system scales algebraically with the dimension of the Hilbert space with an exponent that is the fractal dimension of the chaotic saddle of the corresponding classical system [LSZ03].

In all the leaky systems mentioned so far we have only mentioned completely open leaks. In many physical scenarios, however, the leaks – or absorbing regions – have a finite reflectivity. An example for that is the reflection on the boundary of a microcavity with an angle of incidence smaller than the critical angle of total reflection. In contrast to open systems (full absorption), in *partially* absorbing systems, the box-counting dimension is an integer number equal to the phase-space dimension [APT13a]. Fractality in the classical dynamics of such systems is still present [WM08] and can be quantified using the spectrum of Rényi dimensions.

1.2   This Thesis

In the previous section we argued that fractal dimensions are a central quantity in the study of transient chaos in fully and partially open systems. They are generally defined as the scaling-exponent of some scalar function of the $t \to \infty$ asymptotic invariant measure contained in boxes of size ε of a regular grid covering the phase space in the limit of $\varepsilon \to 0$. In practise, these two limits are almost never reached; the exception being the rare cases,

where an analytical treatment is possible. Instead, the fractal dimension is usually calculated numerically, in which case a sampling of *finite size* ς (the number of found trajectories) of a *finite time t* approximation of the invariant measure is examined at *finite box-sizes* ε. Using statistical and dynamical arguments we show that the finiteness of all three of those parameters can be expressed in terms of finite length scales and thus can be related to each other. Apart from the computational cost of the numerical calculation, there can be physical reasons for the finiteness of any of the scales associated to the parameters. Minimal length scales in physical fractals are in the extreme case for example given by thermal noise or even quantum effects. More interestingly, there are dynamical systems (e.g. weakly chaotic Hamiltonian systems) which exhibit a non-trivial dependence of the effective dimension on ε [LFO91, MLG03, KMBK13].

The aforementioned limitations lead to an observed dimension which depends on the parameters ς, t, and ε. There is a range of values of those parameters, for which the observed dimension does not depend on the particular choice of parameters, but instead is an intrinsic property of the underlying dynamical system. We use the term *effective dimension* (D_{eff}) to describe the observed dimension in this range of parameters. Using fully and partially open strongly chaotic systems we develop a theory that allows the prediction of the parameter ranges leading to D_{eff}. We then continue to show that the concept can be applied to find efficient choices of the parameters of numerical dimension algorithms. We further show that the concepts can be used to gain insight into the dynamics of weakly chaotic systems. And, lastly, we show that in partially open quantum chaotic systems we can use an effective dimension to explain numerical observations. In detail, this work is organised in the following way.

In Chapter 2 we give an introduction to Hamiltonian chaos followed by a general overview over fundamental concepts from the field of transient chaos. We further introduce the stadium billiard, both in its traditional (closed) form and also opened by the introduction of a leak. This chaotic billiard serves as an instructive example of the concepts discussed in that chapter and also reappears later in the text.

The introduction of the type of dynamics considered in this text is then followed by a chapter on fractal dimensions in Chapter 3. There we show the definition of the spectrum of Rényi dimensions which is central to the research presented here and discuss its relevance in the investigation of (leaky) chaotic systems. We also review the most commonly used numerical methods to calculate fractal dimensions and compare them in terms of their generality and numerical efficiency. We then propose a derivative of the algorithms which preserves generality in the sense that it is applicable to a wide range of (multi)fractal measures and allows the calculation of the full Rényi spectrum while at the same time being straightforward to implement and almost perfectly parallelisable.

In the central Chapter 4 we formulate a theory for effective dimensions D_{eff} in strongly chaotic leaky systems. It is based on the numerical observation that even though the asymptotic dimensions in the limit of infinitesimally small box-sizes and infinitely large sample-size are often trivial, there exist parameter-intervals for which we can assign a well defined effective dimension spectrum to approximations of the invariant structures. We show that the bounds of these intervals can be expressed in commonly used dynamical-quantities such as the Lyapunov exponents and the escape rate, and with the help of statistical concepts such as order statistics. We numerically confirm our theoretical predictions in an analytically solvable map, a true-time billiard-map, and in a partially open system and show that the predictions are valid in all three.

For the discussion in Chapter 5 we turn to leaky systems which are not fully hyperbolic. We review stickiness caused by regular regions and marginally unstable periodic orbits embedded within a chaotic phase-space. We then proceed to show that we can identify effective dimensions of the type presented in Ch. 4 even in these types of chaotic systems. We compare the numerically obtained results to the theory presented in Ch. 4 and demonstrate, that the observed features can be explained by a similar reasoning.

In Chapter 6 we present an introduction to partially open quantised chaotic maps and the fractal Weyl law and give a short review of the literature in the field. We then present another type of effective dimension based on the interpretation of the invariant measure as a probability measure. We apply our results about undersampled distributions to explain properties of the eigenvalue spectrum of (partially) open quantised chaotic systems and show that something comparable to the fractal Weyl law can be observed also in the case of partial absorption, and that the observed scaling can be explained from our model.

Lastly, we close the thesis with a review of the central results in Chapter 7.

This thesis is a result of studies conducted between 2012 and 2016 at the Max Planck institute for the physics of complex systems in Dresden under the supervision of Eduardo G. Altmann. The results presented in parts of Sec. 4.4, Chapter 6, and App. D were previously published in [SA15].

Chapter 2

From Closed to (Partially) Open Chaotic Hamiltonian Systems

In this chapter we give an overview over a selection of concepts from the theory of transient chaos that we will need throughout this work. We start with the discussion of chaos in closed systems. Afterwards we consider leaky systems, i.e., systems with fully and partially absorbing regions in the phase space.

The introduction presented here is based on textbooks [Ott02, Str94, LT11, Ozo90, Bäc03, Stö99] and review articles [APT13b, Nov13] on nonlinear dynamics and (transient) classical and quantum mechanical chaotic dynamics. It shall serve as an introduction to the type of dynamics and the systems that we study in later chapters.

2.1 General Concepts in Hamiltonian Chaos

In this work we consider chaotic dynamics in systems that are deterministic and Hamiltonian. A *dynamical system* in this context is a function that describes the temporal evolution of a point x in the N-dimensional phase-space of the system. A system is called *deterministic* if its state is at all times $t > t_0$ uniquely defined by its state at t_0. In a *Hamiltonian* system there exists a set of canonical coordinates (q, p) with $p, q \in \mathbb{R}^N$ spanning the phase-space Ω such that the time evolution in Ω is described by Hamilton's equations

$$\begin{aligned} \frac{\mathrm{d}p}{\mathrm{d}t} &= -\frac{\partial \mathcal{H}}{\partial q} \\ \frac{\mathrm{d}q}{\mathrm{d}t} &= +\frac{\partial \mathcal{H}}{\partial p} \end{aligned} \quad . \tag{2.1}$$

The Hamiltonian $\mathcal{H}(q, p, t)$ fully describes the dynamics in the system. For this work one of the most important properties of Hamiltonian systems is that because of their symplectic structure the dynamics preserves infinitesimal phase-space volumes. We stress this property here because it allows to differentiate the case that there are absorbing regions in Ω which we discuss below and which leads to a decay with time of relevant sets in the phase-space from the dynamics in dissipative systems which show decaying behaviour in a different sense and which are not subject of this thesis.

For the most part, in this work we study Hamiltonian chaos in symplectic maps which are the discrete-time equivalent of such continuous Hamiltonian systems [Mei92]. Such mappings are of the form

$$x_{n+1} = \mathcal{M}x_n, \tag{2.2}$$

where the $x_n \in \Omega$ are the subsequent states of the system. Such maps can be created by discretising a continuous-time system. One way of achieving a discretisation of a flow is by stroboscopic mapping, i.e., by noting the state of trajectories at fixed time-intervals, which leads to a map of the type

$$x(t + T) = \mathcal{M}_T x(t), \tag{2.3}$$

where the map $\mathcal{M}_T$ describes the change in the value of x within one period T. This method is especially useful in periodically driven systems where the driving period provides a natural choice of T. Another way of obtaining a discrete time map from a flow is to create a Poincaré map by reducing trajectories[1]

$$x(t) = \left(x^{(1)}(t), x^{(2)}(t), \ldots, x^{(N)}(t) \right) \in \mathbb{R}^N$$

to a discrete time trajectory $\{\chi_0, \chi_1, \ldots, \chi_n, \ldots\}$ by only considering the intersection points of the trajectory and a hyperplane of dimension $N - 1$, where

$$\chi_n = \left(f^{(1)}\left(x(t^*)\right), \ldots, f^{(N-1)}\left(x(t^*)\right) \right) \in \mathbb{R}^{N-1}$$

is the set of free coordinates at the point in time t^* when $x(t)$ intersects the plane for the nth time. The function f defines the shape of such a Poincaré surface of section and the mapping $\mathcal{M}_P$ from one point of intersection to the subsequent one is called Poincaré map:

$$\chi_{n+1} = \mathcal{M}_P \chi_n, \tag{2.4}$$

This sort of reduction to a map is generally possible and the resulting mappings are

---

[1]We use the superscript $^{(i)}$ do mark the ith component $x^{(i)} \in \mathbb{R}$ of $x \in \mathbb{R}^N$.

often simpler to handle in computations than the flow. There are also computationally convenient "artificial" chaotic maps that show behaviour similar to maps created by the methods described above. For the sake of clarity the notation and examples in this work are oriented on such artificial discrete time systems. Nonetheless, the results obtained also apply to the more complicated dynamics in maps created by a discretisation of flows in physical systems.

The notion of chaos in such systems is based on the concept of stability. We define the Jacobian matrix $J(x^*)$ as[2]

$$J(x^*) := \left(\frac{\partial \mathcal{M}}{\partial x} \right) \bigg|_{x=x^*}. \tag{2.5}$$

This defines a linearisation of the dynamics of $\mathcal{M}$ around x^* so that we can approximate the evolution of a trajectory close to x^* by a Taylor expansion to first order as

$$\mathcal{M}(x^* + \delta) \approx \mathcal{M}x^* + J(x^*)\delta + \cdots \tag{2.6}$$

for small δ. If x is a fixed point, i.e., if $\mathcal{M}x = x$, then we can use this equation to qualify the stability of this fixed point by looking at a nearby trajectory starting at $x' = x + \delta$:

$$\delta \mapsto \mathcal{M}(x + \delta) - \mathcal{M}(x) \approx J(x)\delta. \tag{2.7}$$

In an N-dimensional system $J(x)$ has a system of N eigenvalues l_i and eigenvectors v_i. The component $\delta \cdot v_i$ of a deviation δ away from x grows or shrinks in one iteration of $\mathcal{M}$ by a factor of l_i. So any small volume containing x is stretched in the direction of v_i by a factor of l_i. In a similar fashion we can define the linear stability of any orbit of period n by using the fact that any point of such an orbit is a fixed point of a map $\tilde{\mathcal{M}} := \mathcal{M}^n$. The resulting eigensystem $(\tilde{v}_i, \tilde{l}_i)$ describes the stretching – or squeezing – of the distance between the periodic orbit and a nearby trajectory within one period of the orbit, so that we can define a set of stretching factors $l_i := \tilde{l}_i/n$ that quantify the stretching within one iteration.

To simplify the discussion below it is useful instead of the eigenvalues l_i we discuss exponents $\Lambda_i \in \mathbb{C}$ such that $l_i = \mathrm{e}^{\Lambda_i}$. The volume-preserving property of a map implies

---

[2]Let $x, y \in \mathbb{R}^N$. Using $v^{(i)}$ for the ith component of a vector $v \in \mathbb{R}^N$ we define the following short-hand notation:

$$\frac{\partial y}{\partial x} := \begin{pmatrix} \frac{\partial y^{(1)}}{\partial x^{(1)}} & \frac{\partial y^{(1)}}{\partial x^{(2)}} & \cdots & \frac{\partial y^{(1)}}{\partial x^{(N)}} \\ \frac{\partial y^{(2)}}{\partial x^{(1)}} & \frac{\partial y^{(2)}}{\partial x^{(2)}} & \cdots & \frac{\partial y^{(2)}}{\partial x^{(N)}} \\ \vdots & \vdots & \ddots & \vdots \\ \frac{\partial y^{(N)}}{\partial x^{(1)}} & \frac{\partial y^{(N)}}{\partial x^{(2)}} & \cdots & \frac{\partial y^{(N)}}{\partial x^{(N)}} \end{pmatrix}$$

that the Jacobian determinant is equal to unity:

$$|\det J(x)| = 1 \,. \tag{2.8}$$

Expressed in terms of the stability exponents of $J(x)$ an equivalent formulation is $\left|\sum_{i=1}^{N} \Lambda_i\right| = 0$. So for the real part of a set of Λ_i values at a certain point the possible scenarios are

(i) All $\Re\Lambda_i = 0$: A fixed point with purely imaginary stability exponents is called *elliptic*. A volume close to such a point is rotated around it with time but neither stretched nor squeezed.

(ii) If one or more $\Re\Lambda_i > 0$ there must exist $\Re\Lambda_j < 0$ such that the stretching is compensated. An eigenvector associated to the negative (positive) exponents defines a stable (unstable) direction of a fixed point, and the manifold containing all forwards (backwards) iterations of a small perturbation in an unstable (stable) direction is called unstable (stable) manifold such that every point on the stable (unstable) manifold converges to the fixed point under forwards (backwards) iteration.

(iii) The special case of (ii) with $\Re\Lambda_i \neq 0$ for all i defines a *hyperbolic* fixed point. The name stems from the fact that trajectories that are passing by such a point do this on a trajectory resembling a hyperbola. They first approach along the stable direction close to but not on the stable manifold before the trajectory bends away from the fixed point and they are accelerated along the unstable direction.

There also exist fixed points with slower than exponential instability that therefore cannot be expressed in terms of stability exponents. Such linearly unstable points are called *marginally unstable* and we discuss them in detail in Ch. 5.

Up to this point we have established that we are interested in Hamiltonian systems and that such systems can be treated as maps. Furthermore we have discussed how to treat periodic orbits in such systems. What remains to be introduced is the concept of chaotic dynamics. While most people seem to agree on a colloquial definition of dynamical chaos which could be summarised as the emergence of unpredictability and random-like behaviour usually associated to stochastic systems in systems that are fully deterministic, stating a rigorous and minimal definition of chaos is much more difficult. In fact, there exist numerous definitions [Fot05]. In light of the scope of this work the following definition is sufficient: We call the dynamics in a bounded set $\mathcal{C}$ (with $x \in \mathcal{C} \Rightarrow \mathcal{M}x \in \mathcal{C}$) *chaotic* if it fulfills the following criteria:

(i) For every $x \in \mathcal{C}$ there exists a periodic point x' arbitrarily close to x.

(ii) Trajectories in $\mathcal{C}$ diverge exponentially fast, i.e., the distance between nearby trajectories grows exponentially with time. Of course, since $\mathcal{C}$ is finite the Euclidean distance between two trajectories can not grow exponentially for all times, but the probability that both are within some ϵ-environment decreases exponentially fast.

(iii) The dynamics in $\mathcal{C}$ is mixing, which means that if we pick any two volumes $\mathcal{A}$ and $\mathcal{B}$ contained in $\mathcal{C}$, there exists an $x \in \mathcal{A}$ and an $n \in \mathbb{N}$ with $\mathcal{M}^n x \in \mathcal{B}$.

From (i) and (iii) it follows that there exist arbitrarily long periodic orbits that come arbitrarily close to every point in $\mathcal{C}$ so that we can use their stability exponents to describe the exponential divergence of two close-by trajectories on the set. This divergence is described by the Lyapunov exponents λ_i. Let $\epsilon > 0$ and two points x and x' with $x, x' \in \mathcal{C}$ and $|x - x'| < \epsilon$. Then we can approximate (see Eq. (2.5) and below) the nth image of x' as $\mathcal{M}^n x' \approx \mathcal{M}^n x + J^n(x)(x' - x)$, where $J^n(x) := J(\mathcal{M}^{n-1}x) \cdot J(\mathcal{M}^{n-2}x) \cdot \ldots \cdot J(x)$. For almost all initial conditions $x_0 \in \mathcal{C}$ and large n, the eigenvalues $l_{i,n}$ of $J^n(x_0)^{\mathrm{T}} J^n(x_0)$ are the same and

$$\lambda_i := \lim_{n \to \infty} \frac{1}{2n} \ln l_{i,n}, \tag{2.9}$$

with $i = 1, 2, \cdots, N$ and $\lambda_i \in \mathbb{R}$, defines the spectrum of Lyapunov-exponents. We follow the conventional ordering $\lambda_1 \geq \lambda_2 \geq \cdots \geq \lambda_N$. Every typical small variation with time aligns itself with the direction associated to λ_1 so that the largest Lyapunov exponent can be interpreted as a measure of the severeness of the exponential decay mentioned in (ii). λ_1 can be numerically approximated by iterating two nearby initial conditions x and $x' = x + \delta x$ and observing the stretching of the displacement vector δx:

$$\lambda_1 = \lim_{n \to \infty} \lim_{|\delta x| \to 0} \frac{1}{n} \ln \frac{|\mathcal{M}^n \delta x|}{|\delta x|} \tag{2.10}$$

If $\lambda_1 > 0$, criterion (ii) above is fulfilled and thus the two formulations are equivalent.

2.2   Closed Stadium Billiards and True-Time Maps

Dynamical billiards are a very instructive class of systems to study Hamiltonian chaos [CM06] and we will use this section to introduce a particular example of them – the stadium billiard. We also introduce a Poincaré map for dynamical billiards that acts on an extended phase-space and allows the description of the true-time (as opposed to iteration-number) dynamics [KL01]. Dynamical billiards are straightforward to implement numerically and depending on the choice of boundary shape all typical cases of dynamics found in other Hamiltonian systems can be reproduced.

FIGURE 2.1: Stadium billiard boundary (black) with shape-parameters L and r in blue and an example of a collision at (s, ϑ) in red.
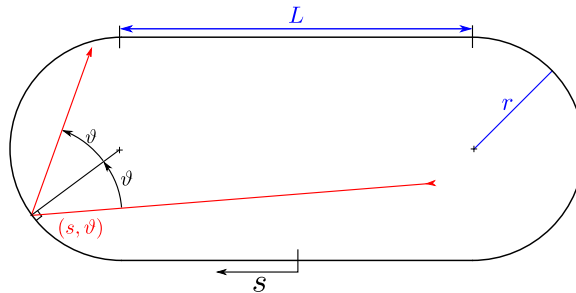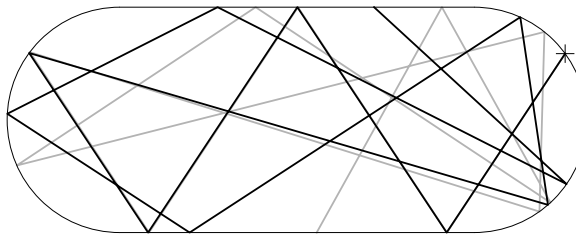
FIGURE 2.2: Exponential divergence of two trajectories with almost identical initial conditions. Both start from the same point $(+)$ on the boundary and their initial angles differ by around $0.05°$. The trajectories are truncated at the 11th collision with the boundary.

The dynamics in a billiard takes place on an area $\mathcal{Q}$ in configuration space which is circumscribed by an boundary $\partial\mathcal{Q}$. We consider the dynamics of "balls" (i.e. massless point like particles) moving freely in $\mathcal{Q}$ which collide elastically with the boundary. That means at a collision the velocity vector of the ball is mirrored on a line tangent to $\partial\mathcal{Q}$ at the collision point. Depending on the choice of boundary-geometry billiards can be fully integrable (e.g. circular boundary), fully hyperbolic (e.g. cardioid shape [Rob83]), hyperbolic with measure-zero continuous families of marginally unstable periodic orbits (e.g. stadium), and mixed regular and chaotic (e.g. mushroom [BVA12] or limaçon [DB01]).

A particularly popular and widely studied example of a chaotic billiard is the stadium-billiard. Its boundary is made up of two semi-circular arcs with radius r connected by two parallel lines of length L which are smooth continuations of the arcs. This shape is shown in Fig. 2.1. Stadium billiards are fully chaotic in the sense of the definition in the previous section. They do however have a class of periodic orbits that are not exponentially unstable but only linearly unstable. The most obvious marginally unstable periodic orbits (MUPOs) are trajectories of balls bouncing perpendicularly back and forth between the straight wall segments. If the angle is slightly perturbed away from a perpendicular direction the distance of the perturbed trajectory to the unperturbed one grows only linearly. This family of MUPOs can trap trajectories for a while if they enter the area between the straight wall segments in a direction that is almost perpendicular to a straight segment. The length of this trapping depends on the angle of incidence. This effect is called stickiness and we will discuss it in Ch. 5. In Fig. 2.2 we show parts
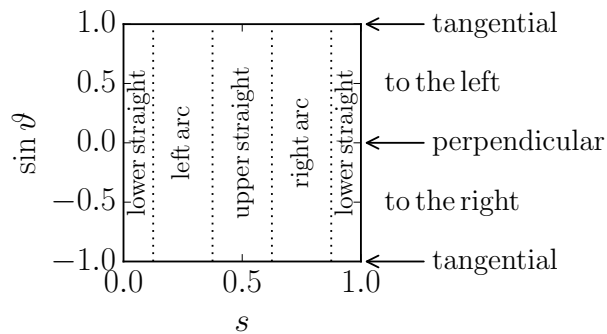
FIGURE 2.3: Schematic illustration of billiard coordinates $(s, \sin \vartheta)$ in a stadium where L is equal to the arc-length. The vertical segments are labeled with the respective part of the boundary. On the right we indicate the outgoing direction with respect to a normal pointing towards the inside.

of two trajectories in a stadium billiard. They follow each other closely until they hit the curved part of the boundary for the first time. Up to that point the divergence was merely linear. After that the exponentially fast divergence is clearly visible.

In billiards the dynamics is independent of the velocity of the balls and we can reduce a trajectory in real space to a series of collision-events $\{x_0, x_1, \cdots, x_n, \cdots\}$ with $x_n = (s_n, \sin \vartheta_n)$ (see Fig. 2.1) by reducing the motion to a Poincaré surface of section on the boundary. Here, $s \in [0, 1)$ is the parametrised position along the boundary and $\vartheta \in (-\pi/2, \pi/2)$ is the collision angle, i.e., the angle between the normal vector at the collision point and the incoming trajectory. The collision angle thus is defined in such a way that if we were to look from the collision point along the normal direction towards the inside of the billiard a trajectory coming from our right with a very flat angle to ∂Q and leaving with the same flat angle towards our left would have a positive ϑ value close to $\pi/2$. The steeper the angle between the trajectory and the boundary, the closer ϑ approaches zero. The case $\vartheta = 0$ then corresponds to a collision perpendicular to the boundary. A ball approaching from our left is described by a value $-\pi/2 \leq \vartheta < 0$. For the variable s along the boundary we chose the following definition: $s = 0$ at the center of the lower straight segment and s is the length a of the boundary-segment between this origin and the collision point measured in clockwise direction and normalised by the total length of the boundary: $s = \frac{a}{2L+2\pi r}$. Throughout this work we plot $\sin \vartheta_n$ versus s_n, so that the different parts of the boundary correspond to vertical strips in these plots. This transformation of coordinates makes the billiard map area-preserving [Ber81] and the tuple $(s, \sin \vartheta)$ is called Birkhoff-coordinates; we illustrate them in Fig. 2.3.

Stadium billiards exhibit a particular type of trajectory that showcases the importance of distinguishing between the iteration-time and true-time dynamics. Since the velocity of all "balls" is identical, the time $\tau(x)$ a trajectory spends between two

collision points can be assumed to be equal to the distance between the collision points:

$$\tau(x_n) = |x_n - x_{n+1}| \tag{2.11}$$

Trajectories that collide almost tangentially to the wall get trapped in the semi-circular parts of the boundary, because the number of iterations to escape from there goes to infinity as $\sin\vartheta \to \pm 1$. At the same time, their real runtime is bound by the length $r\pi$ of the semi-circular segments. Depending on the application it is often necessary to look at the runtime instead of the iteration number and it can be incorporated into the mapping by extending the phase-space and considering the true-time map

$$\mathcal{M}^* : \begin{cases} x_n \mapsto x_{n+1} = \mathcal{M}x_n \\ t_n \mapsto t_{n+1} = t_n + \tau(x_n) \end{cases} \tag{2.12}$$

where t_n is the length of the trajectory after n collisions ($t_0 := 0$).

2.3   Transient Chaos in Open Systems

So far we have discussed chaotic dynamics in closed Hamiltonian systems. In this section we introduce the concept of leaks in the phase space and define the relevant quantities that we use to discuss the dynamics in open systems later in this work. If we open the phase-space Ω of an ergodic chaotic system, e.g., by introducing an absorbing region $\mathcal{H}$ intersecting it, any ensemble of trajectories started in Ω decays with time as more and more trajectories get absorbed. In such system chaotic dynamics is only prevalent for a transient time, hence the term *transient chaos* is used to describe such behaviour [LT11].

To describe this sort of dynamics in maps it is useful to extend the true time map [APT13b] by setting

$$\mathcal{M} : x_n \mapsto \begin{cases} x_{n+1} = \mathcal{M}_{\text{closed}}x_n, & \text{if } x_n \notin \mathcal{H} \\ \text{escape}, & \text{if } x_n \in \mathcal{H} \end{cases} \tag{2.13}$$

in Eq. (2.12). With that we can define the escape time of a trajectory: Let $x \notin \mathcal{H}$ and

$$n_{\text{esc}}(x) := \max\{n^* : \mathcal{M}^{n^*}x \notin \mathcal{H} \ \forall \ n^* \leq n\} + 1 \tag{2.14}$$

and $n_{\text{esc}}(x) = 0$ for $x \in \mathcal{H}$. The escape time is then defined as

$$t_{\text{esc}}(x) := t_{n=n_{\text{esc}}(x)}. \tag{2.15}$$

We further define the finite-time trapped set as

$$\mathcal{S}_t := \{x \in \Omega : t_{\text{esc}}(x) \geq t\}. \tag{2.16}$$

The survival probability $P(t)$ which is the probability that the trajectory of an initial condition randomly chosen somewhere in Ω has an escape time of at least t and it is equal to the probability that an initial condition placed randomly in Ω belongs to $\mathcal{S}_t$ which is equal to the relative volume of $\mathcal{S}_t$:

$$P(t) = \mu_{\text{L}}(\mathcal{S}_t), \tag{2.17}$$

where μ_{L} is the Lebesgue measure normalised such that $\mu_{\text{L}}(\Omega) = 1$. Because the dynamics on Ω is mixing or – in other words – because typical trajectories explore the full phase space almost every trajectory has a finite escape time and

$$P(t) \xrightarrow{t \to \infty} 0. \tag{2.18}$$

There is, however, a subset of measure zero that survives even in that limit. This subset is called the forward trapped set $\mathcal{S}_\infty$. Analogously, the set surviving infinitely long under time-reversed dynamics is the backwards trapped set $\mathcal{S}_{-\infty}$. The points $x \in \mathcal{S}_\infty \cap \mathcal{S}_{-\infty}$ are trapped in both temporal directions and they form the *chaotic saddle* of the open system [LFO91, LT11, JT91]. The trapped sets $\mathcal{S}_\infty$ ($\mathcal{S}_{-\infty}$) form the stable (unstable) manifold of the saddle.

For *closed* systems an invariant quantity is the natural measure $\mu_{\text{n}}(\mathcal{B})$ defined as the relative time a typical trajectory spends within a ball $\mathcal{B}$: Let $\mathcal{B}$ be a ball in Ω and $\{x_1, x_2, \ldots, x_n\}$ be a trajectory generated by $\mathcal{M}_{\text{closed}}$. Then the probability of finding points of such a trajectory in $\mathcal{B}$ defines the natural measure:

$$\mu_{\text{n}}(\mathcal{B}) := \int_{\mathcal{B}} \mathrm{d}\mu_{\text{n}} = \lim_{n \to \infty} \frac{1}{n} \sum_{i=1}^{n} \mathbb{I}_{\mathcal{B}}(x_i), \tag{2.19}$$

where

$$\mathbb{I}_{\mathcal{B}}(x_i) := \begin{cases} 1, & \text{if} \quad x_i \in \mathcal{B} \\ 0, & \text{else} \end{cases}. \tag{2.20}$$

Due to the ergodic property of the chaotic systems we consider, all but a subset of measure zero of initial conditions lead to the same distribution μ_n after some transient
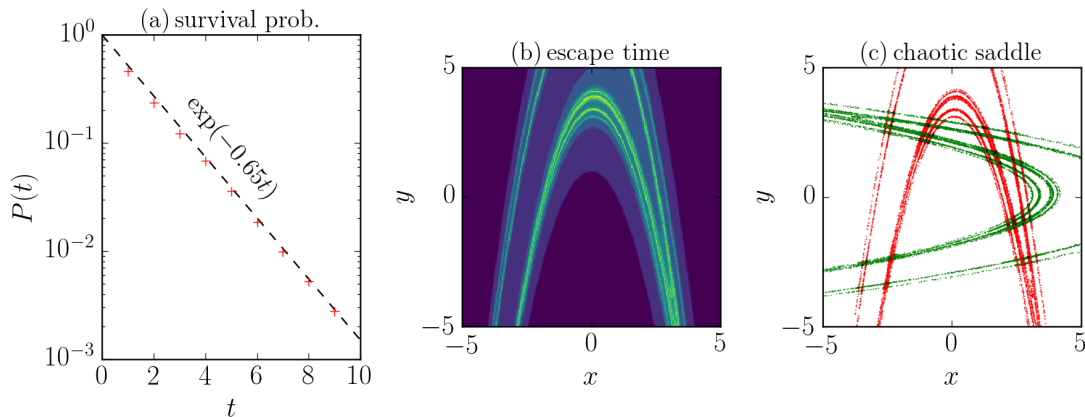
FIGURE 2.4: Escape from a volume preserving Hénon map: $x_{n+1} = 6 - x_n^2 - y_n$, $y_{n+1} = x_n$, and $t_{n+1} = t_n + 1$. A trajectory escapes if $|x| > 5$. (a) Exponential decay of $P(t)$; Numerical results ($+$) and an exponential function (dashed) for comparison. (b) Escape times (low: dark blue, high: yellow). (c) Numerical approximation of stable (red) and unstable (green) manifolds of the saddle (black).

time. In *open* systems, the probability of finding a trajectory which does not leave the system goes to zero with time (see Eq. (2.18)) so that the only place where the $n \to \infty$ limit in Eq. (2.19) is defined is on the chaotic saddle and on its stable manifold. As an example, in Fig. 2.4 we show a numerical treatment of the chaotic saddle in a chaotic map. For this particular choice of parameters of the map is area preserving (2.8) for all $r \in \mathbb{R}^2$. We chose the hole as $\mathcal{H} = \mathbb{R}^2 \backslash \{(x,y) \in \mathbb{R}^2 : |x| \geq 5\}$. This system is slightly different from the usual notion of open systems that we use in this work because it is not the result of opening an otherwise bounded chaotic set to the outside. Instead, almost every trajectory leaves to infinity. The escape here happens exponentially fast as we numerically confirm by starting a large number of initial conditions and counting the remaining ones after t iterations. The results in Fig. 2.4(a) show that in this map $P(t)$ is very closely described by an exponential decay. The distribution of the escape times presented in Fig. 2.4(b) already hints at the position and shape of the stable manifold which must be close to the points with high escape times in this plot. In Fig. 2.4(c) we show numerical approximations of the manifolds and the saddle. They are created by finding trajectories with escape times $t_{\text{esc}} \geq t^* = 5$ by random sampling of initial conditions in the shown sector. For this choice of t^* the survival probability dropped to $P(t^*) \approx 10^{-2}$. To approximate the unstable manifold we define the time-reversed map and apply the same criterion. The saddle is the intersection of these sets. From these approximations we can already get a good idea of the shape and position of the manifolds and the saddle. For a more quantitative discussion, however, a more fine-grained approximation would be necessary.

Since the area of $\mathcal{S}_\infty$ is zero, its natural measure is also is zero and therefore

it is not useful to describe the distribution of $\mathcal{S}_\infty$ in Ω. A measure μ_c is said to be conditionally invariant [PY79] if, for any $\mathcal{B}$ contained in Ω, it fulfills

$$\mu_c(\mathcal{B}) = \frac{\mu_c(\mathcal{M}^{-1}\mathcal{B})}{\mu_c(\mathcal{M}^{-1}\Omega)}, \tag{2.21}$$

as is the case with the natural unstable manifold measure which is invariant under the condition that we renormalise it at every time step which is achieved by the factor $\mu_c(\mathcal{M}^{-1}\Omega)$. This factor accounts for the overall decay of the total measure, i.e., $\mu_c(\Omega) = \alpha\mu_c(\mathcal{M}^{-1}\Omega)$ with $\alpha < 1$.

Following this line of argument, we define a natural measure of the stable manifold in the following way: Let $\mathcal{B}$ be a ball in Ω with $\mathcal{B}\cap\mathcal{S}_\infty \neq \emptyset$. The natural stable manifold measure μ_s is the relative volume of the remaining set in $\mathcal{B}$ in the limit $t \to \infty$:

$$\mu_{\mathrm{ns}}(\mathcal{B}) = \lim_{t\to\infty} \frac{\mu_{\mathrm{L}}(\mathcal{B}\cap\mathcal{S}_t)}{\mu_{\mathrm{L}}(\mathcal{S}_t)}. \tag{2.22}$$

Since $\mu_{\mathrm{L}}(\mathcal{S}_t)$ is equal to the survival probability $P(t)$ we can also use this term instead. In a similar way, it is possible to define a version of this measure for the unstable manifold by replacing $\mathcal{S}_t$ with $\mathcal{S}_{-t}$ in Eq. (2.22). With this definition of μ_{ns} we close this general introduction of leaky systems with fully open holes. In the next section we discuss the introduction of holes on the specific example of the leaky stadium billiard. A generalisation of the concepts from this section to partially open systems follows in Sec. 2.5.

2.4   Open Stadium Billiards

Billiards are very suitable systems to study transient chaos in open systems [DG09, NKL$^+$07]. As mentioned in Sec. 2.2 they can easily be tailored to have the desired mix of dynamical behaviour and an opening in the phase space of a billiard also often has an intuitive interpretation. The representation of different kinds of holes in the phase space defined in the billiard coordinates introduced in Sec. 2.2, however, is sometimes not as straightforward, so we will discuss it in detail in this section.

The most intuitive type of hole is a gap in the boundary that allows the escape of trajectories. In Fig. 2.5 we show two examples of trajectories in a billiard with that type of hole. The initial conditions were chosen to be the same as in Fig. 2.2, so they are very close together. Nonetheless, the integer escape times differ by a factor of two. This already hints at the complicated structure of the surviving set in the phase-space which we will discuss in more detail in later sections. The $(s, \sin\vartheta)$-space representation

FIGURE 2.5: Trajectories in a billiard with a hole. Both start from the same point (+) on the boundary. Their initial angles differ by 0.05° and their escape times are $n_{\mathrm{esc,\,black}} = 11$ and $n_{\mathrm{esc,\,grey}} = 22$.
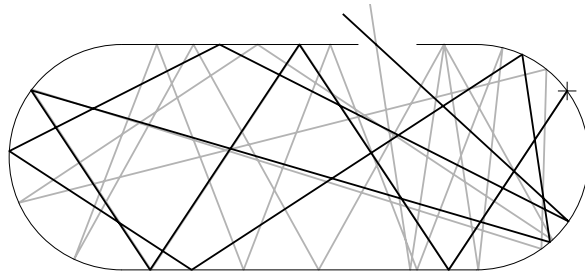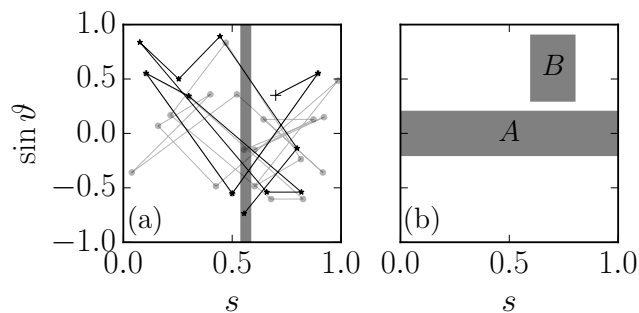
FIGURE 2.6: (a) Trajectories from Fig. 2.5 in billiard coordinates. The grey strip represents the hole. The initial conditions are marked with + points are connected to illustrate their order. (b) Other types of holes. A: Full (no) reflection above (below) a critical value of $|\vartheta|$; B: no direct physical equivalent.

of the same two trajectories is shown in Fig. 2.6(a). Like in Fig. 2.5 the first 4 images of the initial points are almost indistinguishable and afterwards the quick correlation loss is clearly visible. A few interesting properties of this representation can be seen in the example of the two trajectories plotted here. We can see how mappings from one straight to the other straight (2nd, 3rd, and 4th image of each trajectory) correspond to a linear change (modulo 1) of s and only a sign change of $\sin\vartheta$. We can also observe how mappings within the same arc (5th, and 6th image) only change s and not $\sin\vartheta$.

The gap in the boundary is a vertical region in $(s, \sin\vartheta)$-space and it is marked as a grey band in Fig. 2.6(a). It spans the whole range of $\sin\vartheta \in [-1, 1]$ because such a hole allows every trajectory to pass independently of the angle. Apart from this kind, we also consider other types of opening in this work. In general when we discuss holes in billiards in this work we consider rectangular regions in phase space defined by the set $\{s_{\min}, s_{\max}, \vartheta_{\min}, \vartheta_{\max}\}$ so that a trajectory is absorbed if $s_{\min} < s \leq s_{\max}$ and $\vartheta_{\min} < \vartheta \leq \vartheta_{\max}$. As seen above, a physical hole in the boundary comparable to the pockets of a billiard table then corresponds to the case of $\vartheta_{\min} = -\pi/2$ and $\vartheta_{\max} = \pi/2$. In Fig. 2.6(b) we show two other types of hole that are relevant for this work. Any choice that is symmetric around the line $\vartheta = 0$ means that any collision above or below some
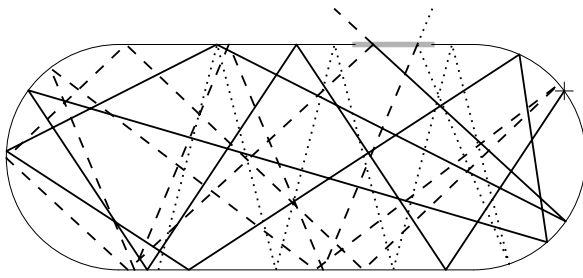
FIGURE 2.7: 30 iterations of a single trajectory in a billiard (starting at +) with a partially reflecting hole (grey region in top straight segment) with a reflectivity of 50%. The dashed part has a half the intensity than the solid part and the dotted part has a quarter left.

critical value leads to an escape, while other reflections are unaffected. Such a choice is reminiscent of the reflection of light rays on the interface between dielectric materials of different refractive index [CW15]. This sort of reflection can of course be restricted to only parts of the boundary. Sometimes it is also useful to chose less physical holes like the one denoted B in Fig. 2.6(b). This hole makes part of the boundary transparent to a narrow band of angles but in such a way that a trajectory could pass through a collision $(s, \sin \vartheta)$ in one direction, while it would leave the system if followed in the opposite direction $(s, -\sin \vartheta)$.

2.5 Partially Open Systems

In the discussion leading up to this section we have considered holes that completely absorb every trajectory that enters as described by Eq. (2.13). In this section we take a look at the more physically relevant case of holes that are not completely absorbing and at the necessary modifications of the concepts introduced in the context of systems with fully absorbing holes. A motivation of the study of partially open systems is given in Sec. 1.1, and the formalism in this section is oriented on the presentation found for example in [APT13b]. The optical microcavities mentioned there comprise of a disk of transparent material surrounded by a layer with a different refractive index so that there is a critical angle of incidence at the interface between the two materials above which a ray of light inside the disk is fully reflected and below which it is partially transmitted to the outside. We now give an introduction to a way of modelling such a partial reflection using partially transparent holes in well established chaotic systems.

Partial leaks in their most general form are incorporated into the discrete time systems discussed so far by instead of defining a hole as in Sec. 2.3 defining a real valued function $R(x) \in [0,1]$ that defines the reflectivity coefficient at x. We incorporate the effect of partial absorption by associating to each trajectory an intensity I_n, with $I_0 = 1$, $I_{n+1} = R(x_n)I_n$. This type of dynamics in a billiard with a partial leak is sketched in

Fig. 2.7. It can be expressed by an extended true time map defined as

$$
\mathcal{M}^* : \begin{cases} x_n \mapsto x_{n+1} = \mathcal{M}x_n \\ t_n \mapsto t_{n+1} = t_n + \tau(x_n) \\ I_n \mapsto R(x_n)I_n \end{cases} , \tag{2.23}
$$

where $\mathcal{M}$ can be an open or closed map. Since it is more useful in studying the transition between open and closed systems we restrict the discussion in this work to a slightly less general type of opening: we consider the case of a small absorbing region $\mathcal{H}$ with $R(x) = R < 1$ inside that region of the phase-space (i.e. $R(x) = 1$ everywhere else).

If $R = 0$ in the absorbing region the system corresponds to usual open systems and the asymptotic behaviour can be discussed in terms of trapped sets. The set of initial conditions x_0 with $\lim_{t \to \infty} I_n = 1$ form the forward trapped set $\mathcal{S}_\infty$ of the map (the stable manifold of the chaotic saddle). Analogous to the definition of the invariant stable manifold measure (see Eq. (2.22)) in systems with fully transparent holes we can define an invariant asymptotic measure from the intensity distribution in partially open systems by normalising to the total intensity left in the system. The analog to the stable manifold measure (see Eq. (2.22)) in a partially absorbing system with $0 < R < 1$ in a phase-space region $\mathcal{B}$ should be proportional to the average intensity I_n for $n \to \infty$ of randomly drawn $x_0 \in \mathcal{B}$. The finite time normalised measure of $\mathcal{B}$ after n iterations can thus be written as

$$
\mu_n(\mathcal{B}) = \frac{\langle I_n \rangle_\mathcal{B}}{\langle I_n \rangle_\Omega}, \tag{2.24}
$$

where the average intensity $\langle ... \rangle_\mathcal{B}$ is computed over initial conditions $x_0 \in \mathcal{B}$. The asymptotic stable manifold measure then follows from taking the limit $n \to \infty$

$$
\mu_\mathrm{s}(\mathcal{B}) = \lim_{n \to \infty} \frac{\langle I_n \rangle_\mathcal{B}}{\langle I_n \rangle_\Omega}, \tag{2.25}
$$

This definition is consistent with the usual definition of the natural stable manifold measure defined in Eq. 2.22 considering the intensities $I \in [0, 1]$ of trajectories as weights (see also Ref. [APT13b]). More precisely, the normalised density of the support of μ_s (short: supp(μ_s)) defines μ_ns in ergodic systems. If $R(x) \neq 0$ for all $x \in \Omega$ and $\mathcal{M}$ in Eq. (2.23) is closed, supp(μ_s) is the full phase space. The equivalent unstable manifold measure can be achieved from Eq. (2.24) by computing $\langle I_n \rangle$ over the positions $x_n \in \mathcal{B}$ after n iterations instead of the initial conditions.

In summary, in this chapter we have introduced (partially) open chaotic systems, the concept of the chaotic saddle and its (un)stable manifolds, and the associated natural measures. We have also introduced a measure based on the asymptotic intensity in

partially open systems.

Chapter 3

Fractal Dimensions in Open Chaotic Systems

As we have seen in Chapter 1, fractal dimensions are a powerful tool to study the properties of dynamical systems. In this chapter we give a mathematical definition of the dimensions we consider and afterwards discuss methods for their numerical calculation. We begin this chapter with an introduction to the fractal dimension spectrum that we consider in this work. After that, in Sec. 3.1.3 we show that fractal dimensions are useful in the description of invariant structures in open systems. Towards the end of the chapter, in Sec. 3.2 we review common algorithms to calculate fractal dimensions. In this review we concentrate on their suitability in the calculation of the fractal dimension spectrum of invariant fractal and multifractal measures in open chaotic systems. Afterwards, in Sec. 3.2.2 we present a new method suitable to calculate the full Rényi dimension spectrum of a measure. We close the chapter in Sec. 3.2.3 with a qualitative comparison of the efficiency and generality of the different algorithms.

3.1 Introduction to Fractal Dimensions

Expressed in simple terms, fractals are objects that "look the same" on different scales, i.e., if we take a picture of a fractal object, pick a small region in the picture, and blow that region up to the same size as the original picture, the two would look alike. On the one hand, that can mean that the two are exactly the same, as it is for example the case with a middle third cantor set if the region to zoom in is chosen appropriately. In a more general sense, however, it means that zooming in leads to a qualitatively similar picture. Both kinds of self similarity – the exact kind and the qualitative kind – can be

FIGURE 3.1: First 2 iterations of the construction of a Koch curve. In each iteration step, every straight segment of the curve is replaced by the shape seen in the 2nd row.
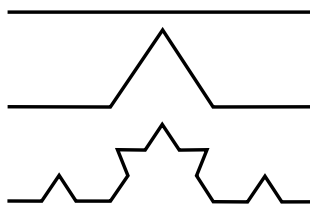
expressed in terms of fractal dimensions. In fact, fractal dimensions are suitable a way of defining both exact and qualitative self similarity.

The concept of fractal dimension is an extension of the general notion of spatial dimension [Str94, Ott02, TG06, Man04]. The dimension of an object can be interpreted as the number of variables needed to uniquely describe a point on the object. For example, along a one dimensional curve, the position of a point on the curve is uniquely defined by the distance to a arbitrarily chosen origin on the curve. Now, if the curve is a fractal, such as, for example, the Koch curve (see Fig. 3.1) is, then the length along the curve between two points is infinite and therefore its dimension must be larger than one. At the same time this curve is still made up of infinitely short line segments and it does not fill an area, in the sense that if we were to draw a box of any size around any part of the curve, almost all points in the box would not belong to the Koch curve, i.e., the probability that a randomly drawn point in the box lies on the curve is zero. If we would try the same with a two dimensional object, this probability would be larger than zero, so the Koch curve is neither one, nor two dimensional, instead its dimension is a non-integer number. This is the defining property of fractal objects and the fractal dimension is always smaller than the dimension of the embedding space.

3.1.1   Box-Counting Dimension

The box counting dimension D_0[1] is a commonly used and very accessible fractal dimension, i.e., it is intuitive and convenient to compute numerically. The box-counting dimension of a set is the exponent of the asymptotic ($\varepsilon \to 0$) scaling of the minimal number[2] of disjoint ε-sized boxes that is needed to completely cover the set. Its definition is slightly different from another popular choice of fractal dimension, the *Hausdorff dimension*, which is defined as the scaling exponent of the minimal number of – not necessarily non-overlapping – balls of radius r needed to completely cover S as $r \to 0$.

---

[1] we use the subscript 0 because – as we will see in Sec. 3.1.2 – the box-counting dimension is just one special case of a full spectrum of fractal dimensions

[2] In practise, for small enough box sizes the number is not changing drastically with a shift of the covering grid, so that it is not necessary to minimize the number at every box-size. If the fractal is strictly self similar, however, an improper choice of box-sizes can introduce systematic errors.

The box-counting dimension always gives an upper bound to the Hausdorff dimension and for most fractals they converge to the same value [Ott02].

In this work, we concentrate on the box-counting dimension for two main reasons. First, the box-counting dimension is a special case of a full spectrum of dimensions that we consider and, second, it is much more conveniently computed numerically. It is formally defined in the following way: Let $\mathcal{S}$ be a fractal object embedded in $\mathbb{R}^N$. The box-counting dimension D_0 of $\mathcal{S}$ is then defined by the scaling relation

$$n_{\text{intersecting}}(\varepsilon) \overset{\varepsilon \to 0}{\sim} \varepsilon^{-D_0}, \tag{3.1}$$

where $n_{\text{intersecting}}(\varepsilon)$ denotes the number of ε^N-sized boxes of a regular grid needed to cover $\mathcal{S}$. This relation can be slightly rearranged to make the definition more explicit:

$$D_0 = \lim_{\varepsilon \to 0} \frac{\ln n_{\text{intersecting}}(\varepsilon)}{\ln 1/\varepsilon} \tag{3.2}$$

As we can verify by imagining trivial examples, like, for example, a line or a square, the box counting dimension of non-fractal objects is similar to the usual (non-fractal) definition of dimension.

3.1.2 Generalised Fractal Dimensions and Multifractals

In the previous section we have assumed that the object we want to describe using a fractal dimension is a fractal set embedded in a N-dimensional space. In this section we extend the concept to measures, i.e., real valued functions $\mu : \mathcal{S} \mapsto \mathbb{R}$, where $\mathcal{S} = \text{supp}(\mu)$ and $\mu(\mathcal{S}) := \int_{\mathcal{S}} d\mu = 1$. Examples for such measures are the (un)stable manifold measures introduced in Sec. 2.3 and Sec. 2.5. The distribution of μ on $\mathcal{S}$ can have very intricate features that are not resolved by a metric such as D_0, which only considers the binary property "filled or not filled" of a box but does not distinguish boxes by how much of the measure is contained in them. In this section we introduce two generalisations of the box-counting dimension that fix this shortcoming. We define the spectrum of Rényi dimensions and use it to introduce the concept of multifractality and afterwards shortly discuss an alternative approach – the $f(\alpha)$-spectrum.

The spectrum of Rényi dimensions of a measure μ is defined as follows [Rén55]: As above we use the symbol $\mathcal{S}$ for the support of μ. We further assume that $\mathcal{S}$ is embedded in the connected subspace Ω of $\mathbb{R}^N$ such that $\mathcal{S} \subset \Omega$. Let $\{b_i\}$ be a covering of Ω with non-overlapping ε^N-sized boxes and let $\mu_i := \int_{b_i} d\mu$. Further, let $n(\varepsilon) := |\{b_i\}|$ the number on boxes in the covering and $n_{\text{intersecting}} := \left| \{b_i : \int_{b_i} d\mu > 0\} \right|$ the number

of boxes intersecting $\mathcal{S}$. The spectrum of Rényi dimensions D_q (q is a continuous real valued index) is defined as

$$D_q = \frac{1}{1-q} \lim_{n\to\infty} \frac{\ln \sum_{i=1,\mu_i>0}^{n(\varepsilon)} \mu_i^q}{\ln 1/\varepsilon}, \tag{3.3}$$

where the sum runs only over boxes with $\mu_i > 0$ – a restriction which is necessary only for the case $q = 0$. This spectrum is sometimes also referred to as "generalised fractal dimensions". The dimensions D_q fulfill $N \geq D_q \geq D_{q'} \geq 0$, where $q' > q$ and $q, q' \in \mathbb{R}_0^+$. In the case of a uniformly distributed measure all the dimensions are the same, independently of the choice of q. All measures with $D_q = D_0 \ \forall \ q \in \mathbb{R}$ are called monofractal and their fractality is sufficiently described by any fractal dimension D_q of their support. In the case that D_q depends on the value of q, μ is called multifractal. Some values of q lead to special fractal dimensions:

(i) $q = 0$: Plugging this in leads to a numerator $\sum_{i:\mu_i>0} \mu_i^0$. This is the number of boxes with $\mu_i > 0$, i.e., the number of boxes needed to cover supp(μ), and we obtain the box-counting dimension (see Eq. (3.1)) of the support $\mathcal{S}$.

(ii) $q = 1$: This case needs to be treated separately because the factor $1/(1 - q)$ in Eq. (3.3) is not defined in that case. We define this dimension as

$$D_1 := \lim_{q\to 1} D_q \tag{3.4}$$

which – using L'Hôpital's rule – leads to

$$D_1 = \lim_{\varepsilon\to 0} \frac{-\sum_{i=1}^{n(\varepsilon)} \mu_i \ln \mu_i}{\ln 1/\varepsilon}. \tag{3.5}$$

If we interpret μ_i as the probability that a random variable X assumes a state x_i then the expression in the numerator is the Shannon entropy H_ε of that probability distribution, which is defined as

$$H_\varepsilon := -\sum_{i=1}^{n(\varepsilon)} \mu_i \ln \mu_i. \tag{3.6}$$

Therefore, D_1 describes the growth of information content as the number of boxes is increased, and for that reason it is often called *information dimension*.

(iii) $q = 2$: The case

$$D_2 = \lim_{n\to\infty} \frac{\ln \sum_{i=1}^{n(\varepsilon)} \mu_i\mu_i}{\ln \varepsilon} \tag{3.7}$$

is called *correlation dimension* because if μ is a natural measure the summands in the numerator here are proportional to the probability that two trajectories end up in the same box, i.e., within a distance ε. It is often used in numerical dimension estimations (see for example Sec. 3.2.1.2) because there are efficient algorithms to compute it. It gives a lower bound to the numerically much less accessible D_0 – or even the same result in the monofractal case.

For other values of q there are no such intuitive interpretations. In general, the parameter q gives more (less) weight to the boxes that contain more measure the larger (smaller) it is. For example, in the limit $q \to \infty$ the sum is dominated only by the box or boxes b_j with $\mu_j = \max(\{\mu_i\})$.

An alternative but equivalent way of describing the multifractality of a measure is given by the $f(\alpha)$ spectrum [HJK$^+$86b, HJK$^+$86a]. To define it we first need to introduce the point-wise dimension, which is defined as

$$D_{\mathrm{P}}(x) := \lim_{\varepsilon \to 0} \frac{\ln \mu(\mathcal{B}_\varepsilon(x))}{\ln \varepsilon}. \tag{3.8}$$

This dimension describes the change of the measure contained in an ε-sized ball $\mathcal{B}$ around the point x as ε is changed. Now consider the set $\mathcal{C}_\alpha$ of points in the support $\mathcal{S}$ of μ that have a point-wise dimension close to α:

$$\mathcal{C}_\alpha := \{x \in \mathcal{S} : |D_{\mathrm{P}}(x) - \alpha| < \delta\}, \tag{3.9}$$

with $\delta \to 0$. We define a function $f(\alpha)$ which returns the box counting dimension of this subset:

$$f(\alpha) := D_0(\mathcal{C}_\alpha) \tag{3.10}$$

The knowledge of $f(\alpha)$ is equivalent to knowing the full D_q spectrum as they can be transformed into each other using c

$$\left. \frac{d}{d\alpha'} \left(q\alpha' - f(\alpha') \right) \right|_{\alpha' = \alpha(q)} = 0 \tag{3.11}$$

and

$$\left. \frac{d^2}{d\alpha'^2} \left(q\alpha' - f(\alpha') \right) \right|_{\alpha' = \alpha(q)} > 0, \tag{3.12}$$

which leads to

$$D_q = \frac{1}{1 - q} \left(q\alpha(q) - f\left(\alpha(q) \right) \right). \tag{3.13}$$

Both treatments are equivalent but as we will see in Sec. 3.2 sometimes the point wise dimension is numerically more accessible.

3.1.3   Application of Rényi Dimensions in Open Chaotic Systems

Fractals are omnipresent in nonlinear dynamics [AVS09]; for an overview, see Sec. 1.1. Here we show two important relations that illustrate how fractal dimensions allow to link the geometry of structures in the phase space with the underlying dynamics.

Historically, the first use of dimensions in the characterisation of asymptotic measures comes from the study of chaotic attractors. Those can be found in dissipative systems and their natural measure is defined as the probability of finding a typical trajectory in a given region of the phase-space. The Kaplan-Yorke formula [FKYY83] gives an expression of the information Dimension D_1 of this measure in a system in terms of its Lyapunov exponents λ_i. Let

$$k := \max \left\{ j \in \mathbb{N} : \sum_{i=1}^{j} \lambda_i > 0 \right\} \tag{3.14}$$

be the index after which the sum becomes negative. Then D_1 is given by

$$D_1 = k + \frac{\sum_{i=1}^{k} \lambda_i}{|\lambda_{k+1}|}, \tag{3.15}$$

which for two-dimensional maps reduces to

$$D_1 = 1 + \frac{\lambda_1}{|\lambda_2|}. \tag{3.16}$$

This relation is very significant, because it made a connection between a geometrical property – the fractal dimension – and dynamical properties of the system.

In open systems a similar formula exists. The Kantz-Grassberger relation [KG85] connects the information Dimension D_1 of the natural measure of the saddle in a two dimensional system with the escape-rate κ and the Lyapunov exponents λ_1, λ_2

$$D_1 = (\lambda_1 - \kappa) \left(\frac{1}{\lambda_1} + \frac{1}{|\lambda_2|} \right). \tag{3.17}$$

In the case of a closed system, we have $\kappa = 0$ and we recover Eq. (3.16). A generalisation for the case of true-time maps with partial absorption was recently proposed in [APT13a].

As we will see later in this work, in open quantum chaotic systems the fractality of the classical dynamics appears in the distribution of eigenstates [CMS97] and in the Weyl law [LSZ03]. The latter we discuss in detail in Ch. 6, so we omit a further description here. In very basic terms we can summarise the influence of fractal invariant

structures in this way: Exceptionally long and short lived states in quantized chaotic systems localise on an equivalent to the classical phase-space in regions that contain a majority of the stable-manifold and unstable-manifold measure, respectively. As a result, the scaling of the number of such states with the dimension of the associated Hilbert space is determined by certain fractal dimensions of those measures.

3.2   Numerical Dimension-Estimation

Over the years a variety of algorithms was devised to numerically estimate fractal dimensions in different contexts. Some of them are tailored to a specific setting like for example time series analysis, while others are more general. In the following we discuss the algorithms most commonly used in the context of dynamical systems. We compare them in terms of their ability to calculate fractal dimensions of conditionally invariant stable manifold measures – as defined in Eq. 2.22 and Eq. 2.25 – of fully and partially open chaotic systems of the kind introduced in Ch. 2. The first of these measures is the natural stable manifold measure μ_{ns} defined as the density of surviving points and the other one (μ_{s}) is proportional to the average leftover intensity in a particular region. Since the escape of a trajectory can be expressed by setting the associated intensity to 0, in fully open systems, the fraction $\mu_{i,t}$ of either of those measures contained in a phase-space region b_i at the time t is proportional to the average intensity after a time t of the trajectories started from this box at $t = 0$.

We assume that the measures are not analytically known because that is typically not the case. Therefore the measure needs to be numerically estimated which means that a large number of trajectories needs to be iterated for a sufficiently long time in order to get a good estimate of $\mu_{i,t}$ and its support. The exponential decay of the survival probability in chaotic systems makes it very hard to find long enough trajectories in fully open systems, so that the sample size in a brute force sampling of the full phase space is not a viable option if the support of μ is sparse. The algorithms presented in Sec. 3.2.1.3 and 3.2.1.4 avoid the sampling in the full phase space by generating sampling on the fly and only in parts of the phase space.

In partially open systems, however, the support of the measure is not sparse, so that a sampling in the full phase space or at least along a cross section is necessary. Because of that we start the discussion with known algorithms acting on a pre-sampled set. In Sec. 3.2.2 we present a parallelisable approach to pre-sample sparse measure distributions.

3.2.1 Known Algorithms

In the following we give an overview over the algorithms most widely used for dimension calculation. We assume that the intensity associated $I_t(x_0)$ to a trajectory starting at x_0 is accessible only through numerical forwards evolution of the point. If the system is fully open $I_t(x_0) = 1$ for $t \leq t_{\text{esc}}$ and $I_t(x_0) = 0$ afterwards. We further assume that the system is at least partially chaotic. There are three main contributions to the computational cost associated to the numerical dimension calculation (see for example [Ott08, MLCVHÁ02]). The first contributor simply is the iteration of the trajectories. It grows linearly with the desired iteration time t. The second contribution comes from grouping the trajectories into boxes or comparative methods to calculate the function used to estimate the dimension. As we show in the following review efficient algorithms apply different strategies to minimize either one of the two or both contributions. The third, and in most cases most severe contribution to the numerical cost is the expense of trying out (i.e. iterating) a sufficiently large number of initial conditions.

For the numerical examples in this section we use a fully open tent map defined as

$$
x_{n+1} = \begin{cases} 2x_n & \text{for} \quad x_n < \frac{3}{4} \\ 6(1 - x_n) & \text{for} \quad x_n \geq \frac{3}{4} \\ \text{escape} & \text{for} \quad x_n \geq 1 \end{cases}
\tag{3.18}
$$

$$
t_{n+1} = t_n + 1.
$$

This map is analytically treatable as we will discuss in detail in Sec. 4.2. For this chapter the relevant analytical result is that for this choice of parameters the fractal dimension of the stable manifold is that of the middle third cantor set $D_0 = \ln 2 / \ln 3$. As a more general example we use a open stadium billiard (see Sec. 2.4) with $r = 1$ and $L = \pi$. Since the particular choice of parameters is not important for the results in this chapter – as long as $L, r > 0$ – we have picked values that make the area in phase space belonging to the arc section similar to that belonging to the straight section. For the billiard we use the extended true-time map defined in Eq. (2.23) with $R(s, \sin \vartheta) = 0$ inside the hole and $R(s, \sin \vartheta) = 1$ everywhere else.

3.2.1.1 Brute Force Sampling and Box-By-Box Evaluation

The numerical approach described here is less of an algorithm than it is a straightforward application of the definitions presented in 3.1 on a fractal measure μ which needs to be available before the algorithm is applied. In its most simple form the sampling and dimension calculation follows a procedure like this:
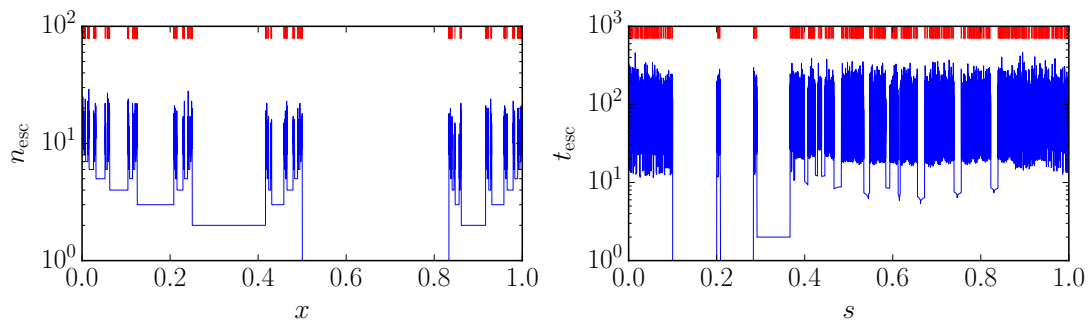
FIGURE 3.2: Blue: numerically calculated escape time distributions in (left) the asymmetric tent-map (see Eq. (3.18)) and (right) a leaky stadium ($R = 1, L = \pi$ with a hole at $0.1 < s < 0.2$); for the billiard we chose the line defined by $\vartheta_0 = 2\pi/3$. To give a better representation of the strong fluctuations we connected the points of the escape time distributions which were sampled using 10^5 i.i.d. initial conditions uniformly distributed on $[0, 1[$. Red: markers for the location of trajectories that survive longer than some threshold ($t_{\text{esc}} > 15$ in the tent map and $t_{\text{esc}} > 200$ in the billiard).

1. Chose a time t^* that is large enough that the sampling yields a sufficiently good approximation of the asymptotic behaviour; chose t^* as small as possible to minimize the computational cost of iterating the system.

2. Pick an initial condition x and iterate it until its associated intensity reaches zero (i.e. the trajectory escapes) or up to $t_n \geq t^*$. Repeat this step until we have a large enough sample size ς of points with $t_{\text{esc}} \geq t^*$ for a good approximation of the measure.

After these steps the sampling part of the dimension calculation is finished. In Fig. 3.2 we sketch the sampling procedure. The size of the approximation of the trapped set at this sample size is roughly 350 points in the tent map and around 700 in the stadium. Both values are three orders of magnitude smaller than the total number of samples (10^5) which already hints at the low efficiency of this approach for sparse sets. From here on the steps are independent of the sampling method but the outcome still depends on the quality of the sampling, i.e., usually the sample-size. What follows is a numerical evaluation of D_q (see Eq. (3.3)) which is defined in the limit of $\varepsilon \to 0$ by looking at the scaling of a q-dependent function $f_q(\varepsilon, \mu)$ with ε at finite box-sizes. What choice of t^* and what range of box-sizes is leading to an accurate estimation at a decent computational effort is discussed in detail in Ch. 4.

3. For a wide range of box-diameters $\varepsilon \leq 1$ completely cover the embedding space with a regular grid of non-overlapping boxes b_i of volume ε^N, where N is the phase-space dimension.[3]

---

[3]It is not necessary to sample the full N-dimensional phase-space if the measure is constant along the stable manifold. In that case the calculation of the dimension can be done on an $(N-1)$-dimensional subspace intersecting the stable manifold. We do not specifically discuss the latter case below, but all the arguments are easily applied there by replacing N with $N-1$.

4. In every box approximate the measure as the normalised average intensity of trajectories that started in that box. This means that in general every initial condition x that was randomly drawn needs to be checked for the conditions $I_{t^*}(x) > 0$ and $x \in b_i$.

5. Calculate $f_q(\varepsilon, \mu) := \sum_{i:\mu_i>0} \mu_i^q$ with $q = 0$ for the box-counting dimension or with $q \in \mathbb{R}$ for any of the Rényi dimensions.[4].

6. Find the scaling exponent D_q that best describes the observed scaling $f_q(\varepsilon, \mu) \sim \varepsilon^{-D_q}$; either by a method like least square fitting of a line in log-log-space or by averaging over local slopes $\Delta \ln f_q / \Delta \ln \varepsilon$ between different box-sizes.

This method of calculating the Rényi dimensions has the benefit that it is very easy to implement and very robust. It is also very general in the sense that it can be applied to different kinds of measure with only minor modifications to steps 1 to 4. Its main downside is connected to its generality: Because no information about the origin of the measure is considered, it checks all $n(\varepsilon) = \varepsilon^{-N}$ boxes covering the phase-space. The number of filled boxes –i.e. the support of μ – by definition of the box-counting scales as ε^{-D_0} and in most open chaotic systems D_0 is much smaller than N. This means in cases where D_0 is considerably smaller than N it wastes a lot of computational effort checking empty boxes unnecessarily. In the next section we review two alternative approaches that are – at the sacrifice of some generality – much more efficient if μ fulfills some criteria. In Sec. 3.2.2 we propose a variant of this algorithm that makes it more efficient while preserving the generality.

3.2.1.2   The Grassberger-Procaccia Algorithm

A lot of the development of fractal dimension algorithms was done in the attempt to calculate the fractality of strange attractors (i.e., fractal asymptotic sets in contracting systems). It became obvious very quickly [GWSP82] that the straightforward application of box-counting algorithms is not practical because of the sparseness of the attractor in the phase-space and the associated rapid scaling of the unnecessary computational cost for checking empty boxes. In this section we present a class of very successful algorithms based on the correlation sum that allow a much faster estimation of the fractality that are commonly referred to as "Grassberger-Procaccia(-Theiler) Algorithm".

---

[4]The $q = 1$ case needs to be treated slightly different; see Eq. (3.5)

It was introduced[5] [GP83] as an efficient way to estimate the correlation dimension D_2 of strange attractors. Here, the measure these algorithms act upon is a finite-time approximation of the natural measure of the stable manifold (i.e. the distribution of surviving initial conditions in the phase space), not the intensity based measure that we study in partially open systems. As $D_{q'} \geq D_q$ for $q' > q$, the value of D_2 can be used to give a lower bound for the box-counting dimension of the support of μ. In the case of monofractal measures, i.e. if $D_q = D_0 \,\forall\, q$, we can use this algorithm to calculate the box-counting dimension of the set directly. In many multifractal cases, however, the D_q spectrum is flat enough, in which case $D_0 \approx D_2$ and it can be considered a good approximation of D_0.

The Algorithm in its original monofractal-oriented form is based on the correlation sum: Let $\tilde{\mathcal{S}}_t$ be a sampling approximation of the time-t forward trapped set $\mathcal{S}_t$ (for example obtained from a procedure similar to the first steps of the algorithm described in the previous section) with $\varsigma := \left| \tilde{\mathcal{S}}_t \right|$ points. The correlation sum $C(r)$ on $\tilde{\mathcal{S}}_t$ then is the following sum over all pairs of points $x_i, x_j \in \tilde{\mathcal{S}}_t$:

$$C(\varepsilon) = \frac{1}{\varsigma^2} \sum_{i,j:i\neq j}^{\varsigma} \Theta(\varepsilon - |x_i - x_j|), \tag{3.19}$$

with

$$\Theta(\xi) = \begin{cases} 1, & \xi > 0 \\ 0, & \xi \leq 0 \end{cases}. \tag{3.20}$$

The value of $C(\varepsilon)$ is the fraction of points within a distance ε from each other and therefore the scaling exponent D_2 in $C(\varepsilon) \propto \varepsilon^{-D_2}$, is the *correlation dimension* (c.f. Sec 3.1.2) of $\tilde{\mathcal{S}}_t$. As with any algorithm based on finite sample-size approximations, the sample size limits the accessible range of ε and can introduce spurious dimensions that can be avoided by requiring a minimum distance in the sum in Eq. (3.19) [The86].

The algorithm can be made more efficient by – instead of comparing all pairs – pre-ordering the x_j in bins and only comparing distances in neighbouring bins [The87, Gra90]. This sort off approach which is sometimes called "Theiler algorithm" reduces the numerical effort from $\mathcal{O}(\varsigma^2)$ to $\mathcal{O}(\varsigma \ln \varsigma)$. Later, an adaptive version [Cor00] using a variable number of points at different scales as well as improved versions based on different data-structures for the pre-ordering [FSM01, BOPG07] of the points were proposed and implemented.

---

[5]For the sake of completeness, we mention that according to, e.g., [The90], Floris Takens independently published a similar algorithm in a paper called "Invariants related to dimension and entropy" published in *Atas do 13° Colóqkio Brasiliero do Mathemática*, Rio de Janeiro (1983), which we can not access at the time of writing.

The algorithm can also be used to calculate the D_q-spectrum of the natural measure of the stable manifold by calculating the scaling of

$$C_q(\varepsilon) := \left(\varsigma^{-1} \sum_i \left(n_i(\varepsilon)/(\varsigma - 1) \right)^{q-1} \right)^{1/(q-1)}, \tag{3.21}$$

where $n_i = \sum_{j \neq i} \Theta(\varepsilon - |x_i - x_j|)$ is the number of points ε-close to x_i, instead of $C(\varepsilon)$ above. A generalisation to intensity-based measures is not straightforward for this algorithm.

3.2.1.3 Uncertainty Algorithm and Output Function Evaluation

The algorithms presented in this section are suitable for the calculation of the box-counting dimension D_0 of a fractal boundary [TG06, HP83, OSA$^+$93, MdMGK05]. Historically, the uncertainty algorithm was applied to fully chaotic systems with two holes $\mathcal{H}_1$ and $\mathcal{H}_2$ [BGOB88] and to dissipative systems with multiple attractors, but fractal boundaries appear in many other contexts. The different holes or attractors define different outcome states and the phase space can be divided into disjoint sets of initial conditions that lead to a particular outcome. Following the notation established in the examination of strange attractors, the set of initial conditions leading to a particular outcome is called its basin of attraction In such a system almost every point belongs to one of the basins and the interface between the basins of attraction is typically a fractal. The points belonging to the boundary are the ones that do not end up in any of the defined outcome states and as such are singularities of a function $f : \Omega \mapsto \{o_1, o_2, \cdots, o_n\}$, where $\{o_1, o_2, \cdots, o_n\}$ are the different outcomes. Using the fact that points on the forward trapped set $\mathcal{S}_\infty$ of an open system are the singularities of the function $f(x) := t_{\mathrm{esc}}(x)$ we can use this algorithm for the estimation of D_0 of $\mathcal{S}_\infty$. In the context of fractal dimensions of the intensity based stable manifold measure μ_{s}, the algorithms can be used only for D_0 of μ_{s}. But since they converge quickly they can be used to confirm the results of slower but more general algorithms in the special case $q = 0$. We start the discussion of this class of algorithms applied to $\mathcal{S}_\infty$ on the example of the uncertainty algorithm and later present a second method which is outperforming the uncertainty method in some cases [dMG01].

The estimation of D_0 of $\mathcal{S}_\infty$ using the original uncertainty algorithm follows this procedure:

1. Chose a set $\mathcal{E}$ of values for the box-size $\varepsilon > 0$. Since the dimension is calculated from evaluating the scaling-exponent of the density of the boundary with ε, $\mathcal{E}$ should

be chosen sufficiently dense on a logarithmic scale while at the same time choosing $\varepsilon_{\min} := \min \mathcal{E}$ small enough to ensure a sufficiently close approximation to $\mathcal{S}_\infty$.

2. Fix a value of $\varepsilon \in \mathcal{E}$.

3. Choose a random initial condition x and evolve it until it escapes at $t := t_{\mathrm{esc}}(x)$.

4. Perturb the initial condition in a random direction: $x \to x' = x + \delta$, where $|\delta| = \varepsilon$ and calculate its escape time t'.

5. If $t = t'$ then x is considered a certain point, if not, x is uncertain at the scale given by ε.

6. Repeat steps 3 to 5 until the number uncertain points $n_{\mathrm{uc}}(\varepsilon)$ reaches a given required value. This value is a parameter of the algorithm and should be as large as the desired computational performance allows.

7. Start from step 2 with a new value of ε.

The ratio $r(\varepsilon)$ of $n_{\mathrm{uc}}(\varepsilon)$ to the total number $n_{\mathrm{tot}}(\varepsilon)$ of initial condition chosen in point 3 for each value of ε follows a power law

$$r(\varepsilon) \propto \varepsilon^\alpha \tag{3.22}$$

with $\alpha \geq 0$. The value of α is then obtained by a suitable fitting method and it is the codimension of the boundary in the phase-space. The restriction that $n_{\mathrm{uc}}(\varepsilon)$ must be the same ensures a similar sample size at all scales. The *uncertainty dimension* D_{uc} embedded in a N-dimensional phase-space is defined as.

$$D_{\mathrm{uc}} := N - \alpha \tag{3.23}$$

And its value is similar to the box-counting dimension of $\mathcal{S}_\infty$[6].

In contrast to the previously discussed algorithms that rely on a finite time approximation of $\mathcal{S}_\infty$ this algorithm naturally converges to high escape times with the decrease of ε because – as we will discuss in detail in Ch. 4 – the larger the escape time the shorter the interval it is constant on.

---

[6]It is instructive to consider the case of an N-dimensional space divided by a $N-1$-dimensional barrier. Independent of N, the probability of being ε-close to the barrier on either side is $P(\varepsilon-\mathrm{close}) := 2\varepsilon$. This needs to be multiplied with the probability $P(\mathrm{uncertain})$ that the perturbed point falls on the other side of the barrier. If $N = 1$ the boundary is a point and $P(\mathrm{uncertain}) = 1/2$ because there are only two choices. Accordingly, we expect a scaling of $r(\varepsilon) \sim P(\mathrm{uncertain})P(\varepsilon-\mathrm{close}) = \varepsilon$, i.e., $\alpha = 1$ and $D_{\mathrm{uc}} = 0$. For $N = 2$, $P(\mathrm{uncertain})$ depends on the distance of x to the barrier. It is proportional to the area of an ε-disk around x that is beyond the boundary. Integration over all x within a distance ε of the barrier results in $P(\mathrm{uncertain}) = 1/2$ and $D_{\mathrm{uc}} = 1$. For larger N the calculation is equally straightforward.

The *Output Function Evaluation* algorithm is closely related to the uncertainty algorithm. This method utilises the local slope of $f(x)$ to generate a sampling of the trapped set that is more dense in regions that contain singularities than in regions that do not. Afterwards the dimension of the set is calculated. We discuss the method using the escape time as an output function. It is outperforming the uncertainty method if the reduced dimension

$$D_r := D_0 - (N - 1) \tag{3.24}$$

is smaller than $1/2$, where D_0 is the fractal dimension of the trapped set [dMG01].

To keep the notation clean, we here restrict the discussion to the one-dimensional case, which in a 2D system corresponds to the calculation the reduced dimension (i.e. the dimension along a line intersecting the manifold) of the stable manifold of the saddle. In that case the algorithm works as follows:

1. Pick an initial condition x at the beginning of the line and calculate its outcome $f := t_{\mathrm{esc}}(x)$.

2. Set $x^* = x + \Delta$, where $\Delta = \epsilon$ in the overall first passage of this algorithm, and ϵ is the minimal allowed step size – a free parameter of the algorithm.

3. Calculate $f^* := t_{\mathrm{esc}}(x^*)$.

4. Approximate the derivative $f' := \frac{f^* - f}{\Delta}$

5. To calculate the step size Δ for the next passage, first introduce the intermediate variable

$$\xi := \min \left(\frac{\delta}{|f'|}, \alpha \Delta \right) \tag{3.25}$$

so that ξ is either the distance in which f changes by $\pm \delta$, or α times the previous step size. $\alpha > 1$ is a further parameter of the algorithm.

6. Set the next step size to

$$\Delta = \begin{cases} \epsilon & \text{if} \quad \xi < \epsilon \\ \Delta_{\max} & \text{if} \quad \xi > \Delta_{\max} \\ \xi & \text{else.} \end{cases} \tag{3.26}$$

where $\Delta_{\max}$ is the chosen maximum step size (also a parameter of the algorithm).

7. Store x^* and f^* and continue from step 2 with $x := x^*$ and $f := f^*$ until x lies outside of the range of interest.
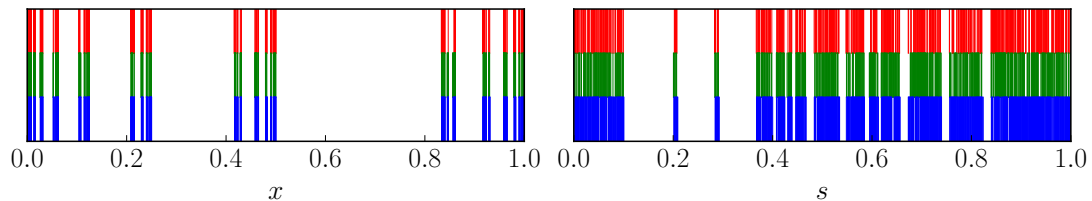
FIGURE 3.3: Sets resulting from (red) brute-force sampling, (green) uncertainty method with $\varepsilon = 10^{-6}$, and (blue) output function evaluation.

8. Remove all points that do not change the outcome significantly from the two sets containing all points $\{x_i\}$ used and output-function values $\{f_i\}$ calculated in to create the new set

$$\Omega = \{x_i : |f_i - f_{i-1}| > \beta\} \tag{3.27}$$

with an appropriately chosen $\beta > \delta$.

The set Ω generated in this way is made up of points which oscillate on scales we can not resolve at a given ϵ or in other words $\frac{\delta}{|f'|} < \epsilon$ in (3.25). We can now apply a box-counting or Grassberger-Procaccia algorithm on this set. In both cases the number of points that needs to be checked is much lower than if uniform random sampling would be used because points far from the stable manifold are removed from the sample in step 6.

To illustrate the algorithms, in Fig. 3.3, we show a comparison of approximations to the stable manifold obtained by steps 2 to 5 of the uncertainty algorithm and by the output function evaluation method. We stop the uncertainty algorithm once n_{uc} reaches the size of the brute force approximation from Sec. 3.2.1.1. The number of total samples to find the 350 (700) uncertain points is around 2×10^3 (4.5×10^4) in the stadium (tent map), which is significantly lower than what the brute force approach required which is of the order of 10^5. While in the tent map, a pair of points is uncertain if the two escape times are different, in the true-time billiard map, the number depends on the definition of a uncertain point. We use the approximation for the average inter-collision distance of the closed stadium [LS90, MLS93] and consider two points different if their escape times fulfill $|t_1 - t_2| > 2\pi/3$. With the output function evaluation method it is less simple to control the number of points. To get sets of a similar size than with the brute force attempt we restrict the minimal step size to $\epsilon \approx 10^{-4}$. This leads to an approximation approximately 400 (1000) points of the stable manifold of the tent map (stadium) at the expense of a total of approximately 4000 (1500) calculated trajectories. While this parameter choice leads to the same number of points than brute force sampling and uncertainty method and to a qualitatively similar picture of the set in Fig. 3.3 at a

much lower cost, the cut-off in inter-sample distances introduced by this choice of ϵ also restricts the box-sizes that can be used with the set.

3.2.1.4 GAIO Algorithms

Other than the algorithms discussed so far which are relatively independent of the dynamics that create the fractal distributions, the following method is specifically targeted to the calculation of D_0 of invariant sets in dynamical Systems. It is part of a set of algorithms which are presented in [DFJ00]. Because of its clearly defined field of application it is less general than the methods before. At the same time this lack of generality allows us to use properties of the dynamical system to improve the performance of the algorithm. Furthermore, its computational cost does not depend strongly on the dimension of the phase space. In the following we discuss the general procedure and results from its application to our two model system.

The algorithm is split in three main parts: first, a more and more refined covering of the chaotic saddle is constructed utilising the fact, that the saddle is invariant under the dynamics. In the second part this covering is iterated backwards to generate an approximation of the stable manifold at the same resolution. Then a box-counting method with a increasingly coarse resolution is applied.

In practise the following steps are applied.

1. Pick an initial box-size ε larger than the desired resolution of the approximation and cover the full phase space with disjoint boxes of that size.

2. Remove any boxes that are entirely in the hole, if such boxes exist.

3. In each box of the current selection[7] of boxes pick random initial conditions and iterate them backwards once until either some maximum number of trials in that box is reached or an initial condition is found for which its pre-image lies within a box of the current collection of boxes.

4. Discard all boxes where no pre image within the current selection is found and divide the remaining boxes into smaller ones.

5. Repeat steps 3 and 4 until a predefined small enough box-size $\varepsilon_{\min}$ is reached.

The steps so far result in an approximation of the saddle at a resolution defined by $\varepsilon_{\min}$. It is made up from the set $\mathcal{A}$ of surviving – i.e., self-intersecting – boxes of size $\varepsilon_{\min}$. To

---

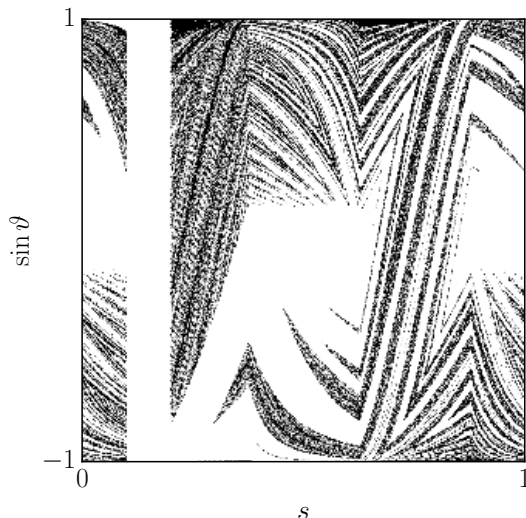[7]In the first passage of the algorithm that means all boxes from step 1.

FIGURE 3.4: GAIO approximation of the stable manifold in the open stadium.

get the stable and unstable manifolds this approximation needs to be iterated, e.g., in the following way:

6. Cover the phase-space with boxes of size $\varepsilon \geq \varepsilon_{\min}$

7. Pick a number ς of initial points inside the boxes contained in $\mathcal{A}$.

8. Iterate this batch of points until the trajectories either escape or reach a maximum length t^* – either forwards to approximate the unstable manifold or backwards for the stable manifold of the saddle-approximation $\mathcal{A}$. After each iteration mark the boxes that contain any of the trajectories. If the number of marked boxes saturates the iteration can be terminated here.

The last three steps result in a approximation of a ϵ-covering of the (un)stable manifold. As an example, in Fig. 3.4 we show the approximations to the stable manifold obtained using the two parts of this algorithm. We used $\varepsilon_{\min} = 2^{-10}$ and a maximum of 10^5 samples per refinement level in steps 1 to 5. Overall this amounts to $\sim 5 \cdot 10^5$ iterations performed to arrive at the saddle and roughly the same number again to get this picture. From here on we can go upwards to larger box-sizes by combining neighboring filled boxes to new boxes to obtain the covering at increasingly coarse resolutions. By going up the subdivision tree that created the small covering in the first place in the opposite direction we obtain from this method the box-counting dimension without needing to check all points of the approximation to determine if the boxes contain a point or not. The algorithm can further be used to calculate the natural measure of chaotic saddles and approximate attracting sets with minor modifications [DFJ00].

3.2.2   Tree Based Algorithm Suitable for Partially Open Systems

In Sec. 3.2.1 we have discussed the major known algorithms. They all have advantages and disadvantages, that we summarise again in Sec. 3.2.3. What they all have in common is that they are not applicable to intensity based measures such as μ_{s} (see Eq. (2.25)) in a straightforward way. The only method that can be applied to such measures is the brute-force box-counting method described in Sec. 3.2.1.1. As mentioned above, this method is also the most inefficient if applied to sparse sets. In the following we propose a derived variant of the algorithm that keeps its generality, but also makes it more efficient in that case. A main feature of the algorithm is that – similarly in spirit to the GAIO method above – we use the iterations of a refinement tree as boxes. This makes the calculation of the dimension after the sampling steps very efficient, since the found initial-conditions are already binned.

First let us only consider the case of sampling a sparse fractal set that is the support of a natural measure μ. The basic idea of the algorithm is to use uniform sampling but to only refine the search in non-empty areas: Let S be the number of samples we want to draw on some support.

1. Cover the support with an ε-grid consisting of n_b boxes.

2. In each box sample at most $\lceil S/n_b \rceil$ and at least some fixed number of points and stop sampling in this box as soon as a point from the set is found.

3. Cover the support with an ε-grid consisting of $n_b' > n_b$ boxes. In this step we usually divide each box in half along each dimension but other factors are sometimes useful, too.

4. Mark every box as empty that does not intersect a box from the previous covering that contained a point. Optionally, mark every box as filled which contains any of the previously successful samples.

5. Distribute the remaining number of samples on the still undecided boxes and continue the refinement process until S points were sampled or until a certain resolution in ε is reached

A sketch of this sampling procedure can be seen in Fig. 3.5. In this figure we already hint at the main improvement over uniform sampling in the full phase space. Namely, in boxes, which contain large parts of the set, the number of necessary samples is smaller than in less densely populated areas. This can be observed on the example systems used throughout this chapter in Fig. 3.6. In this figure we can clearly see, that the histogram
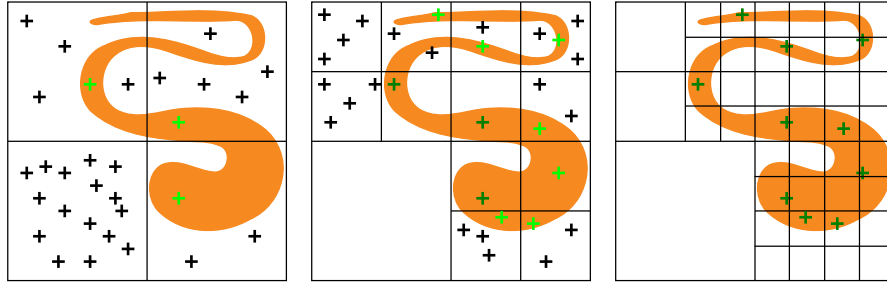
FIGURE 3.5: Three subsequent steps of the tree based algorithm; left and middle panel: The set (orange), samples which are not in set (black +), and samples which are (light and dark green +) at different depth levels of the algorithm. Right panel: next step of the refinement and already found points.
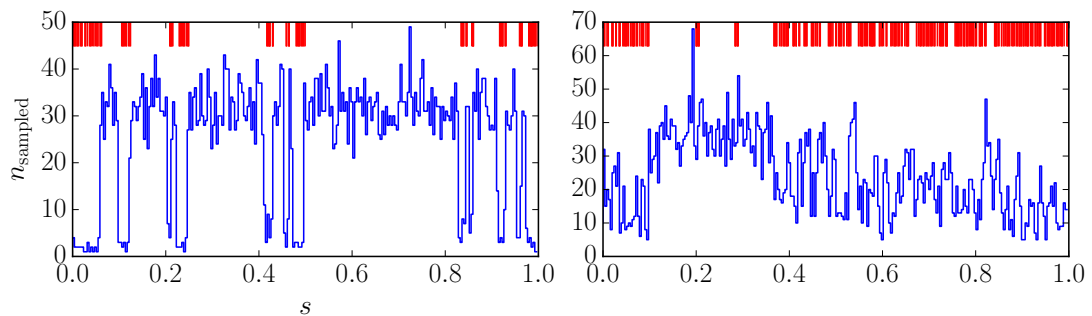

FIGURE 3.6: Blue:Number of samples needed for tree method approximation of stable manifold in (left) the tent map and (right) the stadium. Red: Resulting approximation. The minimal box-size here is 2^{-8}.

shows dips where the set is dense. In contrast to the discussion in Sec. 3.2.1, we have chosen shorter cut-off times here, to make the fluctuations more visible.

After this sampling is finished D_0 can be calculated by going up the refinement tree used in the sampling. This procedure allows a quick calculation of the number of filled boxes at each level, because the edges of the boxes between different levels align. I.e., instead of having to check all points, the algorithm checks only the boxes one level below.

For the computation of D_q of the intensity based measures μ_s defined in systems with partial leaks, there are only slight modifications necessary. Since in this case the support of μ_s is the full phase space we can skip the sampling during the refinement. Instead, we start at the leaves of the refinement tree (i.e. at some minimum ε) and sample a fixed number of initial condition in each. The initial condition are then iterated up to some fixed time. After all boxes are treated that way, we calculate the measure of each box. Then, to calculate a D_q we go upwards in the tree, assigning each box the sum of the measures of the boxes it contains. This method naturally lends itself to a distributed computing implementation since each leave can be computed independently

from the others.

3.2.3   Comparative Discussion of the Algorithms

In the following we want to summarise advantages and disadvantages of the algorithms presented in Secs. 3.2.1 and 3.2.2.

First let us consider the brute-force box-counting approach and the Grassberger-Procaccia algorithm. As mentioned above, if the two algorithms are applied to the same sampling approximation of a fractal set, the Grassberger-Procaccia algorithm is much more efficient. Its main disadvantage over the brute force method is, that it does not return D_0 but only a lower bound given by D_2. In cases where the D_q spectrum is flat, this is often a good approximation. If the fractal under consideration is located at the singularities of some function, then a method like the uncertainty method or the output-function-evaluation method can be used to provide a better sampling approximation than provided by brute-force sampling. If the fractal is generated by a dynamical system, then the GAIO method is most suitable to calculate a covering of the set, because it is the only method that explicitly uses dynamical properties.

The tree method presented in the previous section in most scenarios cannot compete with the efficiency of the long optimised methods above in the estimation of D_0 of a natural measure. Its main advantage lies in its generality. It can be applied to any measure distribution and is easily implemented and parallelised.

It is important to note, that the efficiency of most methods (with the exception of the GAIO algorithm) is based on making efficient use of the available samples. For example the Grassberger-Procaccia algorithm is faster than the brute force method because it minimizes the number of comparisons between points. Nonetheless, in dynamical systems, they are all subject to constraints coming from the dynamics itself. In the next section we will investigate in detail these constraints and their dynamical and statistical origins. The results obtained from these investigations provide a deeper understanding of the algorithms summarised above.

Chapter 4

Effective Dimensions in Open Chaotic Systems

In this chapter we introduce an effective dimension defined away from the usual asymptotic definition, i.e., at finite sample-sizes, finite box-size, and finite time. Effective fractal dimensions that depend on the length scale with which they are observed have been previously considered in weakly chaotic systems [LFO91, MLG03, KMBK13, MdMGK05], general computer science [Lut05, AHLM07], and statistical surface analysis [Pfe84, CH94, MA84]. The influence of finite sample sizes on the observed dimension has been studied in [Gra88, LT89]. In the following we argue that all of the three finite parameters can be expressed in terms of length scales, related to each other, and used to obtain a useful definition of the effective dimension.

While they are seemingly straight-forward, the definitions of the box-counting dimension in Eq. (3.1) and spectrum of Rényi dimensions in Eq. (3.3) contain several assumptions, e.g., $\varepsilon \to 0$ that are usually not met when we study physical fractal objects or numerical models. In the following we will show that in most cases the strict application of the definitions leads to trivial results in the sense that they do not provide information about the underlying dynamics. Usually, the analytical calculation of a fractal dimension is not possible and we need to use numerical dimension estimation algorithms such as the ones presented in Sec. 3.2. All the common algorithms have parameters that need to be chosen carefully in order to produce a relevant result. In this chapter we discuss in detail where the straight-forward application of the definition fails to teach us something insightful about physical fractals and how we can pick up the relevant information numerically, i.e., which are the optimal parameter-ranges of an algorithm. We show that this parameter range not only tells us where we can trust the numerics, but that it also defines an effective fractal dimension that is an intrinsic

property of the dynamical system. We will mostly focus on the box-counting dimension D_0 to keep the notation clear but as we will see later in the chapter the concepts apply to multifractals as well.

The definitions of fractal dimensions in Eqs. (3.1) and (3.3) contain the limit of infinitesimal box size $\varepsilon \to 0$ or, equivalently, infinite number of boxes $n(\varepsilon) \to \infty$ that make up the covering of the phase space used in the calculation of the box-counting dimension. Physical objects, however, are never endlessly self similar, e.g., because they undergo only a finite number of branchings or iterations until they reach a minimal feature-size. Such objects are only fractal down to some minimal scale below which they assume an integer dimension and thus the $\varepsilon \to 0$ limit is trivial. Such a minimal feature-size also appears in numerical computations, e.g., if the fractal set is computed by the iteration of initial conditions in a chaotic system where a truncation in the resolution of the fractal appears because of computational limitations. The fractal dimension (at $\varepsilon \to 0$) of such truncated fractals is equal to the dimension of the remaining features which, in turn, is usually the phase-space dimension. We will in the following use $D_{\varepsilon \to 0}$ for the fractal dimension of an object that results from a strict application of the definition. In contrast, we consider a ε-dependent dimension. In the case of a truncated fractal this leads to an effective dimension for "large" ε:

$$n_{\text{intersecting}} \sim \varepsilon^{-D_{\text{eff}}(\varepsilon)}, \tag{4.1}$$

where $n_{\text{intersecting}}$ is the number of disjoint boxes needed to cover the set. In general, we will use $D_{\text{eff}}(\varepsilon)$ when we talk about the local (in ε-space) scaling if this scaling is not equal to $D_{\varepsilon \to 0}$.

The second assumption is less apparent: the definitions of $D_{\varepsilon \to 0}$ and $D_{\text{eff}}(\varepsilon)$ implicitly assume that we know the measure μ_i of each box or – in the case of box-counting – which box intersects the fractal set. In most cases, however, our knowledge of the fractal distribution is limited. For example, if the data comes from an experiment or from a simulation it is limited to a finite number ς of points. Even if we run numerical simulations that generate samples on the fly – and therefore can control ς – the accessible sample-size is limited by computational power. As a result of this, the observed dimension $D_{\text{obs}}(\varepsilon, \varsigma)$ can differ significantly from the "real" dimension of the set which we will call $D_{\varsigma \to \infty}(\varepsilon)$ from now on (note that $\lim_{\varepsilon \to 0} D_{\varsigma \to \infty}(\varepsilon) = D_{\varepsilon \to 0}$, and away from that limit: $D_{\varsigma \to \infty}(\varepsilon) = D_{\text{eff}}(\varepsilon)$). A lack of data points necessarily leads to $D_{\text{obs}}(\varepsilon, \varsigma) \xrightarrow{\varepsilon \to 0} 0$ for finite ς, i.e., the dimension of a point. At which box-size ε this transition takes place depends on the sample size, so that we can expect that there exists an ς-dependent range of box-sizes for which we can observe $D_{\text{obs}}(\varepsilon, \varsigma) = D_{\varepsilon \to 0}$ and $D_{\text{obs}}(\varepsilon, \varsigma) = D_{\text{eff}}(\varepsilon)$. In case we sample the fractal on the fly we can formulate the problem in the reversed way:

How many samples do we need to perform if we want to observe the non-trivial effective dimension of a particular fractal distribution down to a certain minimal box-size?

An additional interesting type of behaviour appears if the fractal depends on the escape-time, as it is the case in finite-time approximations of trapped sets and conditionally invariant measures of open chaotic systems. In such fractals the typical feature size changes with the escape-time chosen for such an approximation, and the ε-dependence of $D_{\mathrm{obs}}(\varepsilon, \varsigma)$ changes accordingly. Additionally, the number of samples needed to approximate the fractal to sufficient precision in the sense that the observed dimension is close to the real one is a function of that cut-off time.

In this chapter we discuss the questions *"What is the optimal range of box-sizes?"* and *"How many samples do I need?"* in more detail. We will first discuss the interplay between these two questions in open chaotic systems in general. We then present analytical arguments on the calculation of fractal dimensions in a class of systems where such an analytical treatment is possible and compare it to numerical calculations. After that we show on the example of an open billiard that the observations from these simple systems can be used to numerically obtain the fractal dimensions of more complicated systems and that we can identify the parameter ranges yielding D_{eff}. For the most part we will base these calculation on cantor-like fractals and monofractal distributions but we will show that our description also applies to more complex and multifractal distributions. The latter we demonstrate numerically on an example of a map with a partially absorbing hole. For the sake of clarity of the discussion we only consider fractals which are either generated by one-dimensional maps or the result of restricting the calculation of two dimensional fractal measures to a one dimensional slice of the phase space. This restriction to one dimensional maps or slices is not necessary – as the presented results are expected to hold in higher dimensional systems as well – but it allows us to express the formalism in a simpler, more didactic way.

4.1 General Theory

In this section we describe the general behaviour of the observed dimension as a function of box-size, sample-size, and escape-time on the illustrating example of the forward trapped set $\mathcal{S}_{\infty}$ and its finite-time approximation $\mathcal{S}_t$ of an open chaotic map $\mathcal{M}$ of the following general form (see Sec. 2.3):

$$\mathcal{M} : (x_n, t_n) \mapsto \begin{cases} (x_{n+1}, t_{n+1}) = (\mathcal{M}_{\mathrm{closed}} x_n, t_n + \tau(x_n)), & \text{if } x_n \notin \mathcal{H} \\ \text{escape}, & \text{if } x_n \in \mathcal{H} \end{cases}, \qquad (4.2)$$
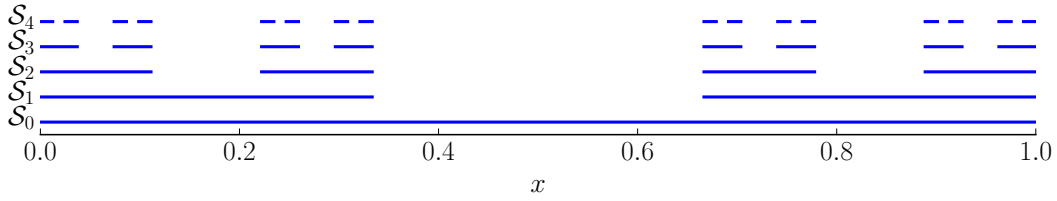
FIGURE 4.1: Surviving sets $\mathcal{S}_t$ in a mapping that at each iteration removes the middle third of every remaining segment.

where $\mathcal{H}$ defines the hole and $\tau(x_n)$ is the time between the nth and $(n+1)$th iteration. For the remainder of this section we assume $\tau(x) = 1$ for all x. We will discuss both an example with a partial leak and an example with non-trivial $\tau(x)$ later in the chapter.

We are interested in strongly chaotic (e.g. hyperbolic) open systems for which the survival probability shrinks exponentially (see Ch.2) for large t:

$$P(t) \sim \mathrm{e}^{-\kappa t}. \tag{4.3}$$

In the infinite-time limit the set $\mathcal{S}_\infty := \lim_{t\to\infty} \mathcal{S}_t$ is the forward trapped set of the system and $\lim_{t\to\infty} P(t) = 0$, i.e., the chance of finding a point belonging to $\mathcal{S}_\infty$ when picking initial conditions distributed uniformly over the full phase space, i.e., a brute force sampling, goes to zero with increasing t.

For finite t, $\mathcal{S}_t$ is made up of objects with the same dimension as the phase space. With increasing time these objects or segments shrink in size but grow in number. In Fig. 4.1 we can see how $\mathcal{S}_t$ changes in an example map which in in the limit $t \to \infty$ creates the Cantor set. Maps like this can be viewed as a tree branch. At each level there are more but smaller branches until they reach a minimal size. For the sake of simplicity we will from here on assume that $\mathcal{M}$ is one-dimensional. This implies that $\mathcal{S}_t$ is shrinking in only one direction along which we observe a time-dependent distribution of segment-sizes $l_{i,t}$ (i is an index numbering the segments) around a typical value $\ell(t)$[1]. For large t this distribution concentrates around $\ell(t)$ and it can be shown that this value scales with the largest Lyapunov-exponent λ [LVA13]:

$$\ell(t) \sim \mathrm{e}^{-\lambda t} \tag{4.4}$$

It is easy to see that in a one-dimensional map for *finite t* the asymptotic dimension is the dimension of a line: $D_{\varepsilon\to0} = 1$ (the dimension of each segment). In chaotic systems the forward trapped set $\mathcal{S}_\infty$ has a fractal dimension. This dimension is equal to the effective

---

[1]In a higher dimensional map there is a typical width for each direction along which $\mathcal{S}_t$ is shrinking and the value of the effective dimension changes each time the box-size passes over a typical size until it reaches the phase space dimension once ε is smaller than the smallest typical size.

dimension D_{eff} of $\mathcal{S}_t$. So box counting on $\mathcal{S}_t$ is expected to yield $D_{\text{obs}} = D_{\varepsilon \to 0} = 1$ for "small" box-sizes and $D_{\text{obs}} = D_{\text{eff}}$ for "large" ε values. The transition between $D_{\varepsilon \to 0}$ and D_{eff} happens approximately at the typical length of segments $\varepsilon \approx \ell(t)$:

$$D_{\text{obs}} = \begin{cases} D_{\varepsilon \to 0} & \text{for } \varepsilon \lessapprox \ell, \\ D_{\text{eff}} & \text{for } \varepsilon \gtrapprox \ell \end{cases} \tag{4.5}$$

As we have mentioned at the very beginning of this chapter the range of box sizes that lead to the effective dimension is further restricted by the number of available data points. We now discuss the influence of finite sampling on our example map $\mathcal{M}$. In a typical scenario we estimate D_{eff} of $\mathcal{S}_t$ at a given value of t. Since we do not know which initial conditions lead to a trapped trajectory we try to sample $\mathcal{S}_t$ by picking S points distributed uniformly over the full phase space and iterate each of them t times or until they escape. Then the number of *successful* samples ς – i.e., the number of initial conditions that belong to $\mathcal{S}_t$ – scales with the survival probability $P(t)$:

$$\varsigma \approx SP(t) = S\mathrm{e}^{-\kappa t} \tag{4.6}$$

This gives us an upper limit for the number $n_{\text{filled}} \leq n_{\text{intersecting}} \leq n(\varepsilon)$ of intersecting boxes that are actually found:

$$n_{\text{filled}} \leq \varsigma. \tag{4.7}$$

This upper limit is simply due to the fact that the number of found boxes can not exceed the number of available data-points. For the observed dimension this implies that if the box-size is small enough such that every filled box contains exactly one of the ς points, then $D_{\text{obs}} = 0$. What "small enough" here means depends on $\mathcal{S}_t$ and on the sampling method used. More precisely, it depends on the distribution of distances between neighbouring data-points around the typical distance which we will call δ in the following. We can summarise our prediction as follows:

$$D_{\text{obs}} = \begin{cases} 0 & \text{for } \varepsilon \lessapprox \delta \\ D_{\varsigma \to \infty} & \text{for } \varepsilon \gtrapprox \delta \end{cases}. \tag{4.8}$$

Intuitively speaking, this provides us with an minimum number of samples we need at a given box size to see the actual dimension of the set (i.e. $D_{\varsigma \to \infty}$) while Eq. (4.5) gives us an lower limit of box sizes that allow us to see the non-trivial effective dimension D_{eff}.

The value of δ depends on the value of $D_{\varsigma \to \infty}$ at $\varepsilon \approx \delta$ so that in the case of a 1D map we have to distinguish two cases:

(i) $\delta < \ell$: In this case $D_{\varsigma \to \infty} = 1$ for $\varepsilon = \delta$, i.e., the transition takes place at box-sizes at which the segments of $\mathcal{S}_t$ look like lines to a box-counting algorithm.

(ii) $\delta > \ell$, i.e., $D_{\varsigma \to \infty} = D_{\text{eff}}$ which describes the case where the box-sizes are large enough for an algorithm to resolve the fractal effective dimension.

Let us first discuss case (i) on the trivial example of $\mathcal{S}_0$ because in that particular case $\ell(t = 0) = 1$ and we can be sure that $D_{\varsigma \to \infty} = 1$ for all box-sizes $0 < \varepsilon < 1$. As described before we distribute ς points on $\mathcal{S}_0$. First, assume that we use a method that creates exactly evenly spaced samples and therefore $\delta = 1/\varsigma$. Here we expect to see a very sharp transition from $D_{\text{obs}} = 1$ to $D_{\text{obs}} = 0$ exactly at $\varepsilon = \delta$. This type of behaviour, i.e., a drop from $D_{\text{obs}} = 1$ to $D_{\text{obs}} = 0$ – albeit less abruptly – is also observed if we distribute the ς points *randomly* on $\mathcal{S}_0$, typically the sort of data available. In the random case we can use order statistics to calculate the distribution of inter-sample distances around the expected value $1/S$ (see App. A). The steepness of the transition in the dimension in that case depends on the distribution of distances between the samples.

We now consider the more relevant case of $\mathcal{S}_t$ for larger but finite t. The area of the set shrinks with the same rate as ς, so that $\delta = 1/S$ continues to hold. At the same time the distribution of gaps in $\mathcal{S}_t$ will include smaller and smaller values as t increases. Once the two distributions overlap we get into the transition denoted by (ii) earlier. That is, we are at box-sizes, where $D_{\varsigma \to \infty} = D_{\text{eff}}$ and we can no longer assume that we sample on a line. Accordingly, the $\delta = 1/S$ estimation based on order statistics used above is no longer valid but we can use a different method to estimate δ. The option we use is to use the upper limit to the number of filled boxes expressed in Eq. (4.7) to estimate the value of δ as the point where the n_{filled} curve reaches ς: So, at $\varepsilon = \delta$ we have $\varsigma \propto \delta^{-D_{\text{eff}}}$ which already gives us the scaling of δ:

$$\delta = C\varsigma^{-1/D_{\text{eff}}} \tag{4.9}$$

The constant C can be calculated from the assumption that the two predictions of δ must match at the point where ℓ and δ cross (as we will see in Eq. (4.14)). So we complete the statements in Eqs. (4.5) and (4.8) by noting that

$$\delta = \begin{cases} 1/S & \text{for } 1/S < \ell \\ C\varsigma^{-1/D_{\text{eff}}} & \text{for } 1/S > \ell \end{cases} . \tag{4.10}$$

The shape of the transition depends on ς and we can generally expect that it is sharper, the larger ς is. We have sketched an example of the typical behaviour of $n_{\text{filled}}(\varepsilon)$ in Fig. 4.2. We show all types of general behaviour that we can observe with a box-counting
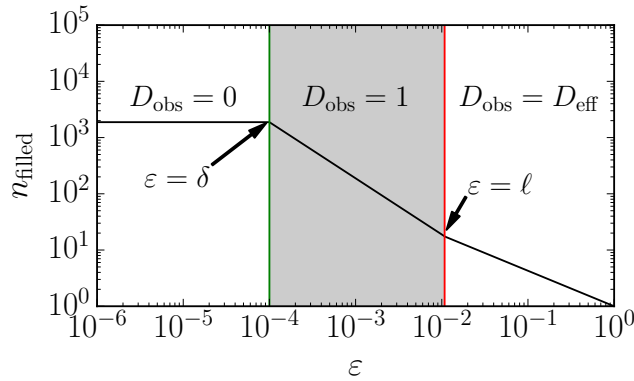
FIGURE 4.2: Typical behaviour of the number of found boxes n_{filled} at a fixed distribution of feature sizes l_i and at a fixed sample-size. The vertical lines mark the transitions between the different values of D_{obs} as described in Eqs. (4.5) and (4.8).
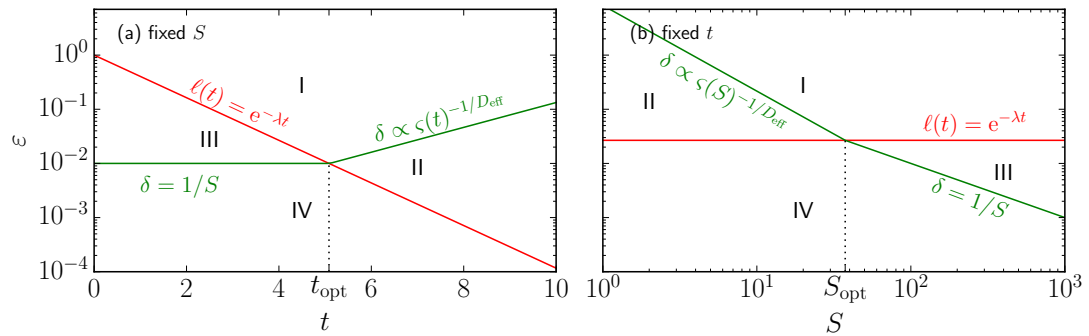

FIGURE 4.3: Schematic picture of the behaviour of the transition points δ and ℓ. The (green) δ-line separates the box-sizes where we observe the actual dimension of the set, i.e. $D_{\text{obs}} = D_{\varsigma \to \infty}$ from box-sizes where $D_{\text{obs}} = 0$. The red ℓ line (4.5) on the other hand separates box-sizes with $D_{\varsigma \to \infty} = 1$ from box-sizes with $D_{\varsigma \to \infty} = D_{\text{eff}}$. The point of intersection between the two lines is called t_{opt} (or S_{opt}). (a) at a fixed sample size S; (b) at a fixed time t. Note the different scaling of the x-axes. The roman numerals mark regions of similar combinations $(D_{\text{obs}}(\varepsilon, \varsigma), D_{\varsigma \to \infty}(\varepsilon))$.

algorithm. Starting from the left ($\varepsilon \to 0$) we start in the regime of saturation due to Eq. (4.7) where $n_{\text{filled}} = \varsigma$. With increasing ε we then pass the transition $D_{\text{obs}} = 0$ to $D_{\text{obs}} = 1$ (see Eq. (4.8)) at $\varepsilon = 1/S$ and lastly we cross over to $D_{\text{obs}} = D_{\text{eff}}$ at $\varepsilon = \ell$ (see Eq. (4.5)). In the sketched scenario ς is large enough to observe the line-like nature of $\mathcal{S}_t$. This means, that here $\delta < \ell$ and therefore $\delta = 1/S$, i.e. case (i). If on the other hand ς is small – or, equivalently, t is large – eventually, $\delta > \ell$ change order and we observe case (ii). In this case the observed dimension would transition directly between $D_{\text{obs}} = 0$ at small boxes to $D_{\text{obs}} = D_{\text{eff}}$ at large ε without crossing the $D_{\text{obs}} = 1$ region.

Now that we have established the types of behaviour that we can observe we discuss in more detail the circumstances under which they arise. In Fig. 4.3 we combine the scalings from Eqs. (4.4) and (4.10). The (ε, t) and (ε, S) spaces are each split in four regions which we denote by I to IV and which are uniquely characterised by the combination of $D_{\varsigma \to \infty}$ and D_{obs} that is observed in a box-counting procedure using ε, t and S from that region. The value combination for all four regions can be found in

TABLE 4.1: Values of the observed dimension and of the real dimension in the four regions of Fig. 4.3

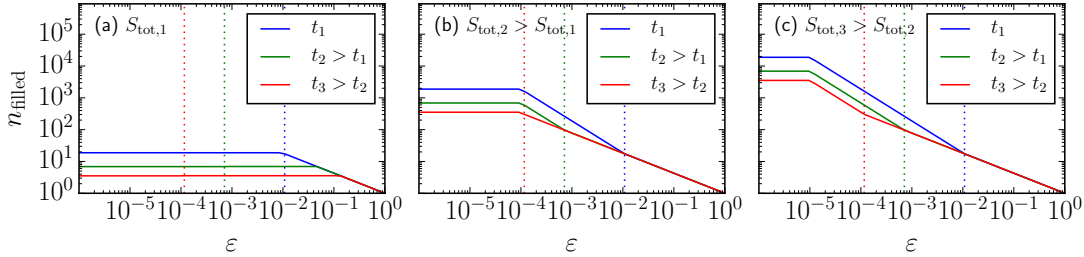|	$D_{\varsigma \to \infty}(\varepsilon)$	$D_{\mathrm{obs}}(\varepsilon, \varsigma)$
I	D_{eff}	D_{eff}
II	D_{eff}	0
III	1	1
IV	1	0

FIGURE 4.4: Sketches of the typical behaviour of the number of found boxes $n_{\mathrm{filled}}(\varepsilon)$ (solid lines) when box-counting $\mathcal{S}_t$ at different values of $t \in \{t_1, t_2, t_3\}$ and different numbers of samples $S \in \{S_{\mathrm{tot},1}, S_{\mathrm{tot},2}, S_{\mathrm{tot},3}\}$. The dashed lines mark the position of $\ell(t)$.

Tab. 4.1. To clarify the meaning of these regions we now take a look at a couple of examples. Let us start by conjuring up Fig. 4.2. This figure represents a vertical slice along a line of fixed box-sizes in Fig. 4.3. More precisely, it is a slice that crosses from region IV to III to I. In a scenario where the sample size is fixed (Fig. 4.3(a)) this vertical slice is left of $t_{\mathrm{opt}}(S)$. If we assume that we are studying $\mathcal{S}_t$ with t fixed (Fig. 4.3(b)) the vertical slice would lie right of S_{opt}. We will explain the relevance of the intersection points after some more examples which are shown in Fig. 4.4. In Fig. 4.4(a) the sample size is very small and therefore for most of the box-sizes $D_{\mathrm{obs}}(\varepsilon, \varsigma) = 0$ for all shown values of t. This corresponds to a slice IV-II-I. For the (S, t) combinations shown here $\delta > \ell$ so that we do not see the transition at ℓ. In Fig. 4.4(b) the sample size is large enough that we observe the D_{eff} over the full range of possible ε values at all three t_i. Here, the value of t_3 (S_2) is very close to t_{opt} (S_{opt}) so that in this example the curves for t_1 and t_2 follow a line across IV-III-I while the t_3-curve almost does not cut region III but goes directly from IV to I. Fig. 4.4(c) shows the case of very large S where all three curves follow a line IV-III-I.

Let us now look at the regions from Tab. 4.1 from the point of view of someone who wants to find efficient parameters for a numerical box-counting algorithm to calculate the real dimension $D_{\varsigma \to \infty}(\varepsilon)$ of $\mathcal{S}_t$ of a given 1D-map. There is a computational cost attached to each box-size and to each iteration step that is calculated. Since sampling in this system means to iterate a randomly picked initial condition up to an exit or up to t, depending on what happens first, the cost of increasing S also grows with t. Basically there are two typical scenarios:

(i) We have a sampled version of $\mathcal{S}_t$ with fixed (S, t) and we want to know which box-sizes ε we can trust to give us a meaningful result, i.e., $D_{\mathrm{eff}}(\varepsilon)$.

(ii) We can sample $\mathcal{S}_t$ on the fly and have some freedom in the choice of S and t, and we want to know a choice of (S, t) that leads to $D_{\mathrm{eff}}(\varepsilon)$ over a particular range of box-sizes.

The scenarios correspond to the questions

(i) *"What is the optimal range of box-sizes?"* and

(ii) *"How many samples do I need?"*

stated in the introduction of this chapter and we can now answer them using Eqs. (4.4), (4.5), (4.8), and (4.10): (i) As long as $\varepsilon > \delta$ we observe the dimension of the set, while for $\varepsilon < \delta$ we resolve the individual data points and therefore $D_{\mathrm{obs}} = 0$. How sharply this transition is depends on the choice of (S, t). (ii) The answer here depends slightly on the definition of "meaningful", but since the value of the dimension for $\varepsilon < \ell$ and $\varepsilon < \delta$ is trivial, the only dimension worth calculating numerically is D_{eff} (i.e., the algorithm should stay in region I). The optimal choice of t or sample size S then is the one where the range of ε's leading to D_{eff} is maximal. This happens at the intersection points

$$t_{\mathrm{opt}}(S) = \frac{1}{\lambda} \ln S \tag{4.11}$$

and

$$S_{\mathrm{opt}}(t) = \mathrm{e}^{\lambda t}. \tag{4.12}$$

These equations can be obtained by simply solving $\ell(t) = \delta(S, t)$ (see Fig. 4.3) for S or t. With that the proportionality constant in Eq. (4.9) can be expressed as a function of S, the constant ℓ_0 in

$$\ell(t) = \ell_0 \exp(\lambda t), \tag{4.13}$$

the Lyapunov-exponent λ, and the escape rate κ by solving $\ell(t_{\mathrm{opt}}) = C\varsigma(t_{\mathrm{opt}})^{-1/D_{\mathrm{eff}}}$ for C which leads to

$$\delta(t > t_{\mathrm{opt}}) = \ell_0 S^{-1 - \frac{\kappa}{\lambda D_{\mathrm{eff}}}} \exp(-\frac{\kappa}{D_{\mathrm{eff}}} t), \tag{4.14}$$

where we assume that we are already at t-values in the asymptotic regime (4.4).

S_{opt} and t_{opt} each have a very intuitive interpretation. In the case that we have an algorithm that allows us to study a given range of ε's (limited e.g. by machine precision). If we iterate S initial conditions in the system up to a time $t < t_{\mathrm{opt}}$ then we do not make use of the possible resolution of the algorithm by providing it a set with lower resolution.

On the other hand if we iterate to $t > t_{\text{opt}}$ we waste computational power to calculate an object that has a lower resolution than the algorithm. Analogously, if at fixed t we chose $S < S_{\text{opt}}$ then we expect gaps in our approximation of $\mathcal{S}_t$ that are similar in size to the box-sizes used by the algorithm and we waste computational power on these box-sizes. And lastly, if $S > S_{\text{opt}}$ then we oversample the set and create an approximation of $\mathcal{S}_t$ with a finer resolution than the algorithm can pick up. These limitations are valid for all the common algorithms discussed in Sec. 3.2. That means that the scalings of S_{opt} and t_{opt} are very hard to circumvent computationally without resorting to previous knowledge of the system under consideration. Accordingly, the different algorithms – at least in terms of sampling efficiency – are expected vary only by pre factors in efficiency as already hinted at in Sec. 3.2.3. We expect our results to be very useful in choosing the parameters connected to the relevant length scales efficiently.

So far we have stated the challenges that arise in typical numerical dimension calculations and we have formulated a general theory of the scaling of the length scales ℓ and δ which define D_{eff} in terms of S and t. In the upcoming sections we apply this theory to relevant strongly chaotic systems, and confirm the predictions made above numerically, and, in case of the tent map, also analytically.

4.2   Application to the Analytically Solvable Open Tent Map

In the following we discuss the general concepts presented in Sec. 4.1 on the instructive example of the open tent map. This system is simple enough that we can make analytical calculations but at the same time shows many of the features that also appear in more physical examples of open chaotic systems.

The open tent map is defined as follows:

$$x_{n+1} = \begin{cases} \frac{\beta x_n}{2a} & \text{for} \quad x_n < a \\ \frac{\beta(1-x_n)}{2(1-a)} & \text{for} \quad x_n \geq a \\ \text{escape} & \text{for} \quad x_n \geq 1 \,, \end{cases} \tag{4.15}$$

$$t_{n+1} = \begin{cases} t_n + 1 & \text{for} \quad x_n < 1 \\ t_n & \text{for} \quad x_n \geq 1 \end{cases}$$

where $a \in (0,1)$ and $\beta \geq 2$. The mapping is illustrated in Fig. 4.5. In this system a trajectory is escaping if it leaves the interval $[0,1)$ so that we effectively have a hole of size
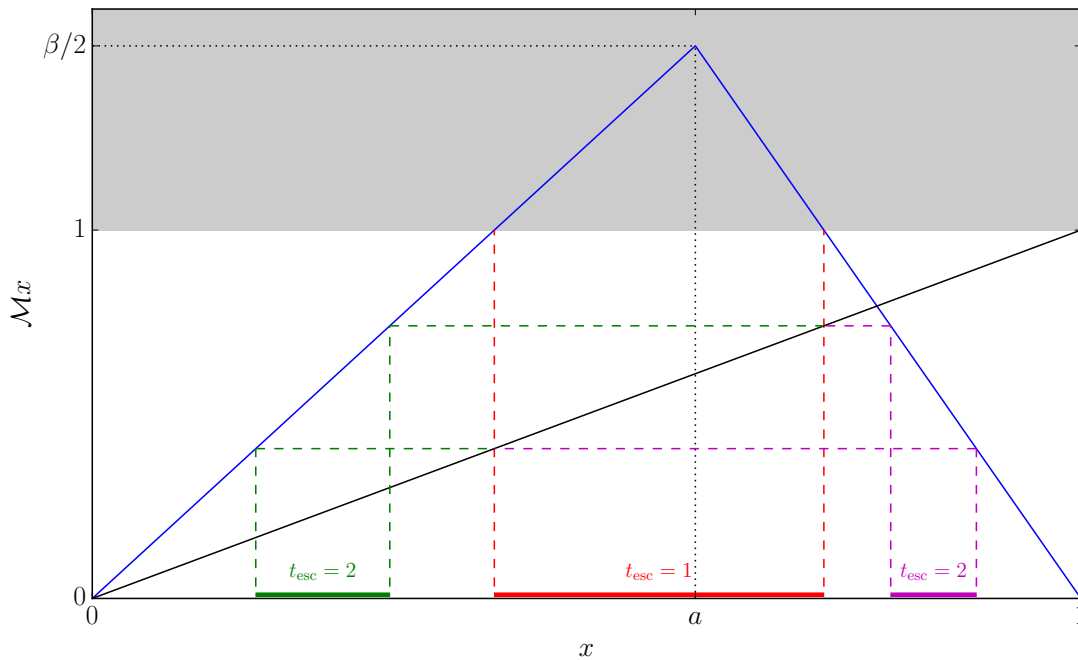
FIGURE 4.5: The open asymmetric tent map as defined in Eq. (4.15). Trajectories escape the system when they are mapped outside the interval $[0, 1)$ (grey area). The red line marks the first pre-image of the hole and the green and magenta lines mark the second pre-images.
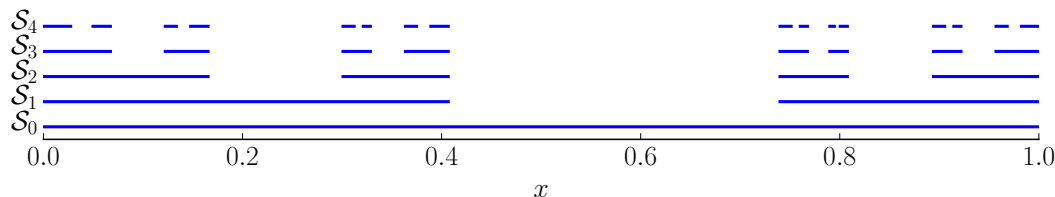

FIGURE 4.6: Surviving sets $\mathcal{S}_t$ in the asymmetric tent map (4.15) with $\beta = 3$ and $a = 0.61$.

$1 - \beta/2$ (if $\beta < 2$ the system is closed). In a map like this the escape time is the number of iterations until escape and thus $t_{esc} \in \mathbb{N}$ plays the role of t in the previous section. In Fig. 4.5 we also mark the intervals of initial conditions with $t_{esc} = 1, 2$, which are the first and second pre images of the hole. The next set of pre images would fall in the empty regions between the colored segments and so on, so that the time-t trapped set $\mathcal{S}_t$ (2.16) in this system is cantor-like. In Fig. 4.6 we clearly see that $\mathcal{S}_t$ approaches a Cantor-set like structure. In fact, the tent map with $a = 1/2$, $\beta = 3$ generates the middle third Cantor set for $t \to \infty$. Fig. 4.7 shows the escape-time distribution along the unit interval of an asymmetric tent map with $\beta = 3$ which corresponds to a hole-size of $1/3$. If we compare the zoomed image in Fig. 4.7(b) with the original we can easily see the fractality of the escape time distribution. We can also see that the pre-images of the hole do not overlap and therefore the measure of $\mathcal{S}_t$ is exactly $\mu_L (\mathcal{S}_t) = (1 - \mu_L(H))^t = (2/\beta)^t$.
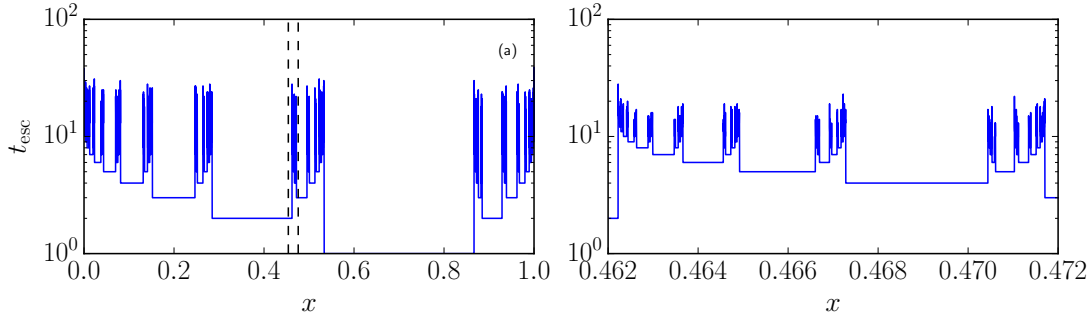
FIGURE 4.7: Escape times of 10^6 evenly spaced initial conditions $x \in (0,1)$ in an open asymmetric tent map (4.15) with $a = 0.8$ and $\beta = 3$. (a) Full phase space (b) Zoom of the region between the dashed lines.

This means that the escape rate κ (4.3) in this system is $\kappa = -\ln(2/\beta)$ and therefore the large-S-asymptotic behavior of the number of successful samples (4.6) is

$$\varsigma = S e^{\ln(2/\beta)t} \tag{4.16}$$

In the tent map we can calculate the distribution of segment sizes $\ell_i(t)$ analytically. We describe the segment sizes at any cut-off time t as being generated by a multiplicative process with two different scales. In the tent map we have two possible absolute values of the local derivative: $\mathcal{M}'_l := \frac{\beta}{2a}$ and $\mathcal{M}'_r := \frac{\beta}{2(1-a)}$. To get from t to $t+1$ a fraction a of each segment is multiplied by $\mathcal{M}'_l$ while the rest is shrunk by the factor $\mathcal{M}'_r$. Therefore the segment sizes follow a binomial distribution. This allows us to quantify the value of the typical length $\ell(t)$ in (4.5). The minimum and maximum segment width after t iterations are $l_{\min,t} = \min(a, 1-a)^t \left(\frac{2}{\beta}\right)^t$ and $l_{\max,t} = \max(a, 1-a)^t \left(\frac{2}{\beta}\right)^t$, respectively. The width of the distribution depends on a and it goes to zero in the case $a = 1/2$. Accordingly, the expected value of the segment size for large t is

$$\mathbb{E}(l_t) = \left(\frac{2}{\beta}\right)^t a^{at}(1-a)^{(1-a)t}. \tag{4.17}$$

We now show that this is equivalent to Eq. (4.4) by calculating the Lyapunov exponent

$$\lambda(x_0) = \lim_{t \to \infty} \frac{1}{t} \ln \left| \frac{\mathrm{d}\mathcal{M}^t(x_0)}{\mathrm{d}x} \right|, \tag{4.18}$$

of the tent map, where $\frac{\mathrm{d}\mathcal{M}^t(x_0)}{\mathrm{d}x} = \prod_{i=1}^{t} \frac{\mathrm{d}\mathcal{M}(x_{t-i})}{\mathrm{d}x}$. To do so we can use the ergodicity of the dynamics and replace the averaging over a trajectory by an average over the invariant set. We first consider a finite time t and then look at $t \to \infty$. After t iteration the fraction of the unit interval that has $|\mathcal{M}'(x)| = \mathcal{M}'_l$, or $|\mathcal{M}'(x)| = \mathcal{M}'_r$, is equal to $a(1 - \beta/2)^n$, or $(1 - a)(1 - \beta/2)^n$, respectively. Now all that is left to do is normalise
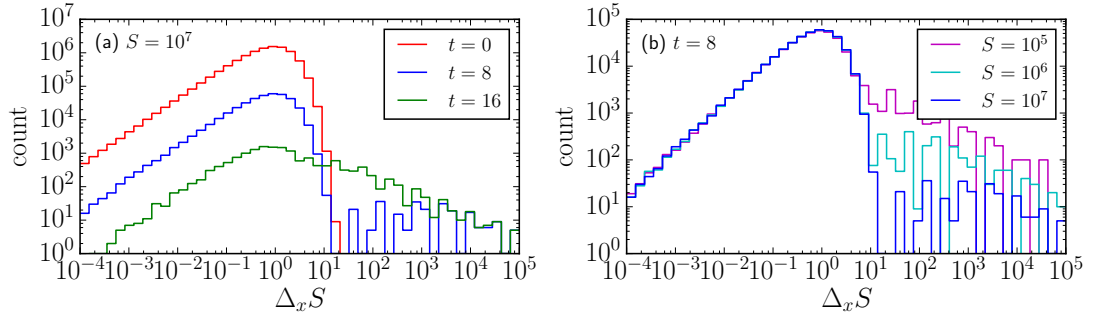
FIGURE 4.8: Time and sample-size dependence of the histograms of the spacing between neighbouring samples calculated in a tent map wit $a = 0.8$, $\beta = 3$. (a) fixed overall sample size $S = 10^6$. (b) fixed time $t = 4$ but different values of S. For each value of S in (a) and (b) we use $10^7/S$ realisations of the sampling and the distances $\Delta_{x,i} := |x_i - x_{i-1}|$ are normalised by $1/S$.

these values by $\mu_{\mathrm{L}}(\mathcal{S}_t)$ and we can write (4.18) as

$$\lambda_{\mathrm{tent}} = \lim_{t \to \infty} \frac{1}{t} \ln \left(\mathcal{M}_l'^{at} \mathcal{M}_r'^{(1-a)t} \right) = a \ln \frac{\beta}{2a} + (1-a) \ln \frac{\beta}{2(1-a)}. \tag{4.19}$$

By rearranging this expression to $\lambda_{\mathrm{tent}} = \ln \frac{\beta}{2} - a \ln a - (1-a) \ln(1-a)$ and comparing with (4.17) we confirm the agreement with Eq. (4.4). Thus in the open tent map the analytic prediction of the transition between $D_{\varepsilon \to 0}$ and D_{eff} (see Eq. (4.5)) is

$$\ell(t) = \left(\frac{2}{\beta} \right)^t a^{at} (1-a)^{(1-a)t}. \tag{4.20}$$

We can use the fact that we know the distribution of segment size in this example to discuss the transition due to a lack of successful samples at $\varepsilon \approx \delta$ in more detail. In Fig. 4.8 we show numerically that (as predicted in Eq. (4.10)) the typical distance between neighbouring samples on the set is $\delta = 1/S$ for small t. We also see a heavy tail growing on the right side of this value as t increases. These larger intervals are the gaps in $\mathcal{S}_t$ so they are distributed according to D_{eff}. We can observe in Fig. 4.8(a) how for large t these intervals interfere with the distribution of the Δ_x caused by the sampling. At $t = 8$ the distributions start to overlap and at $t = 16$ the two distributions are no longer distinguishable. What we observe here is the change in the order of ℓ and δ with increasing iteration-number. In Fig. 4.8(b) we can see how the overlap of the two parts of the distribution decreases with increasing sample-size.

In Fig. 4.9 we show results obtained by numerical box-counting in an open tent map. The shapes of the n_{filled}-curves share their central features with the stylised curves presented in Fig. 4.4. First of all, at small ε the curves get flat (i.e. $D_{\mathrm{obs}} = 0$) because they reach the upper limit (4.7). For $t = 8$ and $t = 12$ this transition occurs at $\delta = 1/S$
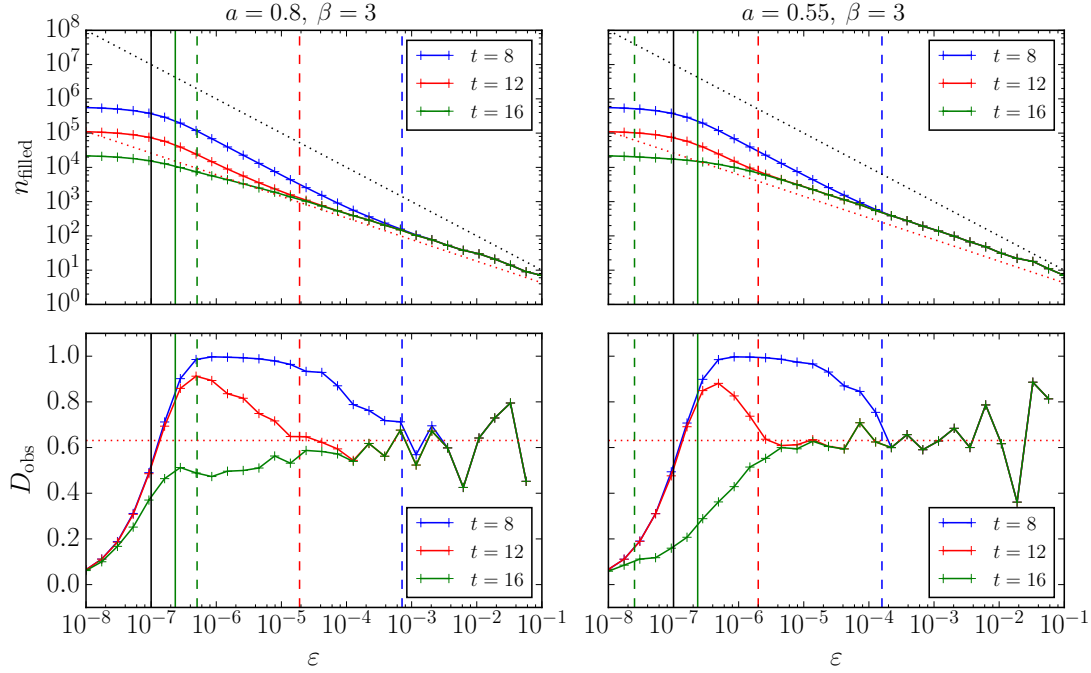
FIGURE 4.9: Numerical results from box-counting at different cut-off times t in the tent-map with different asymmetry parameters a but constant $\beta = 3$; The sampling was uniform over $[0, 1)$ with a sample size of $S = 10^7$. The dotted lines are $D_0 = 1$ (black) and $D_0 = \ln(2)/\ln(3)$ (red). The dashed vertical lines mark $\ell(t)$ (for $\varepsilon > \ell(t)$, $D_{\text{obs}} = D_{\text{eff}}$). The vertical black line is at $\varepsilon = 1/S$ and the green vertical lines mark $\varsigma^{-1/D_{\text{eff}}}$ (cf. Eq. (4.10)).

and we can see in the local dimension curves that the quickest change does indeed happen very close to this predicted value. We can also observe the second kind of transition at δ close to ℓ in the curves for $t = 16$ where the dimension changes directly from D_{eff} to 0.

Now let us compare this observations to the curves in Fig. 4.8. The parameters used in the generation of the histograms are the same as the parameters in the left column of this figure.

- At $t = 8$ we observe a dimension of one for $\varepsilon \in [10^{-6}, 10^{-5}]$ which in the rescaled coordinates of Fig. 4.8 corresponds to an interval $\Delta_x S \in [10^1, 10^2]$. In this interval, the gap between the two distance distributions is so that at box-sizes of this order an algorithm resolves neither the gaps created by the sampling nor the gaps that are intrinsic to the fractal set.

- At $t = 16$ in the asymmetric case we can see that ℓ is very close to $1/S$ so here we see a competition between the two possible values of δ as seen in Eq. (4.10).

Next, we look at the transition to D_{eff} at $\varepsilon = \ell$:

- For $t = 8$ and $t = 12$ the onset of his transition coincides very well with the analytical value. By comparing the symmetric and the asymmetric case we can also verify, that the transition becomes sharper for the symmetric case because the distribution of lengths is narrower there.

- The $t = 16$ case is again special. In the asymmetric case we can observe how the increase in n_{filled} because of $\varepsilon < \ell$ is competing with the decrease caused by $\varepsilon \approx \delta$. In the more symmetric map ℓ is already smaller than $1/S$ and we can observe a drop of D_{obs} that is indeed most severe close to $\delta \propto \varsigma^{-1/D_{\text{eff}}}$ (cf. Eq. (4.10)).

To discuss the relevance of the analytical predictions to numerical methods we calculated the scaling of ℓ, δ and t_{opt} with t and S numerically. In simple terms we propose a numerical procedure consisting of the following three steps for many combinations (S, t):

1. Calculate D_{obs} for a range of box-sizes,

2. find the transitions at $\varepsilon = \delta$ and $\varepsilon = \ell$, and lastly,

3. use this information to find scaling of t_{opt} with S.

Each of the steps can be done in different ways. For example for step 1 alone there exist numerous algorithms that produce the desired results more or less efficiently (see Sec. 3.2 for an overview). We chose the following approach and parameters (see Appendix B for a detailed description):

1. From n realisations of S initial conditions randomly drawn from a uniform distribution over $[0, 1)$ calculate n approximations $\tilde{\mathcal{S}}_t$ of $\mathcal{S}_t$ for different values of t, and repeat the process with different choices of S. For every approximation then use a box-counting algorithm to calculate the number of boxes containing any of its elements and use the local derivative between two adjacent box sizes as $D_{\text{obs}}(\varepsilon)$.

2. Repeat the following steps for all sets $\tilde{\mathcal{S}}_t$ to get n estimations of ℓ and δ for every value of t:

   a) Estimate δ as the ε in the transition region between $D_{\text{obs}} = 0$ and $D_{\text{obs}} = D_{\varsigma \to \infty}$ where the slope of $D_{\text{obs}}(\varepsilon)$ is maximal.

   b) Estimate ℓ as the maximum box-size where the dimension curve for a given t is significantly different from the curves for $t' > t$. It is not possible to find ℓ with this method if $\ell < \delta$, and in this case this approach returns a value close to δ.
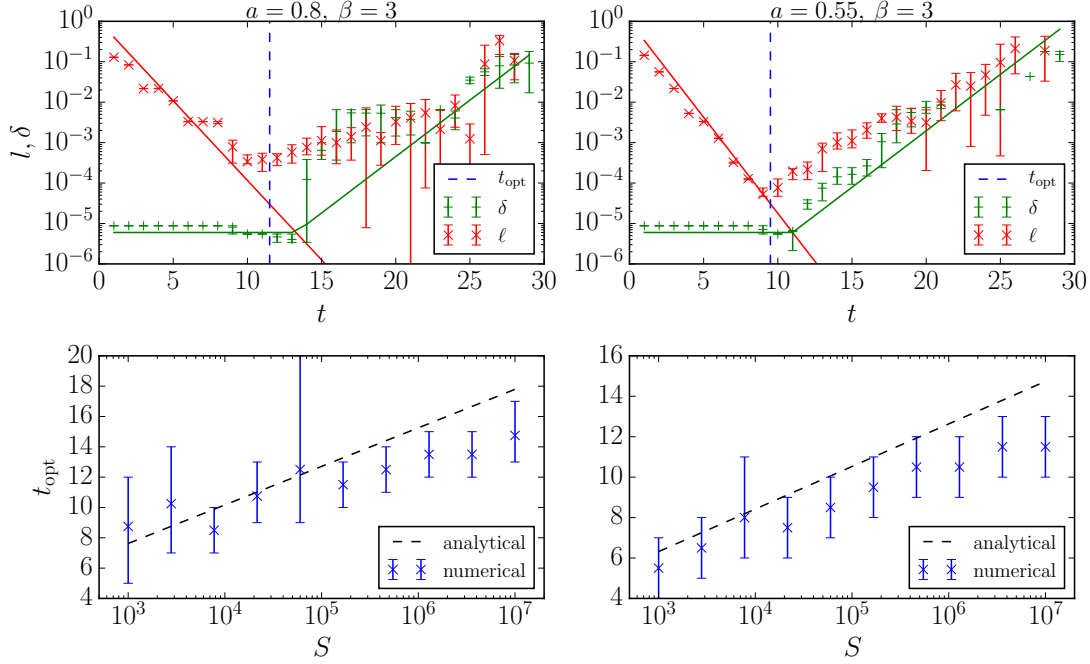
FIGURE 4.10: Numerical results of ℓ, δ and $t_{\text{opt}}(S)$ in the tent map with high (left column) and low (right) values of the asymmetry parameter a. The solid lines in the top row are the analytical predictions. The sample size used in the top row is $S \approx 1.7 \times 10^5$. For ℓ, δ we plot the average over the n realisations of the Sampling together with error bars that span the interval from the 10th to the 90th percentile of the n values obtained for every (S,t)-combination. In the $t_{\text{opt}}(S)$ plots we show the average over the locations of the 4 lowest $\langle\ell\rangle$-values and the error bars cover the whole range of their locations.

3. Estimate $t_{\text{opt}}(S)$ as the average over the four smallest values of $\langle\ell\rangle_n(t)$, where $\langle\ldots\rangle_n$ is the average taken over the n realisations of the sampling.

In Fig. 4.10 we show the results of this numerical approach. We now discuss them using the representative example of the results obtained with $S \approx 1.7 \times 10^5$ presented in the top row of the figure quantity by quantity. We use the superscript $^{\text{A}}$ to denote the analytically estimated values. (see Equations (4.4), (4.10), (4.14), (4.11), and (4.19)).

- As long as $\delta^{\text{A}} = 1/S$ and t is small the numerical results follow the analytic prediction very well.

- Once we leave this regime (i.e. if $t \gtrsim 13$ for $a = 0.8$ and $t \gtrsim 11$ for $a = 0.55$) the behaviour changes and we observe a strong discrepancy between δ^{A} and δ in the strongly asymmetric case. The reason for the difference lies in the asymmetry of the distribution of segment sizes. At $t = 15$ for example the largest segment size in the strongly asymmetric map is of the order of 10^{-4}. The smallest segment on the other hand is already of the order of 10^{-14} which is much smaller than $1/S \approx 5.9 \times 10^{-6}$. The fact that there are many segments too small to be sampled

at this value of S leads to much larger effective gaps in the set than we assumed in the discussion leading to Eq. (4.10). The fact that in the more symmetric case this discrepancy is not observed further corroborates this hypothesis. Also, δ^{A} and δ seemingly coincide more for larger t at $a = 0.8$. The reason for this is most likely also the shape of the segment size distribution which gives a lot of weight to the extreme segment sizes at smaller t but not at higher values.

- Regarding the algorithm to find ℓ we can state, the most obvious observation is that – as already discussed earlier – we cannot numerically observe the typical length of the segments once $\ell^{\mathrm{A}} < \delta^{\mathrm{A}}$ but instead for larger t we resolve the largest time-dependent feature which is close to δ. The reason for the shift towards larger values obtained with the algorithm for δ lies in the fact that the ℓ-algorithm finds the onset of the transition while the δ-algorithm looks for the steepest slope.

- On the other hand in the range where $\ell > \delta$ (i.e. for small t) the numerical results confirm ℓ^{A} very well.

- Because of the width of the segment size distribution the analytical prediction $t_{\mathrm{opt}}^{\mathrm{A}}$ lies above the numerically observed point. If we look at other values of S (bottom row of plots) we can see that nonetheless the scaling of t_{opt} with S follows the analytical estimation.

To summarize the observations from a numerical perspective: The relatively simple proposed algorithm already allows to find the optimal value of t at a given sample size S. One possible approach for that would be to, starting from a small t_0, continue to larger values of t until the slope of $\ell(t)$ becomes positive. Of course any other numerical method to find the minimum can be employed here. If the Lyapunov exponent is known $t_{\mathrm{opt}}^{\mathrm{A}}$ can be used to chose t instead of using this method. In that case the minimum suitable box-size ℓ still has to be found numerically as ℓ^{A} is not usable in this region. If $t_{\mathrm{opt}}^{\mathrm{A}}$ is used the range of box-sizes is smaller than in the optimal case, but the computational cost saved by not having to box-count at many values of t can be used for example to increase S which in turn would increase the range of box-sizes.

In conclusion, the tent map allows us to verify our general statements from 4.1 by comparing analytic results with numerical calculations. In the following section we go on to show that the same kind of behaviour can also be observed in more complex systems like the stadium billiard.
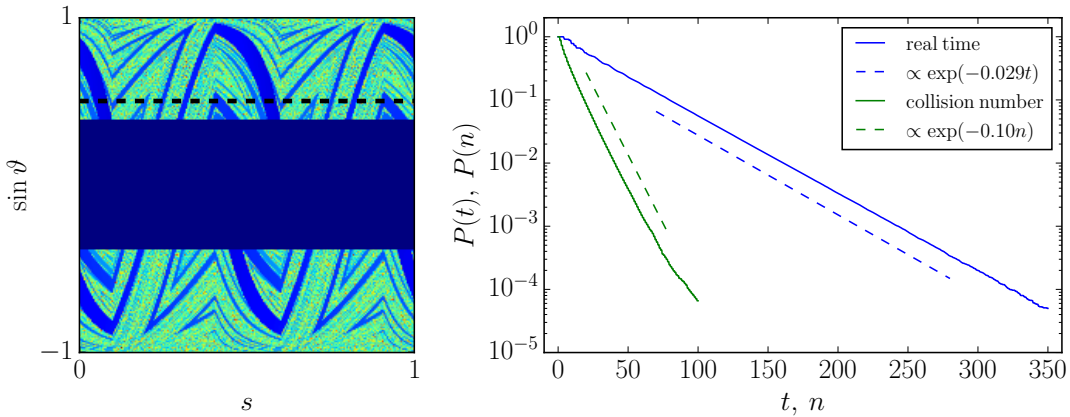
FIGURE 4.11: (left) Escape time distribution over the full phase space in an open stadium billiard. Dark blue marks $t_{\mathrm{esc}} = 0$, i.e. the hole, the color changes gradually from blue to green, then yellow and finally red with increasing escape time. (right) Survival probabilities in real- and discrete time in the same systems. The parameters here are $r = 2$, $L = 4$, and $\{s_{\min}, s_{\max}, \vartheta_{\min}, \vartheta_{\max}\} = 0, 1, -\pi/8, \pi/8$. The exponents of the dashed lines are obtained from fitting exponential functions to the central 60% of each data set.

4.3 Numerical Observations in Fully Hyperbolic Stadium Billiard

In Sec. 4.2 we have shown to which extent we can observe the general predictions made in Sec. 4.1 in simple chaotic maps. In this section we show that they also hold in more complicated but also more physically relevant systems, like the stadium billiard which we have introduced in Secs. 2.2 and 2.4.

In Fig. 4.11 we show the escape time distribution $t_{\mathrm{esc}}(s_0, \sin\vartheta_0)$ and the survival probability in an example. In this particular billiard the complete boundary is fully absorbing at collisions with $|\vartheta| < \pi/8$. This choice of opening removes all the marginally unstable periodic orbits from the system, so that the survival probability is purely exponential. Fig. 4.11 shows that the numerically estimated survival probability in these particular billiard is indeed exponential and that the exponent is different for $P(t) \propto \exp(-\kappa_t t)$ and $P(n) \propto \exp(-\kappa_n n)$. We can use the fitting results to estimate the typical inter-collision distance $\tau := \lim_{n\to\infty} t_n/n$ of a surviving trajectory where t_n is the length of the trajectory after n iterations as $\tau \approx \kappa_n/\kappa_t \approx 3.45$. This is significantly smaller than the typical estimation for mean free path in a closed billiard $\langle l \rangle = \pi A/P \approx 4.36$ [LS90, MLS93] where A is the area and P is the perimeter of the billiard because our choice of hole removes the longest possible paths, i.e., end-to-end collisions with small reflection angles. An analogous estimation of the mean free path in open systems can be achieved by taking the average $\langle l \rangle_{\mathrm{c}}$ according to the unstable manifold as described in [APT13b]. In Fig. 4.12 we can see the difference between
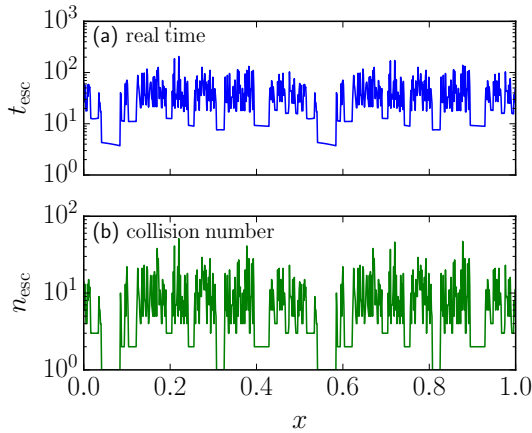
FIGURE 4.12: (a) Real time (trajectory length) and (b) number of iterations until a trajectory hits the hole in the stadium billiard. Initial conditions were chosen along the dashed black line in Fig. 4.11
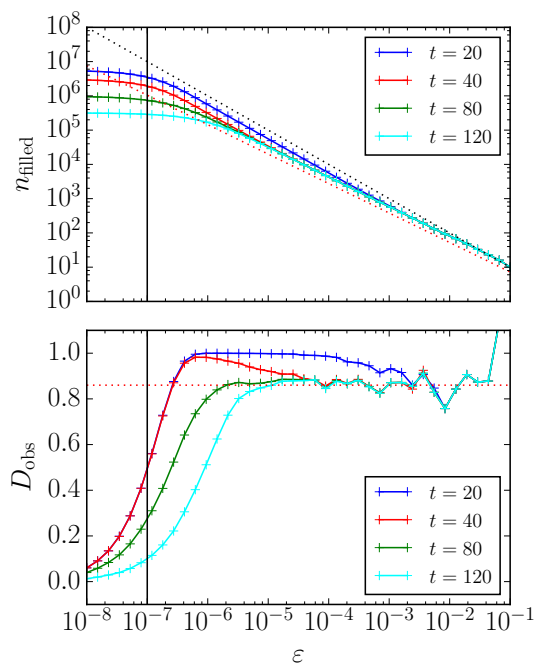

FIGURE 4.13: Number of filled boxes and local dimension in the stadium billiard with four different choices of the cut-off time t. S initial conditions were placed randomly along the line with $\sin \vartheta_0 = 0.5$ and $s_0 \in [0, 1)$. The black vertical line marks the point where $\varepsilon = 1/S$; the dotted black line in the top plot is for comparison and it scales as $1/\varepsilon$. The dotted red lines show the behaviour for $D_{\mathrm{eff}} = 0.86$, the value obtained by averaging D_{obs} over $\varepsilon > \max\{\ell, \delta\}$.

the iteration number and the real time in the escape time distribution of the stadium. Unsurprisingly, the transitions between intervals of different iteration numbers match the transitions between different escape times, but we can observe how considering the trajectory length introduces some noise on the distribution of segment lengths. That means, at the transition between two integer escape times, the length of the segments takes a little while to settle to a constant value. In Fig. 4.13 we show the numerically calculated local observed dimensions of a slice across $\mathcal{S}_t$ in the billiard. We chose initial conditions along a line, so that our observed dimension is the dimension of this slice and it falls in the interval $[0, 1]$. The fractal dimension of the full surviving set $\mathcal{S}_t$ can be obtained from that value by adding 1 to this dimension [Ott02]. As in the simple map discussed in Sec. 4.2 we can identify three regions of observed scaling. Going from small to large box sizes we first see $D_{\mathrm{obs}} = 0$ then the transition to $D_{\mathrm{eff}} \approx 0.86$. For $t = 40$ we

FIGURE 4.14: Numerical results of ℓ, δ and $t_{\mathrm{opt}}(S)$ in the stadium billiard. The sample size used in the top row is $S \approx 4.6 \times 10^5$. For ℓ, δ we plot the average over the n realisations of the Sampling together with error bars that span the interval from the 10th to the 90th percentile of the n values obtained for every (S, t)-combination. The solid red and green line show the scaling obtained by fitting an exponential function to the respective region. In the $t_{\mathrm{opt}}(S)$ plots we show the average over the locations of the 4 lowest $\langle \ell \rangle$-values and the error bars cover the whole range of their locations. The purple crosses are the lowest t with $\langle \delta \rangle(t) > 2/S$. The black lines in the bottom plot show $\ln(S)/\lambda$ with the λ value from the fit in the top plot (dashed) and the theoretical value (dotted).
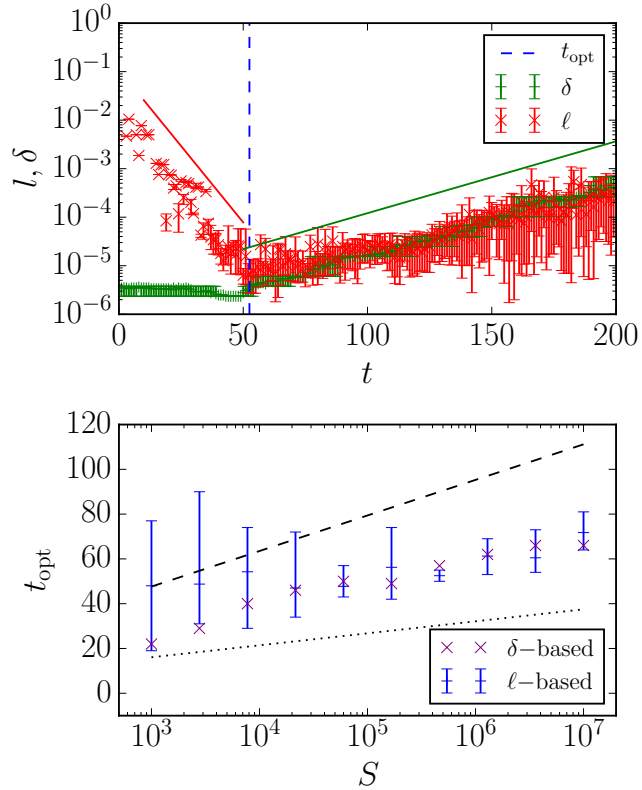
can also observe an ε-region with $D_{\mathrm{obs}} = 1$. In summary, we can numerically observe the basic predictions from Sec. 4.1 in this more realistic continuous-time system.

But not only do the transitions at ℓ and δ as defined in Eqs. (4.5) and (4.8), respectively, occur in this system, we can also numerically show that they follow the same scaling behaviour as in the simple map. In Fig. 4.14 we can see that where we can observe ℓ numerically, i.e., for times t where $\ell > \delta$, it scales exponentially. By fitting an exponential to the data at $S = 10^7$ (where the relevant interval is largest) in this region we obtain a value of $\lambda \approx 0.15$ which is lower than the analytical value of $\lambda_{\mathrm{closed}} \approx 0.43$ obtained for the closed system [BS78]. That the values are different comes as no surprise, since $\lambda_{\mathrm{closed}}$ is calculated in the closed system. We use the numerical results from the ℓ-algorithm to calculate t_{opt} as described in the previous section. As in the asymmetric tent map in Fig. 4.10 the value is systematically lower than the prediction of $t_{\mathrm{opt}} = \ln(S)/\lambda$ with the numerically obtained value $\lambda \approx 0.15$, but nonetheless, the logarithmic scaling with S is confirmed. We have compared the values of t_{opt} with numerical values compared with an alternative algorithm. Namely, we used the results from the algorithm for δ and estimated t_{opt} as the lowest t with $\langle \delta \rangle(t) > 2/S$, $\langle \delta \rangle$ is computed over all n realisations for each S. Both methods agree reasonably well and the observed scaling follows $t_{\mathrm{opt}} = \ln(S)/a$ with $\lambda_{\mathrm{num.}} < a < \lambda_{\mathrm{closed}}$. The numerical δ-curve, however, shows excellent agreement with our general predictions. For small t,
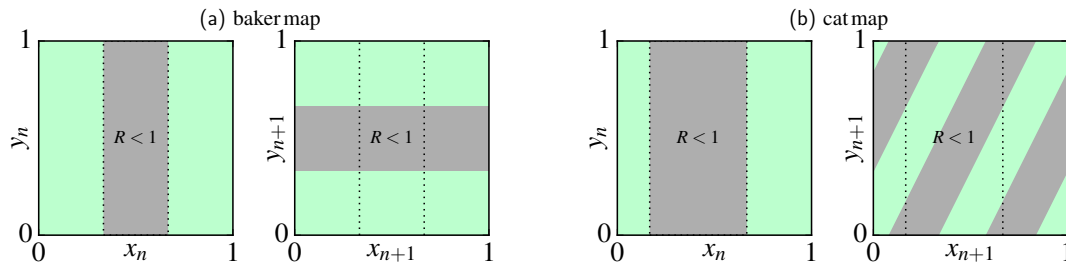
FIGURE 4.15: Sketches of one iteration of partially open versions of (a) the baker map (4.21) and (b) the cat map (4.22). The region between the dashed lines is the absorber (or hole) and it has a reflectivity $R < 1$. The grey regions in the phase-space pictures are there to show where the hole is mapped in one iteration.

$\delta \approx 1/S$ and then it follows an exponential scaling with an exponent $\kappa/D_{\text{eff}} \approx 3.41 \times 10^{-2}$ obtained by fitting an exponential to the relevant range of data. Using $D_{\text{eff}} \approx 0.86$ (see Fig. 4.13 we obtain $\kappa \approx 2.93 \times 10^{-2}$ which is very close to the value $\kappa \approx 2.9 \times 10^{-2}$ obtained by fitting an exponential to $P(t)$ (see Fig. 4.11).

To summarize: the general predictions from Sec. 4.1 can be observed in a much more realistic system such as the stadium. We can also use the theory to numerically find the optimal ε range to observe D_{eff}.

4.4   Maps with Non-Trivial Rényi Dimension Spectrum

As a last class of systems to discuss the general statements from Sec. 4.1 we now consider partially open systems with multifractal asymptotic measures. As representative cases of fully chaotic area-preserving maps we investigate in detail the baker [Ott02] map defined as

$$
\begin{aligned}
x_{n+1} &= 3x_n - \lfloor 3x_n \rfloor \\
y_{n+1} &= y_n/3 + \lfloor 3x_n \rfloor/3 \\
t_{n+1} &= t_n + 1 \\
I_{n+1} &= I_n R(x_n, y_n)
\end{aligned}
, \tag{4.21}
$$

and the cat map [dMdA95]:

$$
\begin{aligned}
x_{n+1} &= 2x_n + y_n \mod 1 \\
y_{n+1} &= 3x_n + 2y_n \mod 1 \\
t_{n+1} &= t_n + 1 \\
I_{n+1} &= I_n R(x_n, y_n)
\end{aligned}
. \tag{4.22}
$$

The dynamics generated by these maps is illustrated in Fig. 4.15. In the case of the baker
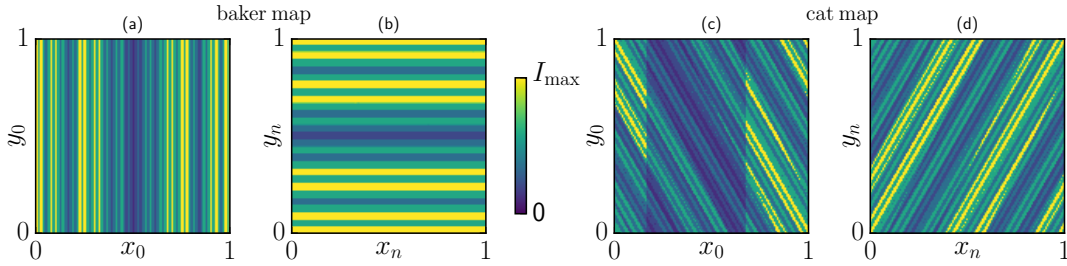
FIGURE 4.16: Intensity distributions in partially reflecting (a),(b) baker map (4.22) and (c),(d) cat map (4.22). (a),(c) projected on initial conditions: $I_n(x_0, y_0)$ and (b),(d) projected on n-th iterate: $I_n(x_n, y_n)$ with $n = 4$.

map the absorbing region was chosen in order to allow for comparison with analytical calculations. In the case of the cat map we chose an arbitrary asymmetric region. The essential point for our investigation of the role of partial opening is that both choices lead to a non-trivial D_0 for $R = 0$. In both maps $D_0 = 2$ and D_q is non-trivial, confirming the result of Ref. [APT13a] that the apparent self-similar distribution of μ observed in the phase-space is properly quantified only through the full multifractal spectrum D_q. For the baker map the calculation of the spectrum D_q can be done analytically (see Appendix C). We will use this fact to confirm the validity of our numerical approach.

In order to discuss the fractal dimensions in this system we need to define the measure we use for their calculation using a multifractal box counting method as described in Sec. 3.2.2. The stable manifold measure (see Eq. (2.22)) contained in the ith box of a partition (by a regular grid) of the phase space of a partially absorbing system with $0 < R < 1$ in a phase-space region should be proportional to the average intensity I_n for $n \to \infty$ of randomly drawn $x_0 \in \mathcal{B}_i$. The finite time normalised measure of a box $\mathcal{B}_i$ after n iterations can thus be written as

$$\mu_{n,i} = \frac{\langle I \rangle_{n,i}}{\sum_i \langle I \rangle_{n,i}}, \tag{4.23}$$

where the average intensity $\langle ... \rangle_{n,i}$ is computed over initial conditions $x_0 \in \mathcal{B}_i$. This definition is consistent with the usual definition of the stable manifold measure considering the intensities $I \in [0, 1]$ of trajectories as weights (see also Ref. [APT13b]). The unstable manifold measure equivalent can be achieved from Eq. (4.23) by computing $\langle ... \rangle_{n,i}$ over the positions $x_n \in \mathcal{B}_i$ after n iterations instead of the initial conditions. In the case $R = 0$ the measure is uniformly distributed on a fractal support and the Rényi spectrum is flat ($D_q = D_0$).

As in the simple fractal case the minimal scale of multifractal objects in any practical case is finite. That means there is a typical length on which the measure fluctuates. In the case of an partially open system that corresponds to a typical width

of areas of constant intensity. In Fig. 4.16 we report the distribution of the measure μ in the phase-space for a particular reflectivity after a few iterations. The finite size of the features is clearly visible. In the plots we show the intensity averaged over initial conditions contained in boxes in the phase space, i.e., $\langle I \rangle_{n,i}$ from Eq. (4.23) over boxes i. That means that – similar to the monofractal case – the observed dimension goes to zero once the boxes are too small to contain any points. As a result, we can observe the transitions at ℓ and δ in these systems, too.

In the following we have a look at both in more detail, but first, let us define the equivalent forms of the dimensions used in Sec. 4.1. The biggest difference is in the local dimension which we define now for the calculation along a one-dimensional slice of the phase space. We use the superscript $^{(k)}$ to denote a particular covering of boxes sized $\varepsilon^{(k)}$ and $\mu_i^{(k)}$ for the measure of the ith box of that covering.

$$D_{q,\text{loc}}(\varepsilon^{(2)}) := \lim_{|\varepsilon^{(1)}-\varepsilon^{(2)}|\to 0} \frac{\ln\left(\sum_{i=1}^{n^{(1)}} \mu_i^{(1)q}\right) - \ln\left(\sum_{i=1}^{n^{(2)}} \mu_i^{(2)q}\right)}{(1-q)\left(-\ln\varepsilon^{(1)} + \ln\varepsilon^{(2)}\right)} \tag{4.24}$$

This is the local scaling exponent of $\sum_{i=1}^{n^{(k)}} \mu_i^{(k)q}$ where $\mu_i^{(k)}$ is the measure from Eq. (4.23) in the ith box. As in the monofractal cases studied before, We call the numerically observed dimension at finite $\varepsilon^{(k)}$, and finite values of $\varepsilon^{(1)} - \varepsilon^{(2)}|$, D_{obs}. It is also usually calculated using a finite sample size approximation of μ_i. In the case $0 < R <= 1$, I_n is always different from zero and therefore – and because we restrict our sampling to the support of μ – we can for the rest of the discussion assume $S = \varsigma$. In other words, all sampled initial conditions do not escape because their intensity never reaches zero. If $S \to \infty$, or if we know the measure analytically, then Eq. (4.24) defines the real local dimension $D_{q,S\to\infty}(\varepsilon)$. This case is the infinite sampling limit of the observed dimension $D_{q,\text{obs}}(\varepsilon)$ which is the dimension obtained from a sampling approximation of μ. Furthermore, in analogy to the monofractal case, we use $D_{q,\text{eff}}(\varepsilon)$ for any non-integer $D_{q,S\to\infty}(\varepsilon)$.

Now let us consider the transition between $D_{q,\text{eff}}(\varepsilon)$ and the trivial dimension at $\varepsilon = \ell$ (see Eq. (4.5)). For the sake of a simpler notation we restrict ourselves to measures with a one-dimensional support, but as in the previous sections the arguments need little modifications to apply to higher dimensions. Assume we go from a box size $\varepsilon^{(1)}$ to a smaller box size $\varepsilon^{(2)} = \varepsilon^{(1)}/\nu$, where $\nu \in \mathbb{N}^+$. Let us also assume that $\varepsilon^{(1)}$ is already close to the typical length ℓ on which the measure fluctuates. The i-th box of the larger grid contributes the term $\mu_i^{(2)q}$ the sum in Eq. (4.24). Because the intensity is constant

over the larger box the general statement that

$$\sum_{i=1}^{n^{(1)}} \mu_i^{(1)} = \sum_{i=1}^{n^{(2)}} \mu_i^{(2)} \tag{4.25}$$

in this case implies that each of the smaller boxes contained in that box leads to a contribution of $\mu_i^{(2)q} = (\mu_i^{(1)}/\nu)^q$. Therefore we can change one of the sums to $\sum_{i=1}^{n^{(2)}} \mu^{(2)q} = \sum_{i=1}^{n^{(1)}} \nu \mu^{(2)q} = \sum_{i=1}^{n^{(1)}} \nu^{1-q} \mu^{(1)q}$. Plugging this into Eq. (4.24) leads to

$$D_{q,S\to\infty}(\varepsilon^{(2)}) = \frac{\ln\left(\sum_{i=1}^{n^{(1)}} \mu_i^{(1)q}\right) - \ln\left(\sum_{i=1}^{n^{(1)}} \nu^{1-q} \mu^{(1)q}\right)}{(1-q)\left(-\ln(\nu\varepsilon^{(2)}) + \ln(\varepsilon^{(2)})\right)} = 1, \tag{4.26}$$

if $\varepsilon < \ell$. The equivalent to Eq. (4.5) for the Rényi spectrum thus is

$$D_{q,\text{obs}} = \begin{cases} D_{q,\varepsilon\to0} & \text{for } \varepsilon \lesssim \ell \\ D_{q,\text{eff}} & \text{for } \varepsilon \gtrsim \ell \end{cases}. \tag{4.27}$$

As is the case in monofractals, ℓ is time dependent and $\ell(t) > \ell(t')$ if $t' > t$. In the example of the ternary baker map, the feature-size is decaying exponentially: $\ell(t) = 3^{-t}$.

The transition caused by finite S as defined in Eq. (4.8) is also very similar to the mono-fractal case. Once the box-size is comparable to the typical distance between samples, the observed dimension goes to zero. In the here considered case that the support of μ is a line we have $\varsigma = S$ for all times and therefore, in the multifractal case $\delta = 1/S$ is independent of the time and we can state the transition as:

$$D_{q,\text{obs}} = \begin{cases} 0 & \text{for } \varepsilon \lesssim 1/S \\ D_{q,S\to\infty} & \text{for } \varepsilon \gtrsim 1/S \end{cases} \tag{4.28}$$

We now compare the theoretical predictions to numerical results obtained in the partially open baker and cat map. In Fig. 4.17 we show the results from a numerical d_q calculation in the two maps. As in the previous sections we use a simple box-counting algorithm for $q = 0, 2, 8$.

In Fig. 4.17(a) to (c) we can immediately see the two transitions at ℓ and δ. At $1/S$ the dimension goes from zero to one and at $\varepsilon = \ell$ it drops again to the effective D_q. In the baker map we have $\ell = 3^{-8} \approx 1.5 \times 10^{-4}$ and $\ell = 3^{-12} \approx 1.9 \times 10^{-8}$ for $t = 8$ and $t = 12$, respectively, which agrees very well to the observed transition points. In the cat map, we can also observe how ℓ decreases with t. In Fig. 4.17(d) we are already in the case $\ell < \delta$, so that the transition (4.27) can not be observed. We plot this particular choice of t to show that, in this system, the value of δ stays constant even in this case.
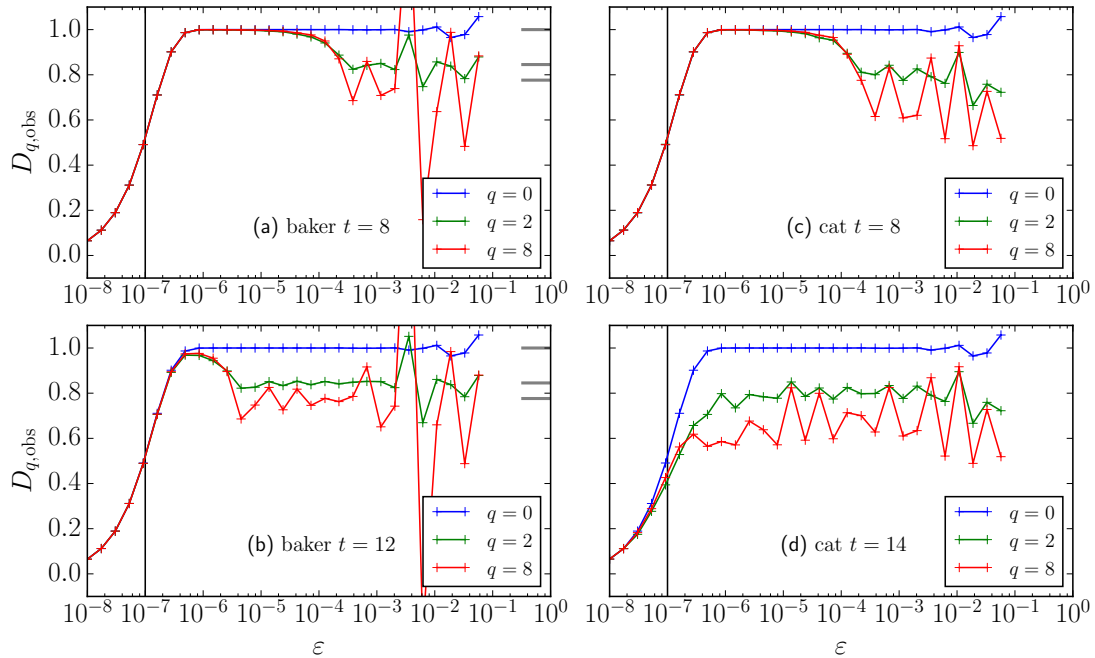
FIGURE 4.17: Numerically calculated local D_q-values for partially open baker and cat map with $R = 0.3$ at two different times t. Initial conditions were picked from a uniform distribution on a line with constant y_0. The grey markers in (a),(b) mark the analytical values of D_q (see Eq. (C.13)). The vertical lines mark $\varepsilon = 1/S$.

4.5 Conclusions

In this chapter we have defined an effective dimension related to previously considered examples of such dimensions in physical systems [LFO91, MLG03, KMBK13, MdMGK05, Gra88, LT89] and also generalised the concept to multifractals. We have expressed the finite parameters (sample size ς, iteration time t, box-size ε) in terms of two length scales ℓ and δ. We further gave a general description of their expected functional dependence on ς and t and confirmed them on the example of two monofractal model systems. Additionally we have shown that they are also identifiable in systems exhibiting a non-trivial Rényi spectrum, a necessary in order to describe partially open symplectic maps. ℓ can be intuitively interpreted as the typical size of segments in a finite-t approximation of either the trapped set or the intensity distribution of the system. Once the box size (or equivalent length scale) of any algorithm gets smaller than ℓ, no fluctuations are measured and the dimension assumes some trivial value (See Figs. 4.2 and 4.3, Tab. 4.1, and Eq. (4.5)). δ, on the other hand, intuitively is the length scale introduced by the lack of samples. Its value further depends on the fractal dimension of the (multi)fractal under consideration (see Eq. (4.10)). We have used these results to calculate optimal combinations of t and the total sample size S, $S \geq \varsigma$, to observe the effective dimension over a given range of ε (see Eqs. (4.11) and (4.12)). We expect the respective scalings

of t_{opt} and S_{opt} to apply to the algorithms discussed in Ch. 3.

In the next chapter we consider non hyperbolic systems which were shown to exhibit more than one effective dimension [LFO91, MLG03, KMBK13] and apply our methods to this class of system.

Chapter 5

Open Non-Hyperbolic Systems

So far we have considered fully chaotic systems, that is, ergodic systems in which the full phase space is chaotic. In fact, we have restricted the discussion even beyond that definition to systems that were *fully hyperbolic*, i.e., every orbit in the chaotic set is exponentially unstable. In physical Hamiltonian systems, however, the dynamics is typically more diverse. In most cases, it is neither purely integrable nor fully chaotic, but mixed, i.e., there are regions in phase space (with positive measure) that support chaotic motion and regions where the dynamics is regular (periodic or quasi-periodic). But also in the ergodic-chaotic case the dynamics often is not fully hyperbolic. Instead, we can often identify measure-zero families of orbits that have weaker than exponential instability.

In this chapter we focus on one particular implication of such non-hyperbolic dynamics: It introduces *stickiness* to the dynamics in the chaotic component, i.e., it leads to regions within the chaotic sea that trap a trajectory for some time [CS84, MO85, WHK02, Zas02]. During that time the motion is almost regular, but still, before entering the sticky region and after leaving it the trajectory is showing the exponential loss of correlation typical for chaotic motion. If a hole is introduced inside a chaotic component containing sticky regions the observed survival probability is no longer purely exponential but instead exhibits a power-law tail [NKL$^+$07, DG11b, ALV12]. Our goal is to investigate the effect of stickiness and mixed phase-space on the fractal properties of the system by studying the fractal dimension of finite-time trapped sets in such systems. It was previously shown that their fractal dimension approaches the phase space dimension as $\varepsilon \to 0$ [LFO91]. The approach to this case was shown not to happen smoothly but instead different effective dimensions can be observed [MLG03]. The effective dimension in such systems was further shown to depend on the phase-space region under consideration [MLG03, KMBK13] We show that following the line

of argumentation presented in Ch. 4 we can observe a time dependent transition in the effective dimension in such systems.

Before discussing these effective dimensions in Sec. 5.2 we begin the chapter with a review of stickiness and its implications to transient chaos in open systems. We also introduce two dynamical systems that serve as instructive examples of the different kinds of stickiness and that we later use for the numerical investigation of the effective dimension of trapped sets.

5.1   Transient Chaos in Sticky Systems

In Ch. 2 we discussed the concept of transient chaos in systems with a hole. We have shown that in fully chaotic systems the survival probability $P(t)$ of trajectories decays exponentially with time t. This means that the area of the remaining set $\mathcal{S}_t$ (See Eq. (2.16)) in such systems also decays exponentially and that it asymptotically approaches the stable manifold $\mathcal{S}_\infty$ of the chaotic saddle.

In Hamiltonian systems containing non-hyperbolic sets the picture is not that simple. What we find instead is that the survival probability at different times follows a different type of scaling [DG11b, ALV12]:

$$P(t) = \begin{cases} \text{irregular} & \text{for } t < t_I \\ a\mathrm{e}^{-\kappa t} & \text{for } t_1 < t < t_{II} \\ bt^{-\gamma} & \text{for } t_{II} < t \end{cases} \cdot \qquad (5.1)$$

The asymptotic power-law tail is due to sticky regions in the phase space which can trap trajectories that enter them for long time spans. This stickiness can happen around families of marginally unstable periodic orbits embedded in the chaotic component or in the vicinity of regular regions – the so called *KAM islands* [Ott02]. In the following we discuss both cases more thoroughly using the stadium billiard as an example for a fully chaotic system with measure-zero sets of non-hyperbolic orbits, and the standard map as an example where the stickiness is due to regular islands.
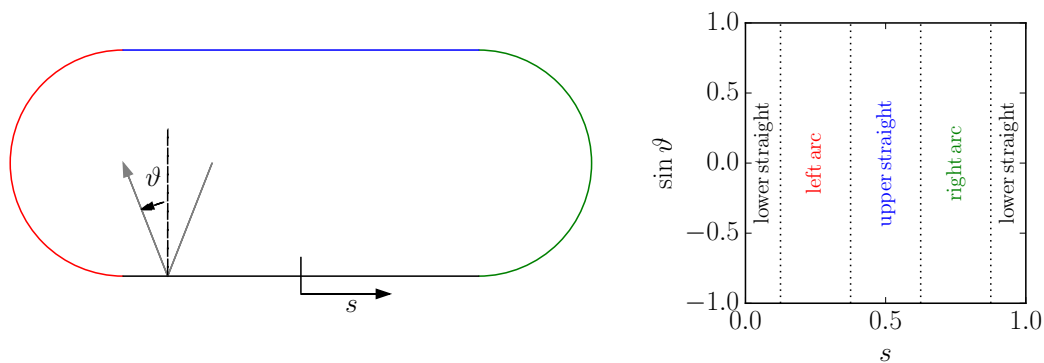
FIGURE 5.1: Sketch of a stadium billiard and the relevant coordinates: s, the position along the boundary, and ϑ, the angle of incident. The half plane with positive (negative) $\sin\vartheta$ corresponds to trajectories leaving the collision point towards the left (right) with respect to the normal vector pointing inside the billiard from that point on the boundary. For a more detailed description of the stadium see Sec. 2.2.

5.1.1 Stickiness Around Marginally Unstable Periodic Orbits within Hyperbolic Sets

Stickiness around continuous families of marginally unstable periodic orbits (MUPOs) was extensively studied in different dynamical billiards such as for example locally perturbed annular billiards [AFM$^+$08], open mushroom billiards [DG11a], drive belt billiards [DG12], open Sinai billiards [FRS94], as well as 2D maps [AS09] and other systems [GD95].

To have a closer look at this source of stickiness we here concentrate on the particular example of the stadium billiard as sketched in Fig. 5.1. We can observe the stickiness in a *closed* stadium by comparing the discrete-time evolution of bundles of trajectories emerging from close to the sticky set and from far away from it. Both bundles explore the full phase space as $t \to \infty$ but for finite times the observed distributions are very inhomogeneous.

In the top row of Fig. 5.2 we see how an initial distribution of points corresponding to a bundle of trajectories emitted from around the center of the right arc of the stadium with a angles distributed in a narrow band around the normal direction is rapidly stretched along the unstable directions and later fills a large portion of the phase space apart from empty areas containing a continuous family of MUPOs. We can see how after 5 iterations large parts of the phase space are still empty and that there is a larger density of trajectories are colliding with the top (bottom) straight with a large negative (positive) angle to the normal (i.e. facing to the left of the billiard) and around a diagonal line in $(s, \sin\vartheta)$-space spanning the s-range belonging to the left arc. It means that
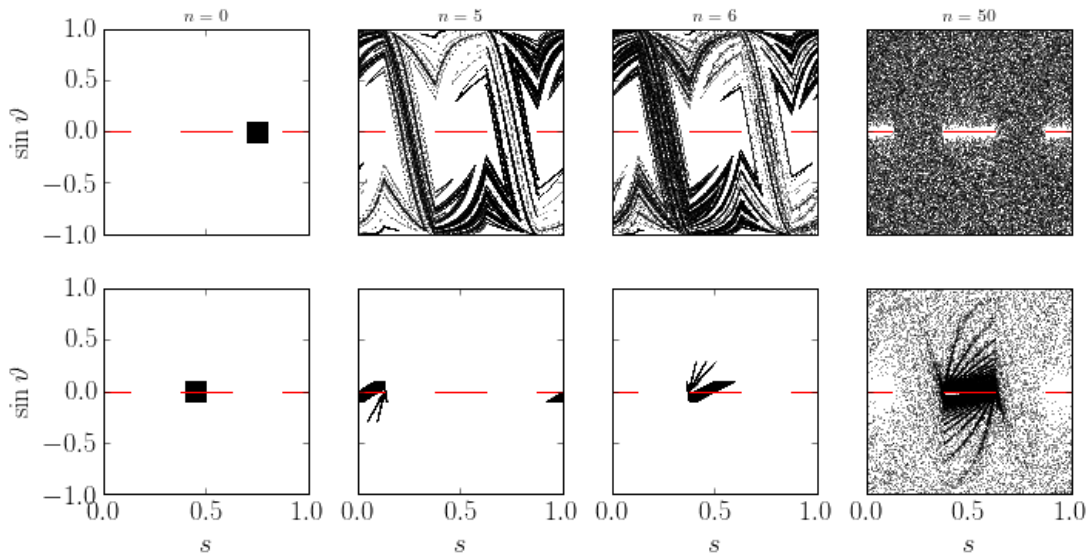
FIGURE 5.2: Evolution of two bundles of trajectories consisting of a large number of initial conditions in a stadium billiard with $L/r = \pi$. The trajectories are started within the black squares visible in the leftmost column of the panels. The columns show the nth images of the initial conditions from the leftmost panel of the respective row; the value of n is the same for both panels within each column. The red horizontal lines located at $\sin\vartheta = 0$ and spanning the intervals $s < \frac{1}{8}$, $\frac{3}{8} \le s \le \frac{5}{8}$, and $\frac{7}{8} \le s$ mark the family of MUPOs consisting of orbits bouncing back and forth perpendicularly between the straight segments of the boundary.

after 5 iterations the majority of trajectories is facing leftwards under still a relatively low angle to the parallel walls or has just hit the left arc which is intuitively expected for small odd iteration numbers of this tight "beam" of trajectories. At $n = 6$ we can quite clearly see how the left-facing trajectories that were on the straights at $n = 5$ have by now hit the left arc. The further spreading of the distribution over the phase space is also visible on the decrease of the empty region, e.g., in the center of the panels. After 50 iterations much of the empty space visible at lower iteration-numbers is filled by the trajectories.

In the bottom row we show how a bundle of initial conditions located on the top straight and containing a part of the family of MUPOs looks after the same iteration numbers. In the plots for $n = 5$ and $n = 6$ we can see how at short times the bundle is located on the top (bottom) straight for even (odd) iteration numbers. At $n = 50$ there is a distinct spike-pattern visible on which a majority of the trajectories is localised. In general, by observing the time evolution in that way we can see that the MUPOs are surrounded by an area in which orbits from the outside only penetrate very slowly while at the same time trajectories from in there take a very long time to leave.

The spike like pattern that we observe from looking at the time evolution of bundles of trajectories in the closed system is also visible when we look at the escape-time
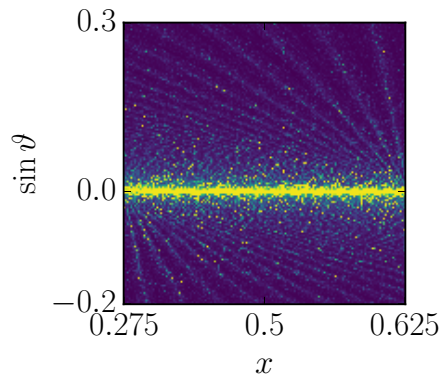
FIGURE 5.3: Escape time (real trajectory-length, not iteration number) distribution in a region on the upper straight segment containing bouncing ball orbits in a stadium with $L = 4$, $r = L/\pi$: color scale transitions from long ($t_{\text{esc}} \approx 2500$, yellow) to short ($t_{\text{esc}} \approx 10$, dark blue). The hole is independent of the angle and located at on the left arc.

distribution in the *open* version of the billiard. To do so we open the billiard by introducing a hole on the boundary. In Fig. 5.3 we display the numerically sampled escape time distribution in a relevant region of such a system. This escape-time distribution leads to triangular filled areas in $\mathcal{S}_t$ which disappear as $t \to \infty$ but which we have to consider in the calculation of an effective fractal dimension at finite times as we show in Sec 5.2. The shape of this spiky structure is discussed in great detail on the example of an open stadium in [DG09]. In Sec. 5.2 we discuss its influence on the fractal dimension of the trapped set.

5.1.2 Stickiness Around Regular Islands

In the previous section we reviewed stickiness on families of MUPOs which are measure zero sets embedded within a chaotic phase space. In this section we examine sticky regions around regular islands. In open systems ensembles of trajectories started inside these islands do not decay with time, unless the islands have a non-empty intersection with the hole. Therefore, the measure accumulates there in the limit $t \to \infty$. Regular islands are a common occurrence in Hamiltonian systems, because typically such systems are neither fully chaotic nor fully integrable. These islands are surrounded by a fractal hierarchy of smaller and smaller islands [Mei92, LT11] unless the systems are specifically designed to have islands with non-fractal boundaries [AMK05, BVA12]. The stickiness of the hierarchical interface between generic regular islands was studied extensively in both two dimensional [CS84, MO85, MO86, WHK03, Zas02] and higher-dimensional [AK07] maps.

FIGURE 5.4: Phase space of the standard map (5.2) for $\beta = 0.1$ (left), $\beta = 0.52$ (center), and $\beta = 4.3$ (right).
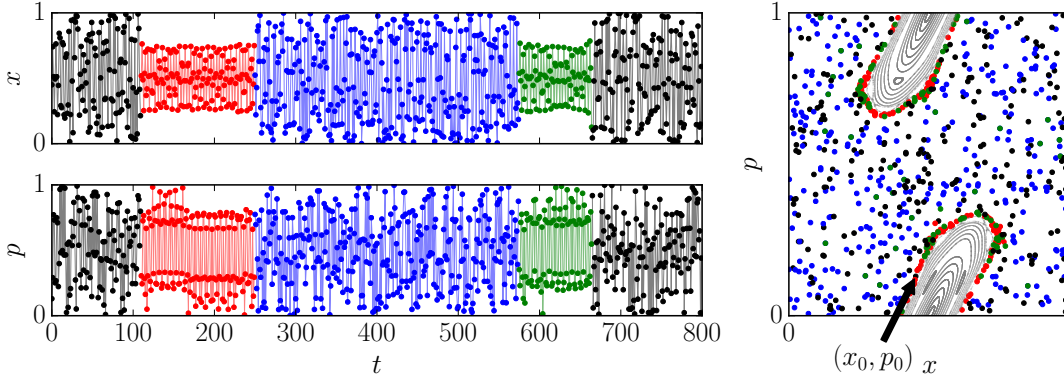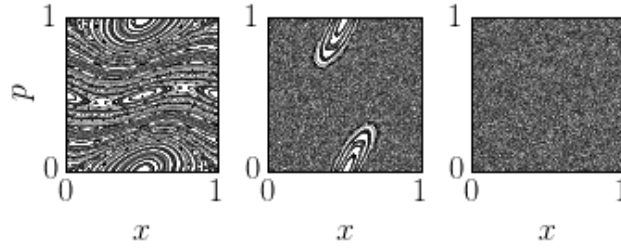

FIGURE 5.5: Part of a single trajectory in a closed standard map with $\beta = .52$. Left: time series of x and p. Right: The same trajectory plotted in phase-space. Around the fixed point $(x, p) = (\frac{1}{2}, 0)$ we show some trajectories belonging to the main regular island in grey.

The standard map is a very useful tool for the study of Hamiltonian systems with mixed phase space. It is a two dimensional mapping on a torus defined as

$$
\begin{aligned}
p_{n+1} &= p_n + \beta \sin(2\pi x_n) \mod 1 \\
x_{n+1} &= x_n + p_{n+1} \mod 1 \\
t_{n+1} &= t_n + 1
\end{aligned}
\tag{5.2}
$$

where $\beta \in \mathbb{R}^+$ is a parameter that allows to tune the mix of chaotic and regular behaviour, as seen Fig. 5.4, where we show the phase space portrait of the map with choices of β leading to almost regular (β close to 0) motion, mixed dynamics with large island for intermediate β, and fully chaotic dynamics for most large values of β.

The stickiness of the island visible in the central panel of Fig. 5.4 can be observed by looking at the time evolution a typical trajectory in this system. By comparing the time series of the (x, p)-values of a trajectory with its representation in phase space (see Fig. 5.5) we can see how the trajectory alternates between chaotic motion exploring the chaotic sea and almost regular motion during the time-intervals it is trapped by the island.

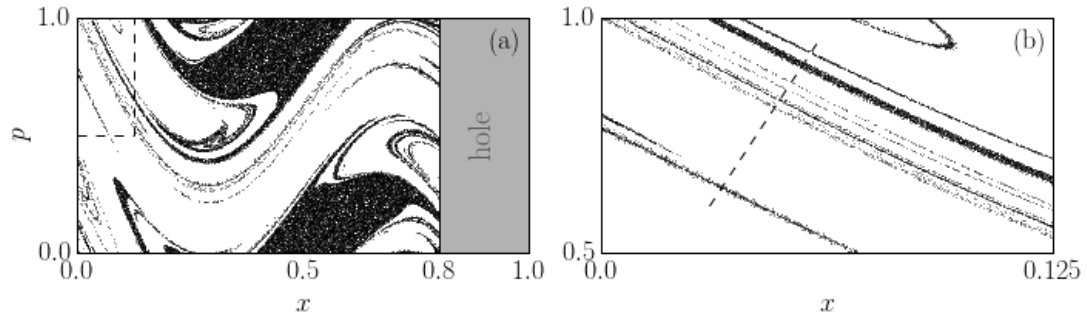FIGURE 5.6: Finite time trapped set $\mathcal{S}_{t=9}$ of a standard map (5.2) with $\beta = 0.52$ and a hole at $x > 0.8$ as indicated in grey. (a) full phase-space; (b) blow-up of area marked by dashed lines in left panel.

As in the case of the billiard, when introducing a hole in the phase space of the standard map (away from the island) this trapping leads to structures in the finite-time trapped different from what we observe in fully chaotic systems. In Fig. 5.6 we can see that the trapped set after nine iterations is dominated by a large continuous area covering the island but also extending throughout the phase space. In the zoomed-in picture we can see that in regions far from the island the set still appears to be of fractal nature, but that there is also a wider band visible that extends directly from the island. In the following section we study this in a more quantitative manner by looking at the time and box-size-dependence of reduced fractal dimensions along lines intersecting the trapped set.

5.2 Effective Dimensions in Non Purely Hyperbolic Chaotic Systems

In this section we present numerical results of the box-counting dimension in the two examples of non purely hyperbolic systems introduced above. In both cases we calculate the reduced dimension along a line intersecting the trapped set. We show that we can identify an effective fractal dimension in such systems following the theory introduced in Ch. 4 which can be roughly summarized as follows: In that chapter we have introduced the observed dimension $D_{\mathrm{obs}}(\varepsilon, \varsigma)$ which is the local slope of the number of filled boxes obtained from a box-counting algorithm at a given box-size. Here, $\varsigma = SP(t)$ is the number of sampled points that is available for the algorithm; S is the total number of sampled trajectories and $P(t)$ is the survival probability of the system. We have further shown that D_{obs} goes to zero if the box-size is smaller than the inter-sample distance $1/S$. In a similar fashion parts of the set that are smaller than $1/S$ are likely to be not found by the sampling which also leads to $D_{\mathrm{obs}} \to 0$. Lastly, assuming S is large enough,

FIGURE 5.7: Survival probability in the open
standard map obtained from random sampling
of initial conditions along the dashed line in the
right panel of Fig. 5.6. The dashed line here is
a guide to the eye following $\exp(-0.3t)$.
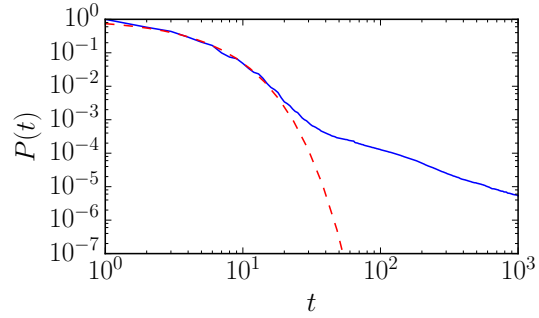
once the box-size is smaller than the typical segment size, the D_{obs} dimension goes to
the dimension of the support of the fractal set under consideration. We used these
limiting cases to define the effective dimension D_{eff} of a set as the dimension that can be
observed if at box-sizes that are larger than the features of the set and at sample-sizes
large enough to resolve the fractal set.

In the following we show that an effective dimension can also be identified in
systems which have a more complicated structure of the fractal set. As in the earlier
discussion we restrict the description to one-dimensional cuts across trapped sets of 2D-
systems but emphasize that the results are not exclusive to such systems and can also
be adapted to higher-dimensional systems. We start with numerical results in the open
standard map and later in the section identify the features observed in this system to
the true-time map of the stadium billiard.

5.2.1   Effective Dimensions in the Open Standard Map

We use the same non-linearity parameter and hole as shown in Fig. 5.6 and discuss the
dimensions along the dashed line in the right panel of that figure. We chose this line
because it crosses the apparently fractal part of the set as well as the extension of the
area covering the central island. As we show in the following, as long as it does not
intersect the island the choice of the line does not change the value of D_{eff} but it has
an influence on the box-size interval at which we can observe it. In Fig. 5.7 we can
clearly see the transition between the different types of decay of the survival probability
described by Eq. (5.1). Most noticeable is the transition from exponential to algebraic
behaviour at $t \approx 30$. We numerically calculate the box-counting dimension of the set
along that line at different iteration numbers t and collect the results in Fig. 5.8. The
decay at the mean inter-sample distance of $5 \cdot 10^{-8}$ is a sign that there are line-like
segments of comparable size present for all shown values of t. Those line-like segments
are also causing the bump that is observable for all shown times and that is caused by
the box-sizes being smaller than the typical width of the line like segments. For box
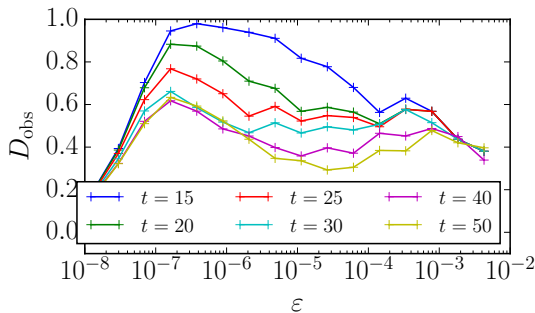
FIGURE 5.8: Numerically observed box-counting dimension in the open standard map. The sample size here is $S = 2 \cdot 10^7$ which leads to a mean inter-sample distance of $5 \cdot 10^{-8}$.

sizes larger than that we can see the effective dimension $D_{\mathrm{eff}} \approx 0.5$ before D_{obs} falls to zero which is most likely caused by the extreme sparseness of the set along this line. What is different to the fully hyperbolic case here is that for $t > 30$ there is a visible dip at intermediate box-sizes. This dip is caused by the fact that there are more than one typical length scales in a mixed system. One scale is given by the exponential shrinking (see Eq. (4.4)) of the average length of the part of the set that decays exponentially fast. The part of the set that shrinks with time following a power-law leads to another length-scale. From the results in Fig. 5.8 we can deduce that this length scale is roughly of the order of 10^6.

5.2.2 Effective Dimensions in the Open Stadium Billiard

To show that this type of behaviour is also present in systems that exhibit stickiness without having regular islands we now consider the open stadium billiard. Here we also use the true time map, i.e., instead of the iteration number we here consider the traveled distance of a trajectory. Apart from showing the general validity of the discussion, doing so also removes the singularities from the escape-time distribution that are caused by whispering gallery orbits. To study the effect of the sticky set more carefully we consider two different realisation of a hole in this system. One is located entirely on one of the arcs of the boundary the other one is slightly shifted so that it partially overlaps with the upper straight segment. In Fig. 5.9 we show an extensive comparison of the escape-dynamics in these systems. We can observe that even though at the resolution provided in the plots the escape time distribution and the trapped set look almost identical, shifting the hole to intersect the sticky set eliminates the extremely long escape times from the set. The reason for that is, that a trajectory that stays extremely long bounces almost perpendicularly between the two straight walls and therefore hits almost all points on the straight segments – including the hole. We can see the influence of shifting the hole much more clearly in the survival probability. In Fig. 5.10 we show how shifting the hole changes the shape of the survival probability curve from almost purely algebraic to almost purely exponential.
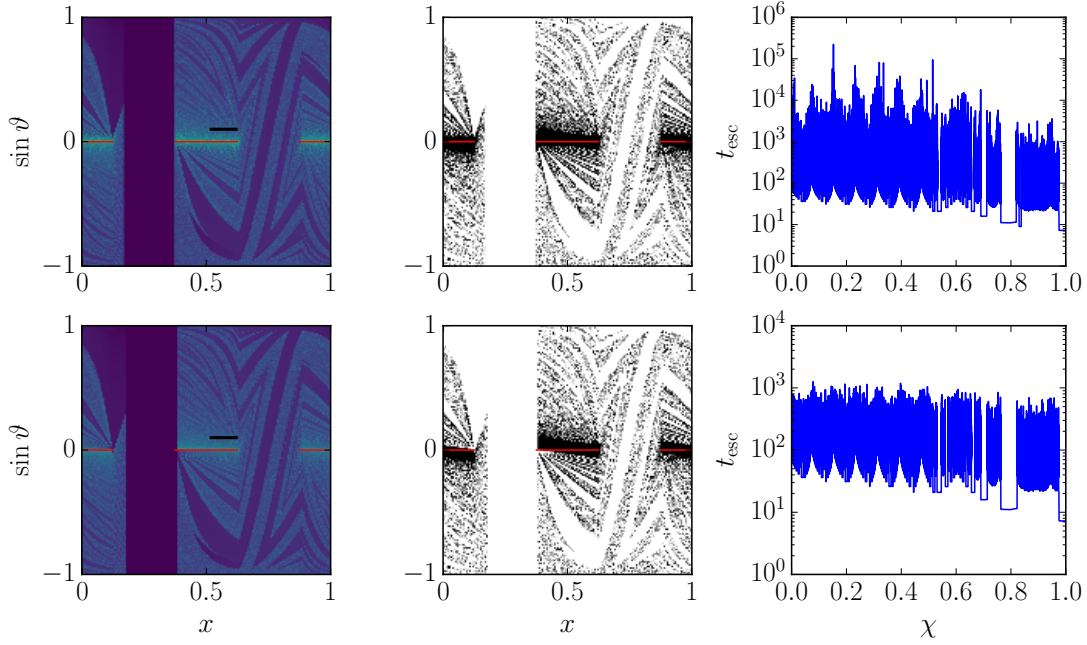
FIGURE 5.9: Comparison of the two different holes studied here; top row: hole at $0.17 \leq s < 0.37$, i.e., on the arc, and bottom row: $0.18 \leq s < 0.38$, i.e., intersecting the upper straight segment. Left column: Escape-time distribution. The colour-coding here is in a logarithmic scale to emphasize the strong fluctuation on all scales. The red horizontal lines mark the bouncing-ball MUPOs on the straight wall-segments and the shorter black line shows the line used in the dimension-calculation. Middle column: Trapped sets $S_{t=60}$ in both billiards obtained from random sampling with $S = 9 \cdot 10^4$ in the full phase-space. Right column: Escape time distribution along the black line shown in the left column; $\chi \in [0,1]$ is a coordinate along that line.

FIGURE 5.10: Survival probability in the open stadium billiards with two slightly different holes; numerically obtained by random sampling of initial conditions along the dashed lines shown Fig. 5.9. The (blue) almost purely power-law like line is for the hole on the arc; the green curve is for the hole that slightly intersects the straight segment. The dashed line here is a guide to the eye following $\exp(-0.015t)$.
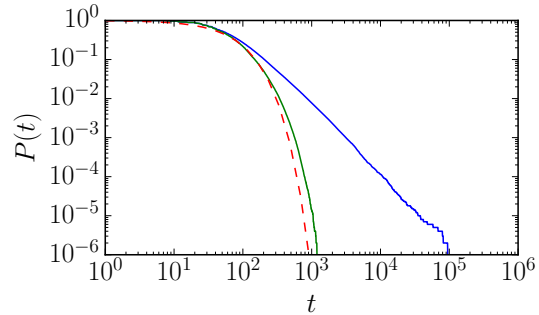
The fact that the holes are almost similar causes the effective dimension in both systems to be almost the same. This can be seen in Fig. 5.11 where for smaller times up to $t \approx 100$ we can observe the effective dimension of $D_{\text{eff}} \approx 0.9$ at box-sizes between $\varepsilon \approx 10^{-3}$ and a lower limit which is different for both choices of the hole position. In the case that the survival probability is dominated by a power-law decay this lower bound appears at $\varepsilon \approx 3 \cdot 10^{-4}$ while in the other case it significantly decreases with increasing cut-off time. The latter is an indicator that we still observe the exponentially shrinking segments there, i.e., this length-scale is still larger than the typical size of the algebraically decaying segments. At $t = 200$ the sample size is too small to resolve any
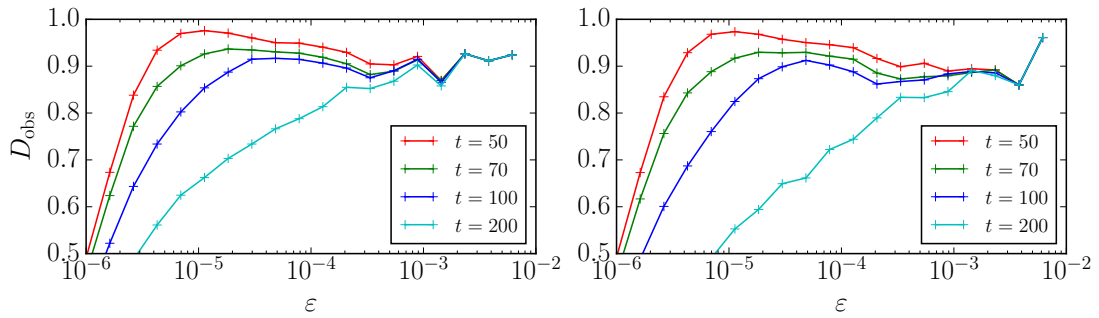
FIGURE 5.11: Numerically observed box-counting dimension in the open stadium. Left: hole entirely on a arc; right: hole intersecting the straight segment (see caption of Fig. 5.9). Here, $S = 10^6$

of the remaining segments but still the drop to $D_{\text{obs}} = 0$ is slower in the case where the hole allows for more bouncing ball orbits to exist.

In conclusion, in this section we have shown that the definition of an effective dimension made in the context of ergodic hyperbolic systems can be extended to systems that exhibit stickiness. The main difference here is that instead of a single typical length given by the exponential shrinking of the segments with time with an exponent that is the Lyapunov-exponent, here we have additional length-scales caused by the slower-than exponential decay of the part of the trapped set that is affected by the stickiness of the system. The previous results are essential to distinguish between numerical limitations and dynamics-generated deviation from the results obtained for hyperbolic systems. From the point of view of our framework of effective dimensions, the nonhyperbolic systems treated here are interesting, because they show non-trivial dependencies of D_{eff} on ε, S, and t. Other systems in which we expect this to appear, too, are for examples multidimensional systems and random maps [NOA96, BAE13].

Chapter 6

(Partially) Open Quantum Maps

In this chapter we investigate the quantum mechanical signatures of multifractality in the classical phase-space. The content of this section was previously published in [SA15]. Recent studies considered the effect of periodic orbits [PWCN12] and weak chaos [RPBF09, KMBK13, ST04] and were conducted on 4-dimensional Hamiltonian systems [RPBF09] and different area-preserving maps [PWCN12, Nov13, KMBK13, ST04]. In these systems the fractal Weyl law can be written as

$$N(|\nu_i| > |\nu|_{\text{cutoff}}) \sim M^{D_0^{(\text{S})}/2}, \tag{6.1}$$

where M is the dimension of the Hilbert space, $D_0^{(\text{S})}$ is the fractal dimension of the chaotic saddle, and $|\nu|_{\text{cutoff}}$ is a cutoff separating long-lived from short-lived states with eigenvalues ν_i. While a straightforward application of the fractal Weyl law to partially open systems predicts a trivial scaling ($N \sim M$), as also argued in [NS08], non-trivial scalings have been reported in numerical investigations [WM08]. In order to investigate the robustness of fractality in the Weyl law we study it at the transition between monofractal and multifractal. This is done by varying the reflectivity $R \geq 0$ of an absorbing region localized in the phase-space. For all nonzero reflectivities we obtain non-trivial Weyl laws with effective dimensions that show strong oscillations as a function of system size and other parameters.

We argue that these observations are due to an effective undersampling of the classical measure in the quantum regime and that the non-trivial scaling remains valid in the semiclassical limit $M \to \infty$.

6.1   Baker Map and Cat Map with (Partial)Leak

As examples of Hamiltonian chaotic systems, in this section we consider the partially open maps introduced in Sec. 4.4. We use $R \in [0, 1]$ for the reflectivity in the hole (i.e. $R = 1$ everywhere else) and consider the finite time intensity based measure in the ith box $\mu_{n,i}$ defined in Eq. (4.23) as the normalised average intensity left in that box after n iterations. For $R = 0$ in the leak, this map corresponds to the usual open maps, and the set of initial conditions with $\lim_{n \to \infty} I_n = 1$ form the forward trapped set of the map (the stable manifold of the chaotic saddle [LFO91, LT11, JT91]). In this case the measure is uniformly distributed on a fractal support and the Rényi spectrum is flat $(D_q = D_0)$.

As representative cases of the two fully chaotic area-preserving maps we investigate in detail the baker [Ott02] and the cat map [dMdA95] as defined in Sec. 4.4. In the case of the baker map the absorbing region was chosen in order to allow for comparison with analytical calculations. In the case of the cat map we chose an arbitrary asymmetric region. The essential point for our investigation of the role of partial opening is that both choices lead to a non-trivial D_0 for $R = 0$. In Fig. 4.16 we report the distribution of the measure μ in the phase-space for a particular reflectivity. The results of the numerical calculation of D_q can be found in Fig. 4.17. For the baker map the calculations of the D_q-spectrum can be done analytically (see Appendix C) and confirm the validity of our numerical methods of estimating μ_i and D_q. In both maps $D_0 = 2$ and D_q is non-trivial, confirming the result of Ref. [APT13a] that the apparent self-similar distribution of μ observed in the phase-space is properly quantified only through the full multifractal spectrum D_q.

6.2   Numerical Results on Eigenvalue Spectra

In this section we introduce the quantised version of the maps of Sec. 4.4 and compute Weyl's law (6.1). By *open quantum map* we mean a propagator [WC08]

$$\hat{\mathcal{M}} = \hat{\mathcal{U}}\hat{\mathcal{P}}, \tag{6.2}$$

where $\hat{\mathcal{U}}$ is the quantised closed system and $\hat{\mathcal{P}}$ is a projector that contains all the information about absorption. In the case of full absorption, $\hat{\mathcal{P}}$ removes the part of the quantum wave-function $\psi(x)$ that overlaps with the absorbing region, but does not alter the remaining part. In the case of partial absorption, $\hat{\mathcal{P}}$ reduces the intensity by a factor $R(x)$ as $\left| \langle x| \hat{\mathcal{P}} |\psi\rangle \right|^2 = R(x) |\psi(x)|^2$. The matrix representation of the propagator of the

quantised version of the baker map defined in Eq. (4.21) is

$$
\mathcal{M}_{\text{baker}} = \mathcal{U}_{\text{baker}} \cdot
\begin{bmatrix}
\mathbb{1}_{M/3} & 0 & 0 \\
0 & \sqrt{R}\mathbb{1}_{M/3} & 0 \\
0 & 0 & \mathbb{1}_{M/3}
\end{bmatrix}
\tag{6.3}
$$

with

$$
\mathcal{U}_{\text{baker}} = \mathbf{F}_M^{-1} \cdot
\begin{bmatrix}
\mathbf{F}_{M/3} & 0 & 0 \\
0 & \mathbf{F}_{M/3} & 0 \\
0 & 0 & \mathbf{F}_{M/3}
\end{bmatrix}
\tag{6.4}
$$

where $\mathbf{F}_{M;m,n} = \frac{1}{\sqrt{M}} \exp\left[-\frac{2\pi\mathrm{i}}{M}(n+1/2)(m+1/2)\right]$ are Fourier transformations from position to momentum representation and $\mathbf{F}_M^{-1}$ denotes the inverse transformation. For an explanation of a quantisation scheme see e.g. [BV89].

Analogously, the quantised cat map has the following form:

$$
\mathcal{M}_{\text{cat}} = [\alpha_{M;m,n}]_M \cdot
\begin{bmatrix}
\mathbb{1}_{M/6} & 0 & 0 \\
0 & \sqrt{R}\mathbb{1}_{M/2} & 0 \\
0 & 0 & \mathbb{1}_{M/3}
\end{bmatrix}
\tag{6.5}
$$

where M is even and the entries are [Kuz00]

$$
\alpha_{M;m,n} = \frac{1}{\sqrt{M}} \exp\left[\frac{2\pi\mathrm{i}}{M}\left(m^2 - mn + n^2\right)\right].
\tag{6.6}
$$

In an M-dimensional Hilbert space (effective $\hbar = \frac{1}{2\pi M}$) maps $\hat{\mathcal{M}}$ have M left (and right) eigenstates with complex energies $\epsilon_i = E_i + \mathrm{i}\Gamma_i/2$. $\hat{\mathcal{M}}$ acts like a time evolution operator so its eigenvalues ν_i are related to ϵ_i by

$$
\nu_i = \exp\left[-\frac{\mathrm{i}}{\hbar}\epsilon_i\right] = \exp\left[-\frac{\mathrm{i}}{\hbar}E_i\right]\exp\left[-\frac{1}{2\hbar}\Gamma_i\right].
\tag{6.7}
$$

Since $\Gamma_i \in \mathbb{R}_0^+$ and $E_i \in \mathbb{R}$ it follows that $|\nu_i| \in [0,1]$. Hereafter we use $|\nu_i|$ to quantify the lifetime of the state, e.g. long-lived states have $|\nu_i| \lesssim 1$ ($\Gamma_i \ll 1$).

We calculated the eigenvalues of $\hat{\mathcal{M}}$ for both the baker and cat map for different reflectivities R and matrix sizes $M = 3^n$ with $n \in \mathbb{N}$. The normalised distributions of $|\nu_i|$ are shown in Fig. 6.1. The states concentrate around a typical value $|\nu|_{\text{typ}}$, which is $|\nu|_{\text{typ}} \approx 0$ for $R = 0$, increases with R, and can be approximated as the median of $\rho(|\nu|)$. For increasing matrix-sizes M the distribution becomes more concentrated around $|\nu|_{\text{typ}}$. To investigate this tendency in further detail, and in line with the fractal Weyl law, we concentrate on the number of eigenstates with $|\nu_i| \geq |\nu|_{\text{cutoff}}$.

FIGURE 6.1: Distribution of eigenvalues $|\nu|$, see Eq. (6.7))in the quantised baker (a) and cat (b) maps. Two matrix sizes were used: $M = 3^7$ (gray line) and $M = 3^9$ (black line). The vertical dashed line marks the cutoff value used for the fractal Weyl law calculations in Fig. 6.2(a,d).
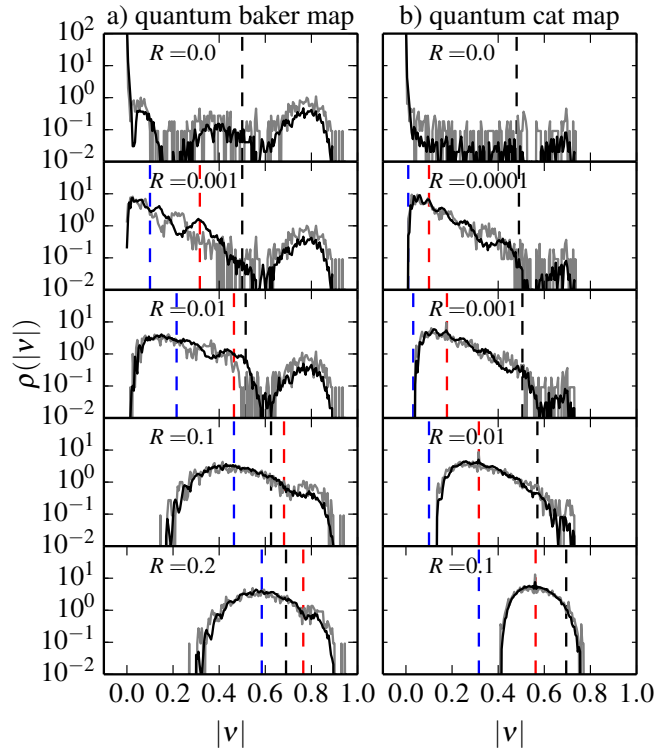
Figures 6.2(a,d) show the *relative* number of eigenstates $N(\nu_i : |\nu_i| \geq |\nu|_{\text{cutoff}})/M$ as a function of the matrix-size M. For this plot, $|\nu|_{\text{cutoff}}$ was chosen in such a way that $|\nu|_{\text{cutoff}} > |\nu|_{\text{typ}}$ but still small enough to allow the calculation of the scaling for a wide range of M, see vertical dashed lines in Fig. 6.1 [1]. The division by M allows for an improved analysis of the scaling, which according to the Weyl law prediction (6.1) should be $d_0 - 1$, where $d_0 = D_0 - 1$ is the partial fractal dimension of the forward trapped set along the unstable direction. D_0 denotes the full fractal dimension of this set. It is connected to the dimension of the chaotic saddle $D_0^{(\text{S})}$ by [LT11]

$$D_0^{(\text{S})} = 2D_0 - 2 \quad \Leftrightarrow \quad d_0 = \frac{D_0^{(\text{S})}}{2}. \tag{6.8}$$

The usual fractal Weyl law is confirmed in Fig. 6.2(a,d) for the case $R = 0$. For small R, the curves follow the $R = 0$ case for small M before deviating from it. With increasing R, the deviation is observed already for smaller M. Interestingly, even for large R and M the numerical results do not approach a constant value as predicted by the classical dimension $d_0 = 1$. Instead, a non-trivial scaling with an *effective* dimension between 0 and 1 is observed. Even if the numerical results do not allow for a conclusion regarding the scaling in the limit $M \to \infty$, the roughly constant scaling for a broad range of

---

[1]In practice, for each of the maps the number of states with $|\nu_i| \geq |\nu|_{\text{cutoff}}$ was chosen to be the same for all reflectivities at $M = 243$ (82 for cat-map): $|\nu|_{\text{cutoff}} = \min\{|\nu|_c : N(\nu_i : |\nu_i| \geq |\nu|_c) > N_c\}$ where $N_c = 60$ for the baker map and $N_c = 10$ for the cat map.
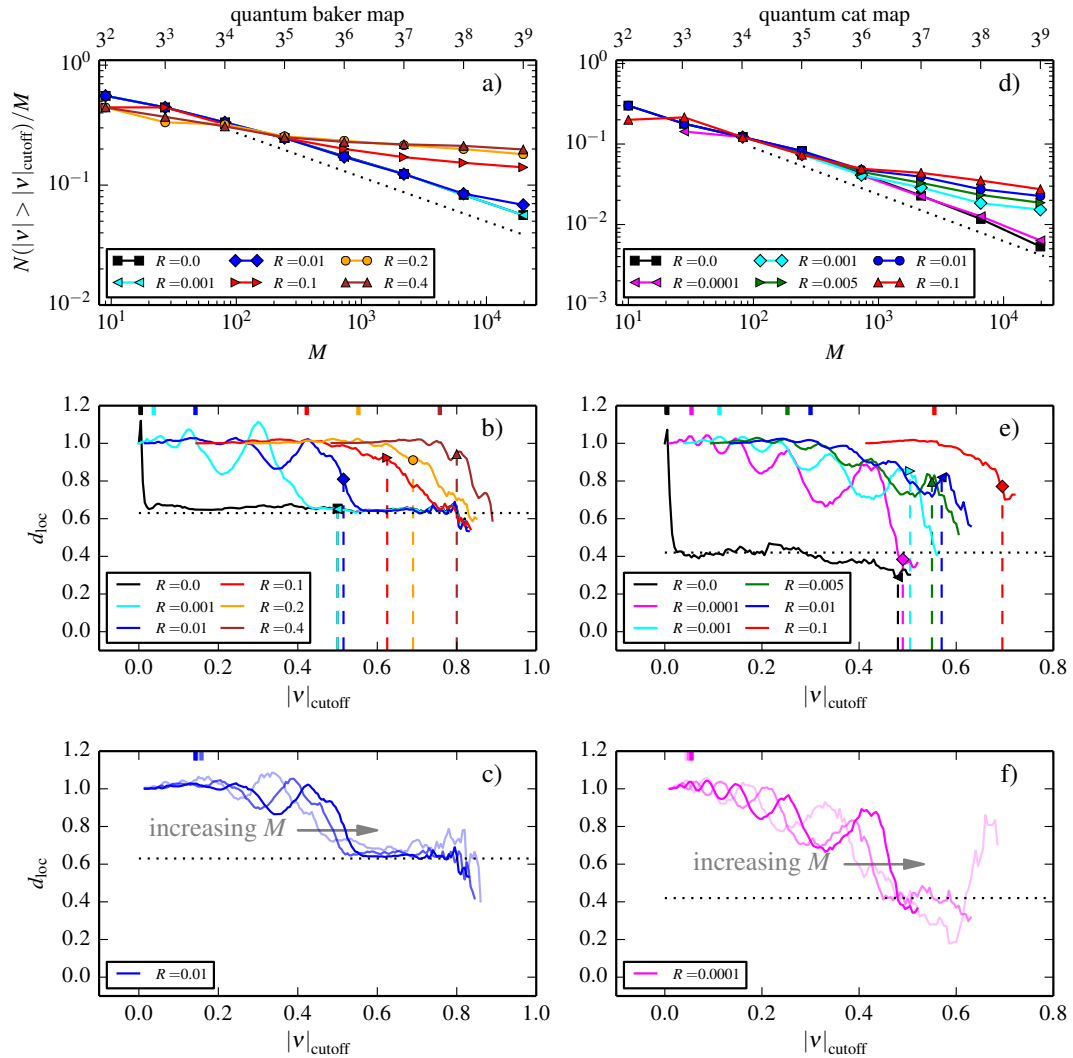
FIGURE 6.2: Scaling behaviour of the quantum states for the baker (a-c) and cat (d-f) maps. **Top row**: Fraction of eigenvalues above the cutoff value $|\nu|_{\text{cutoff}}$ as a function of the system size M at different reflectivities. The dotted lines mark the expected scaling for $R = 0$ ($d_0^{(R=0)} = \ln(2)/\ln(3)$ for the baker map and $d_0^{(R=0)} \approx 0.42$ for the cat map). **Middle row**: Local scaling exponent $d_{\text{loc}}(M) := (\ln N(M) - \ln N(M/3))/\ln 3$, where $N(M)$ denotes $N(\nu_i : |\nu_i| \geq |\nu|_{\text{cutoff}})$, at $M = 3^9$ for different values of R as a function of $|\nu|_{\text{cutoff}}$ (colors and symbols as in top row). We show results up to a cutoff where $N(M) < 0.005M$ after which point the lack of resonances leads to strong oscillations of d_{loc}. The vertical dashed lines indicate the cutoff values used in the top row. The small ticks on the upper axis mark the positions of the medians of the eigenvalue distributions ($\approx |\nu|_{\text{typ}}$). **Bottom row**: $d_{\text{loc}}(M)$ as a function of the cutoff for $M = \{3^7, 3^8, 3^9\}$ (lighter shades correspond to smaller M).

values in M shows the importance of the effective dimension (similar effective dimensions have been employed to investigate classical [MdMGK05] and quantum [KMBK13] Hamiltonian systems with mixed phase-space).

In order to more carefully analyse the scaling we define the *local* dimension d_{loc} as the slope of the N/M vs. M curves between two nearby matrix sizes M. Figures 6.2(b,e) show the dependency of d_{loc} on the choice of the cutoff $|\nu|_{\text{cutoff}}$. For small cutoffs $|\nu|_{\text{cutoff}} < |\nu|_{\text{typ}}$ we observe $d_{\text{loc}} = 1$, in agreement with the observation in Fig. 6.1 that the distribution of eigenvalues becomes concentrated around $|\nu|_{\text{typ}}$ (almost all states count as long-lived). A more interesting behavior appears for $|\nu|_{\text{cutoff}} > |\nu|_{\text{typ}}$, where at least two regimes governed by non-trivial d_{loc} can be identified before d_{loc} starts to fluctuate for $|\nu|_{\text{cutoff}} \to 1$ due to a lack of statistics: (I1) an regime of intermediate $|\nu|_{\text{cutoff}}$ with strong (almost periodic) oscillations of d_{loc}; and (I2) a regime in which $d_{\text{loc}} \approx d_0^{(R=0)}$. These regimes are particularly visible for small R (because $|\nu|_{\text{typ}} \to 0$), but can be identified also for larger R. Surprisingly, Figs. 6.2(c,f) show that regime I1 increases for increasing M (strong oscillations cover a wider range of cutoffs). This suggests that the oscillating (local) scaling is not an artifact of small M but instead that it will prevail in the large M limit.

In summary, our numerical observations of the quantum maps show surprising features. In particular: (i) the classical prediction $d_0 = 1$ was not observed; (ii) the effective scaling varies smoothly with R; and (iii) strong oscillations we observed in d_{loc} vs. $|\nu|_{\text{cutoff}}$.

6.3   Sampling Multi-Fractal Measures

In this section we propose an explanation for the scaling of the number of long-lived states with M observed in the previous section based on the classical dynamics of the system.

6.3.1   General Argument

We first consider how the usual fractal Weyl law is obtained from the classical phase-space of fully absorbing maps [LSZ03, ST04]. Lu *et al.* [LSZ03] argue that the states can be considered as non-overlapping and that each of them covers an area of $h = 1/M$. This localisation happens in the forward trapped set (for the left eigenstates [2]) [CMS97,

---

[2]We focus on left eigenstates but the same ideas apply to the right ones, which localise in the backward trapped set

KNPS06], which is smooth. Therefore, the number of *different* long-lived states depends on the distribution of the forward trapped set in the perpendicular direction (along the backward trapped set or, equivalently, along the unstable manifold of the chaotic saddle). The reasoning above leads to the following constructive classical procedure:

1. Cover an intersection of the forward trapped set with segments of size $h = \varepsilon = 1/M$.

2. Count the number N_b of boxes (segments) needed to cover the forward trapped set, which estimates the phase-space volume available to the long-lived eigenstates.

3. The number of long-lived states $N(M)$ is proportional to N_b.

Since $N_b \sim M^{d_0}$ we obtain $N(M) \sim M^{d_0}$, the fractal Weyl's law (6.1). The scaling exponent d_0 is the partial fractal dimension of the forward trapped set along the unstable direction (6.8). Schomerus and Tworzydło [ST04] provide an alternative explanation based on the phase-space areas that do not escape up to a given time (which grows with M). Both explanations are equivalent because asymptotically the h-sized boxes intersecting the invariant set correspond to the non-escaping phase-space areas.

We now generalize the ideas above to the case of partial absorption. In this case we expect for large M the long-lived states to be distributed according to the classical measure μ of the forward trapped set. Therefore, it is essential to consider a procedure that accounts for the non-uniformity of μ. In line with the usual interpretation of μ as a probability measure, we modify point 2. above and attribute to each segment i a probability p_i of being counted as long-lived (i.e., a probability that a long-lived state is localized in it). This probability has to be large (small) where the measure μ_i of the segment i is large (small) because states localise on high measure areas of the phase-space. At the same time, for large M the number of possibly long-lived states grows and p_i should grow because of the multiple chances of *one* state being localized in segment i. The simplest stochastic process agreeing with these two intuitions corresponds to performing S independent trials with a success-probability μ_i. This can be incorporated in the procedure described above by replacing point 2. by

2'. Count each segment i as part of the accessible phase-space volume with a probability $p_i = 1 - (1 - \mu_i)^S$, where $(1 - \mu_i)^S$ is the probability that the box is rejected S times.

For one realization of this process the available volume $V(M)$ is proportional to the number N_b of counted segments. Therefore, point 3. is generalised to 3'. as

$$N(M) \propto \mathrm{E}[N_b] = \sum_{i=1}^{M} p_i = \sum_{i=1}^{M} 1 - (1 - \mu_i)^S, \tag{6.9}$$

where $\mathrm{E}[...]$ is the expected value computed over multiple sampling realisations and the number of trials S is associated to the total number of states $S = S_0 M$. In the case of a fully absorbing region, $\mu_i = 1/\mathcal{N}$ for all $\mathcal{N}$ boxes intersecting the forward trapped set and $\mu_i = 0$ everywhere else. Eq. (6.9) simplifies to $\mathrm{E}[N_b] = \mathcal{N}\left(1 - (1 - 1/\mathcal{N})^S\right) \xrightarrow{S \to \infty} \mathcal{N}$ and we recover the fractal Weyl law. Analogously, in the fully reflecting case $\mu_i = 1/M$ and $\mathrm{E}[N_b] \xrightarrow{S \to \infty} M$ and we recover the traditional Weyl law.

At the heart of the reasoning above is a crucial difference between the computation of d_0 and of the Weyl scaling. d_0 is obtained by first taking the limit of sampled trajectories S to infinity $S \to \infty$ (construction of the measure) and *afterwards* computing the scaling of filled boxes in the limit of small box sizes $\varepsilon \to 0$. In the Weyl law the analogues of these two limits ($S \to \infty$ and $\varepsilon \to 0$) happen simultaneously when $M \to \infty$ because the maximum number of eigenstates grows with M ($S \propto M$) and the phase-space resolution increases with M ($h = \varepsilon = 1/M$). Therefore, the scaling in the Weyl law corresponds to the estimation of d_0 when sampling the measure with a sample size

$$S = S_0 M = S_0 \varepsilon^{-1} \tag{6.10}$$

in (6.9). The proportionality constant S_0 effectively controls how many segments (long-lived states) will be found for the different M values and therefore plays a similar role as the cutoff value $|\nu|_{\mathrm{cutoff}}$ in the quantum case.

6.3.2   Application to Baker Map

We now apply the general sampling method proposed in the previous section to the baker map (4.21)). The expected number of long-lived boxes $\mathrm{E}[N_b]$ for $\varepsilon = 3^{-n}$ can be computed analytically (see App. D.1)

$$\mathrm{E}[N_b] = 3^n - \sum_{l=0}^{n} 2^{n-l} \frac{n!}{l!(n-l)!} \left(1 - \frac{R^l}{(2+R)^n}\right)^S. \tag{6.11}$$

In Fig. 6.3 we plot Eq. (6.11) and its local derivatives as a function of its three parameters ε, S_0, and R. The similarities to the quantum observations shown in Fig. 6.2 are remarkable (the comparison is based on the identifications $\varepsilon = h = 1/M$,
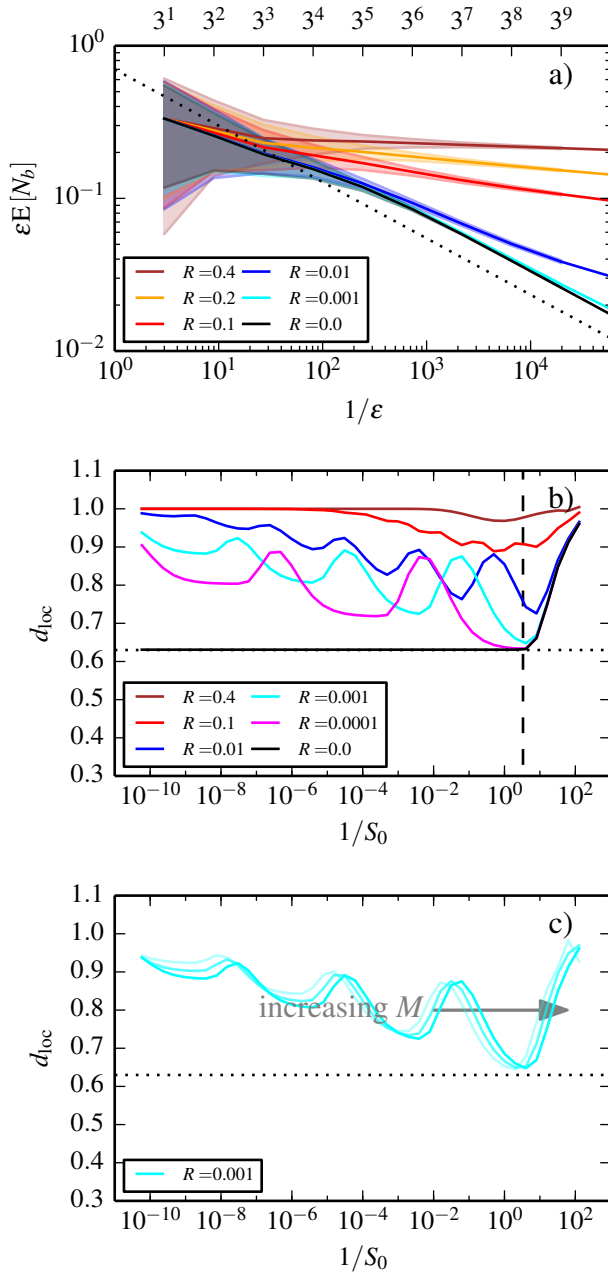
FIGURE 6.3: Scaling behaviour of the classical expected values (6.11) for the baker map. The black dotted line denotes $d_0^{(R=0)}$. a) Rescaled expected value of accepted boxes at an arbitrary sample size of $S(M) = S_0 M$ with $S_0 = 0.3$. $E[N_b]$ grows at fixed ε monotonically with R. The shaded areas cover the range between $E[N_b] \pm \sigma[N_b]$, where σ is the standard deviation. b) Scaling exponent $d_{\mathrm{loc}}(M = 3^9)$ as a function of $1/S_0$. The lower the value of R, the lower the curve intersects the dashed vertical line (the S_0 choice used in a). c) $d_{\mathrm{loc}}(M = 3^n)$ with $n \in \{7, 8, 9\}$. Lighter shades correspond to smaller M.

$N(\nu_i : |\nu_i| \geq |\nu|_{\mathrm{cutoff}}) \propto E[N_b]$, and the similar role played by S_0 and $|\nu|_{\mathrm{cutoff}}$. In particular, we reproduce the three main observations reported in Sec. 6.2: (i) the scaling of the curves is different from $d_0 = 1$; (ii) for increasing R, the effective scaling deviates more and more from $d_0^{(R=0)}$ and approaches a non-trivial dimension (Fig. 6.3(a)); (iii) the local slope d_{loc} show strong oscillations with S_0 (Fig. 6.3(b)) in a range of S_0 values which increases with M (Fig. 6.3(c)). One quantum feature which is not immediately apparent in Fig. 6.3(b) is the plateau of $d_{\mathrm{loc}} \approx d_0^{(R=0)}$, the regime I2 mentioned at the end of Sec. 6.2. To understand this we need to take a closer look at the mapping from S_0 to the cutoff $|\nu|_{\mathrm{cutoff}}$. The limiting case $S_0 \to \infty$ can be safely identified with

FIGURE 6.4: Comparison of the quantum data to the classical model. The symbols show the number of long-lived states. The solid lines are the classical values of $a\mathrm{E}[N_b]$ obtained by choosing S_0 and a for each R so that the rightmost two points of the quantum data are matched as close as possible.
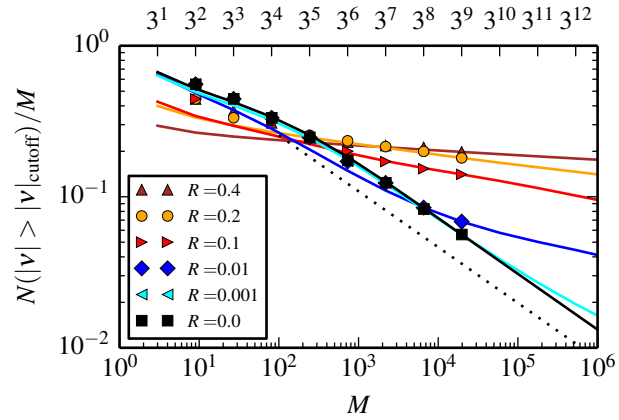
$|\nu|_{\mathrm{cutoff}} \to 0$. In this limit our model correctly reproduces the quantum observations ($d_{\mathrm{loc}} \to 1$). The identification of the opposing limit $S_0 \to 0$ with $|\nu|_{\mathrm{cutoff}} \to 1$ is also possible but less meaningful, since in this limit both the number of resonances, and N_b become very small, and as a result the determination of d_{loc} becomes prone to fluctuations. Between these limits, we can assume that $1/S_0$ grows monotonically with $|\nu|_{\mathrm{cutoff}}$. However, the functional form relating $1/S_0$ and $|\nu|_{\mathrm{cutoff}}$ is unknown (e.g., it depends on the distribution of eigenstates) which does not allow for a careful quantitative comparison of the two plots (e.g., a non-linear transformation of the x-axis in Fig. 6.3(b) could generate the plateaus around $d_0^{(R=0)}$ seen in Figs. 6.2(b,d).

We now search for a quantitative comparison between our classical sampling model and the quantum observations. The only parameter we have to fit is S_0 in the sampling model, which according to the arguments of Sec. 6.3.1 should reproduce the *scaling* of the long-lived states with *large M*. Accordingly, for each value of R we choose the value of S_0 which reproduces the local slope between the last two N/M points in the quantum data (Figs. 6.2(a,d)) and we shift the $\mathrm{E}[N_b]$ curve obtained to match the rightmost point of each quantum data-set (this last shift fixes the proportionality factor a in $N(M) = a\mathrm{E}[N_b]$). We restrict S_0 to the range $[3^{-1}, 3]$, so that S is of the order of M since these values give the best agreement with the whole range of quantum data. Because of the oscillations in d_{loc} there may be more than one choice of S_0 [3]. The results for the different R shown in Fig. 6.4 confirm that our model describes the data also for values of M much smaller than the region used in fixing S_0, a.

The quantitative success of our sampling model motivates us to consider its behavior in the semiclassical limit $M \to \infty$. In Fig. 6.5(a) we plot Eq. (6.11) in an increased range of $M = 1/\varepsilon$ values using for the different R curves the value of S_0 used in Fig. 6.4(b) (estimated from the quantum data). We again see the presence of

---

[3]The asymptotic behaviour is essentially the same for different possible choices of S_0
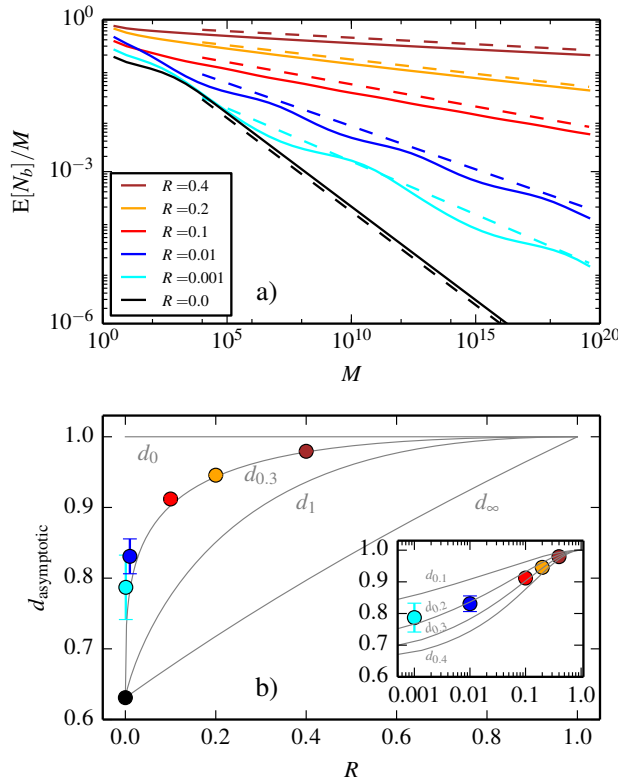
FIGURE 6.5: Asymptotic scaling of the classical prediction. a) Extrapolation of $\mathrm{E}\,[N_b]$ of the curves in Fig. 6.4(a) without the shift (i.e. $a = 1$). R increases from the black (bottom) to the brown (top) curve. The dashed lines follow the asymptotic scaling $M^{d_{\mathrm{asymptotic}}-1}$ with $d_{\mathrm{asymptotic}} = \langle \frac{\ln N(M) - \ln N(M')}{\ln M - \ln M'} \rangle$, where the average is computed over all possible combinations $\{(M, M') : M' < M \wedge (M, M') \in \{3^{10}, 3^{11}, \ldots, 3^{40}\}^2\}$. In b) we show these dimensions together with their standard deviations. In grey are analytically obtained d_q curves, see Eq. (C.13). Note, that for fixed R and $q \in \mathbb{R}^+$, $d_0 \geq d_q \geq d_\infty$ [Ott02].

log-periodic oscillations (see Ref. [Sor98] for a review on log-periodicities in fractals). While these oscillations play a major role in d_{loc} and for the range of M accessible in the quantum computations, they do not hinder the estimation of an asymptotic dimension $d_{\mathrm{asymptotic}}$ as the general trend of the curves. For $R = 0$ the results confirm that for $d_{\mathrm{asymptotic}} = d_0^{(R=0)}$ and that our sampling correctly accounts for the usual fractal Weyl law. More interestingly, $d_{\mathrm{asymptotic}} < 1$ for all R, strongly suggesting that the non-trivial scaling d_{loc} observed in the quantum data are *not* finite M effects but persist in the asymptotic limit. This implies that the fractal Weyl law of partially open systems does not follow the classical prediction $d_0 = 1$. Comparing the R dependence of $d_{\mathrm{asymptotic}}$ with the analytical calculated d_q indicates that roughly $q \approx 0.3$ can be used to estimate this scaling.

In summary, we have investigated the statistical properties of long-lived eigenstates of chaotic systems with partial absorption. Contrary to the naive prediction obtained combining the classical fractal dimension d_0 and the fractal Weyl law, we observe numerically that for a broad range of parameters the number of long-lived states grows sub-linearly with the dimensionality M of the Hilbert space. We explain these observations by considering a model which is consistent with the quantum to classical correspondence in the semiclassical limit $M \to \infty$ but that accounts for an undersampling of the classical measure at finite M. This undersampling combined with the strong

spatial fluctuations of the multifractal classical measure is responsible for the effective reduction of the available phase-space volume for long-lived eigenstates.

Our most surprising finding is that even the asymptotic ($M \to \infty$) scaling of the number of long-lived states differ from the $d_0 = 1$ prediction. This result is compatible with our numerical simulations at least for a broad range of cutoffs in $|\nu|$. In any practical situation the limit $M \to \infty$ is not achievable and the relevance of our model is that it allows to understand the effective dimension observed quantum mechanically. We have also considered alternative models in which we assume that the eigenstates concentrate exclusively on the phase-space regions with highest measure μ, or on boxes with a μ-dependent probability that we compute without including a sampling process. None of these models is able to reproduce the quantum observations, see Appendix D.2.

Our results are not limited to area-preserving maps or to systems with localized absorbing regions. Instead, they should be visible in systems of any dimension for which a multifractal spectrum of a classical measure μ appears. In n-dimensional systems the long-lived resonances are expected to concentrate in n-cuboids of volume h and the sampling has to be carried out on a hyperplane intersecting these volumes. In general partially-absorbing systems there is no analogous fully open system ($R \to 0$ for the cases above). In these cases, the scaling of Weyl's law is expected to follow the dimension of the regions of highest probability[4] for small M (analogous to d_0 of the $R = 0$ case in the examples above) and show a transition towards the dimension $d_{\mathrm{asymptotic}}$ of the undersampled μ (for the large M case). The multi-fractality in the localization of wave functions can appear also without a clear classical counterpart, e.g. in the case of phase transitions in disordered systems [EM08, MGMGG10]. It would be interesting to investigate whether the number of such states show similar dependencies on system size as the ones we observed.

---

[4]The d_0 of the peaks is different from d_q for $q \to \infty$.

Chapter 7

Conclusions and Outlook

7.1 Summary and Open Problems

1. **Dimension algorithms**

   We have reviewed the fractal dimension algorithms most commonly used in the study of dynamical systems and compared them with regard to their applicability in the fully and partially open systems discussed in this work (Sec. 3.2.1). We have presented an improved numerical method suitable to calculate the full spectrum of Rényi dimensions D_q of asymptotic stable manifold measures μ_s defined in Eq. 2.24 based on an iterative refinement of the search for initial conditions $x_0 \in \mathrm{supp}(\mu_s)$ (Sec. 3.2.2). The method significantly reduces oversampling of densely populated areas in the phase space and is trivially parallel, which allows an implementation, for example on graphics cards. We have also shown that the definition of the effective dimensions allows to computationally recognise the resolution-range in which the algorithm produces trustworthy results (Sec. 4.2, App. B). This method is not specific to the algorithm we used but instead it can be applied to any sampling-based dimension calculation in open systems.

2. **Effective dimensions in strongly and weakly chaotic systems**

   With the help of the example of finite-time t approximations of trapped sets in fully open, strongly chaotic dynamical maps we have developed a theory explaining the behaviour of the observed dimension $D_{\mathrm{obs}}(S, t, \varepsilon)$. Its value depends on the number of sampled initial conditions S, the iteration time t used in the approximation of the trapped set, and the box-size ε used to observe the set. We have identified two transition points ℓ and δ separating the ε-intervals characterised a particular value of $D_{\mathrm{obs}}(S, t, \varepsilon)$ (see Eqs. (4.5) and (4.8)). Based on dynamical and statistical arguments we have obtained the scaling of ℓ and δ with S and t (see Fig. 4.3 and Eqs. (4.4), (4.9)).

We have further demonstrated that ℓ and δ define an interval of box-sizes that leads to a value of $D_{\mathrm{obs}}(S, t, \varepsilon)$ which is not the result of the choice of S, t, or ε, but instead is an intrinsic property of the dynamical system. We call this dimension the *effective dimension D_{eff}* of the set (see Tab. 4.1). Using the analytically treatable open tent map we have proposed an algorithm to numerically find ℓ and δ in a numerical box-counting dimension calculation (see Fig. 4.9 and related discussion), which enables us to automatise the identification of trustworthy results of such an algorithm. We have confirmed the numerical method by demonstrating the agreement of the results with analytical predictions. In Secs. 4.3 and 4.4 we have applied our method to a fully hyperbolic open stadium billiard and two partially open dynamical maps. With these examples we have shown that the validity of our theory also extends to more complex and physically more relevant systems.

3. **Application to open systems with stickiness**
   In Sec. 5.2 we have shown a further possible application of our theoretical framework. We have studied numerical results of box-counting dimension calculations in an open standard map (see Fig. 5.8) which is a system with a mixed phase space, and in an open stadium billiard (see Fig. 5.11) which is ergodic chaotic but has sticky families of marginally unstable points. On the results we have shown that in such systems we can identify a non-constant effective dimension which depends on the iteration time and is caused by competing length scales resulting from the stickiness. We have confirmed this by comparing two realisations of the open stadium billiard which are almost identical but have different sticky sets.

4. **Discussion of the fractal Weyl law in systems with partially absorbing leaks based on another kind of effective dimension**
   We have presented numerical results on the eigenvalue distribution of partially open quantised maps (baker map and cat map, see Fig.6.1) for wide ranges of both reflectivity parameter R and Hilbert space dimension M. We have numerically studied the scaling of the number of long lived resonances as a function of M (see Fig. 6.2). In Sec. 6.3.1 we have provided a statistical model, based on the interpretation of the (un)stable manifold measure as the probability to successfully sample a point in a particular region of the classical phase space, to describe the observed scaling of long lived eigenstates (see Sec. 6.3.2). We have shown that our model recovers the known limiting case of the fractal Weyl law defined in Eq. 6.1 in the limit $R \to 0$ and quantitatively describes numerical observations in the quantum baker map (see Fig. 6.4). We have further shown that for large M our model predicts a scaling of the number of resonances with M described by an effective dimension that can not be identified with any of the Rényi dimensions of the (un)stable manifold measure. The results were published in [SA15].

While our theory of effective dimensions in ergodic, fully hyperbolic, open and partially open systems is self-consistent, there are still some interesting open questions in the context of its application to more complex systems. In systems with stickiness we have so far only been able to identify the time-dependent D_{eff}. A theory of the observed transition point between the two possible values is still lacking. Similarly, while we do have shown that our general theory is not restricted to one-dimensional systems, a quantitative description of the expected effective dimensions in multidimensional systems is not available. Such systems are characterised by more than one Lyapunov exponent, and as a result of that we expect there to be more than one typical length scale ℓ. At fixed t, this leads to an ε-dependent effective dimension. In the context of partially open quantum maps, an interesting open question is the origin of the log-oscillations of the local dimension that are present in both the quantum mechanical and classical observations.

7.2 Discussion and Outlook

In this thesis we have discussed fractal dimensions in a wide range of physically relevant model systems. The systems we have studied previously recognized generalisations of the already widely studied case of asymptotic dimensions in open systems. One of the generalisations is to allow partial absorption described by a reflection coefficient R in a region of the phase space which allows to bridge the gap between fully open ($R = 0$) and fully closed ($R = 1$) systems. With that, we have been able to confirm the validity of our predictions in these well studied limiting cases. On the other hand, we have considered the generalisation of fractal dimensions, not only to the case of finite scales ε, but also to the regime of finite sample sizes S and finite iteration times t. The study of partial absorption has been motivated by the fact that, in physical systems, full absorptions is an exception rather than the norm. Therefore, a ray-based modeling of experimentally realised leaky systems such as optical microcavities and microwave resonators is accurately possible only by considering partial absorption. The consideration of finite S and t on the other hand has been motivated primarily from a computational perspective. A secondary motivation for the discussion of finite t is the fact that physical fractals found in nature can not be self similar down to infinitely small length scales. Furthermore, such length scales can be meaningful observables in dynamical systems and therefore their identification provides insight into the dynamics of such systems. We have further found that a finite sample size allows to model the behaviour of leaky quantum maps from a classical perspective.

The central concept in the research we have presented in this work is that of the *effective dimension* which we have defined as the exponent of the scaling with ε – the finite box size used in the observation – of a function of an approximation of the asymptotic measure. The approximation of the invariant measure is taken at finite time and with a finite sample size. The resulting dimension is usually different from the value obtained from the strict asymptotic definition of the Rényi dimension spectrum, but it is defined in the regime that is physically most relevant – as described in the previous paragraph. Nonetheless, it has the usual Rényi dimension as limiting case. We have discussed the concept in two main areas. In the first chapters of this thesis we have defined and calculated effective dimensions in classical systems and later we have used the concept to describe results obtained in the examination of partially open quantised maps. In the following we discuss both separately and also discuss possibilities of applying our results to other fields of study.

We have given a full description of the possible observed dimensions as a function of time, box-size, and sample size in leaky, strongly chaotic classical systems and confirmed our predictions analytically in the open tent-map. We have also connected the results to well established dynamical quantities such as the Lyapunov exponents and the escape-rate. We have further shown that the description is valid also in physically relevant models such as partially open, mixed, and non-uniformly hyperbolic dynamical systems. In the latter case, our method extends the known scale-dependent effective uncertainty exponents to a description that allows the calculation of the full Rényi spectrum of the natural measure as well as the (un)stable manifold measure based on the intensity distribution. This fact makes us confident that our results can also help with the description of other systems that exhibit a non-trivial behaviour of D_{eff}. The first class of such systems is made up of multidimensional systems. In the one-dimensional strongly chaotic systems we have studied in detail, the typical length scale ℓ of the segments in the finite-t trapped sets scales as $\ell \sim \exp(-\lambda t)$. Multidimensional systems have more than one positive Lyapunov exponent which leads us to expect that there is a relevant length scale associated to each of them. As a result of this, we expect the value of D_{eff} to change at those length scales. A second class of systems we expect to show a non-trivial D_{eff} that can be described using our findings, is that of random maps which were shown to exhibit a fluctuating fractal dimension that also depends on the box-sizes used in its estimation [NOA96, BAE13]. In the context of nonhyperbolic dimension it would be interesting to explicitly study the position-dependent dimensions observed for example in hierarchical decomposition of systems with mixed phase space which have been found to have different fractal dimensions on different levels of the hierarchy [KMBK13]. Our findings are of interest in this type of system, for example if the multifractality of the chaotic saddle and its manifolds in each level is to be considered.

In the context of open quantum maps we have numerically studied the eigenvalue spectra of chaotic quantum maps with partial leaks. The prediction of the fractal Weyl law based on D_0 of the classical trapped sets, for partially open systems, predicts a linear scaling of the number of surviving eigenstates with the dimension M ($\hbar_{\text{eff}} := 1/M$) of the Hilbert space. We have shown that if the scaling of the number of longest living eigenstates is considered instead, its dependence on M is non-trivial. With help of a statistical model – identifying M with an effective sample size and using the intensity distribution in the classical system as a probability distribution in a sampling process – we have successfully reproduced the observed scaling. We have further shown that this process leads to an effective dimension for large M which leaves us confident that the observed scaling is not a finite-$\hbar_{\text{eff}}$ effect and that similar scalings can be observed in other systems. One particular possible field of application is that of experimental setups of microwave billiards with absorbers [MSKB$^+$03]. When partial reflection at the absorber is considered we expect our findings to describe the observed spectral properties. Another possible application lies in the field of phase transitions in disordered systems [EM08, MGMGG10] where multi-fractality in the localisation of wave functions can appear without having a classical counterpart.

In summary, in this thesis we have developed a framework for the definition and investigation of effective dimensions of fractal sets and multifractal measures. These dimensions are meaningful for the description of the dynamics and they are defined far from the usual asymptotics of infinite resolution, infinite self-similarity and infinite sample size. In our framework we relate the parameters S, t, ε expressing this non-asymptotic regime to length scales. We have provided a theory to describe the dependence of these length scales on S, t, ε and we base our definition of effective dimensions on them. We have applied this framework to strongly and weakly chaotic classical leaky systems and have demonstrated that the applicability also extends to systems with partial leaks (in which case the multifractal investigation is essential). For quantised, partially open, chaotic systems, we have proposed a model to explain observations comparable to the fractal Weyl law in open systems. This model is centered around the definition of an effective scaling based on undersampled multifractal intensity distributions of the underlying classical system. We have also shown that our findings can be used to define optimal parameter choices for numerical algorithms.

Appendix A

Order Statistics

Here we show that the distribution of samples on line-like objects can be calculated using order statistics following the discussion in Ref. [SM14]. We start with a set of ς samples $\{\tilde{x}_i\}$ drawn from a uniform distribution on the unit interval $[0, 1)$. If we order $\{\tilde{x}_i\}$ in ascending order we get a new set $\{x_i\}$. The i-th entry of the set is called the i-th order statistics and since $\{\tilde{x}_i\}$ are drawn from a uniform distribution the x_i follow a beta distribution

$$x_i \sim B(i, \varsigma + 1 - i) \tag{A.1}$$

We can use this fact to calculate the expected value of the spacing between two neighbouring samples:

$$\mathrm{E}[x_{i+1} - x_i] = \mathrm{E}[x_{i+1}] - \mathrm{E}[x_i] = \frac{i+1}{\varsigma + 1} - \frac{i}{\varsigma + 1} = \frac{1}{\varsigma + 1}, \tag{A.2}$$

where we used that $\mathrm{E}[X] = \frac{a}{a+b}$ if $X \sim B(a, b)$.

So, for the time-zero trapped set, $\mathcal{S}_0$ the typical inter-sample distance is $\mathrm{E}[x_{i+1} - x_i] = 1/(S + 1)$, because at $t = 0$ none of the S samples can be outside the set and $\varsigma = S$. Because in all relevant scenarios $S \gg 1$ we will approximate the expected value by $1/S$. With that our prediction for the transition point here is $\delta = 1/S$.

Appendix B

Numerical Algorithm for Tent Map

To calculate the transitions between the different values of the observed dimension D_{obs} discussed in section 4.2 we apply the following steps:

1. a) Calculate the escape-time for $S_{\text{tot}} = 10^7$ initial conditions drawn from a uniform distribution over $[0, 1)$. This leaves us with a set $Q = \{(x_{0,i}, t_{\text{esc},i})\}$ containing the S_{tot} results.

   b) Pick $n = \max(\{10, \lfloor S/S_{\text{tot}} \rfloor\})$ non-overlapping random subsets of Q_S for values of S distributed logarithmically equidistant (i.e. the ratio of any two subsequent values of S is constant) over $[10^3, 10^7]$.

   c) From every Q_S approximate $\mathcal{S}_t$ as the subset $\tilde{\mathcal{S}}_t := \{x_{0,i} \in Q_S : t_{\text{esc},i} \geq t\}$ for $t = 1, 2, \ldots, 29$.

   d) Apply a simple box-counting algorithm to all n approximations $\tilde{\mathcal{S}}_t$ using 40 box-sizes $\varepsilon_i \in [10^{-8}, 1]$ with $\ln(\varepsilon_i/\varepsilon_{i-1}) = const.$ to get n datasets containing the number $n_{\text{filled}}(\varepsilon)$ of boxes containing elements of $\tilde{\mathcal{S}}_t$.

   e) We then use the local derivative as the ε-dependent observed dimension

   $$D_{\text{obs}}\left(\varepsilon = \frac{\varepsilon_i + \varepsilon_{i+1}}{2}\right) = \frac{\ln n_{\text{filled}}(\varepsilon_{i+1}) - \ln n_{\text{filled}}(\varepsilon_i)}{\ln \varepsilon_{i+1} - \ln \varepsilon_i}, \tag{B.1}$$

   which leaves us with n curves of D_{obs} for every (S, t) combination.

2. a) First we estimate δ. Here we define a window Δ_ε and then find the position ε_{max} where D_{obs} at small ε reaches a maximum. The criterion we use is that ε_{max} is the smallest box-size for which $\partial_\varepsilon D_{\text{obs}}(\varepsilon_i) < c$ for all $\varepsilon_i < \varepsilon_{\text{max}}$ with $|\ln \varepsilon_{\text{max}} - \ln \varepsilon_i| < \Delta_\varepsilon$. In other words, ε_{max} is the largest box-size in the ε-interval in which D_{obs} increases monotonically with ε at the smallest used box-sizes.

   b) We only need a very rough estimate in step a) since δ is now approximated as the value of epsilon, where the local derivative of D_{obs} is the largest. For every (S, t) we pick we get n values of δ from this approach.

   c) Estimate ℓ using the fact that ℓ depends on t: We use a strict criterion and require $D_{\text{obs}}(\ell, t) > D_{\text{obs}}^{(S)}(\ell, t')$ for all (S, t') with $t' > t$. In other words, we pick the value

of ε, where the dimension curve starts to deviate from all the curves obtained with higher values of t. Repeat that process for all realisations with the same S and t.

3. Because of our numerical definition of ℓ the location of the smallest value of ℓ is the optimal choice of t at this S (4.11). So for each S we estimate t_{opt} as the average over the locations of the smallest 4 values of the average value $\langle \ell \rangle$ computed over all n results we obtained for ℓ at any given t.

Appendix C

Analytical dimension spectrum of the partially open baker-map

Let $R_{\mathrm{L,M,R}} \in [0,1]$. After the first iteration the intensity in the top horizontal third is R_{L}, the central strip has an intensity of R_{M}, and the bottom third carries R_{R}. The total intensity is

$$I_{\mathrm{tot},1} = R_{\mathrm{L}} + R_{\mathrm{M}} + R_{\mathrm{R}}. \tag{C.1}$$

The next iteration gives the following total intensity:

$$
\begin{aligned}
I_{\mathrm{tot},2} = \quad & R_{\mathrm{L}}^2 + R_{\mathrm{L}}R_{\mathrm{M}} + R_{\mathrm{L}}R_{\mathrm{R}} \quad + \\
& R_{\mathrm{M}}R_{\mathrm{L}} + R_{\mathrm{M}}^2 + R_{\mathrm{M}}R_{\mathrm{R}} \quad + \\
& R_{\mathrm{R}}R_{\mathrm{L}} + R_{\mathrm{R}}R_{\mathrm{M}} + R_{\mathrm{R}}^2
\end{aligned}
\tag{C.2}
$$

and so forth. At the nth step we obtain the total intensity

$$
\begin{aligned}
I_{\mathrm{tot},n} &= \sum_{k=0}^{n} \sum_{l=0}^{n-k} \binom{n}{k,l} R_{\mathrm{L}}^k R_{\mathrm{M}}^l R_{\mathrm{R}}^{n-k-l} \\
&= (R_{\mathrm{L}} + R_{\mathrm{M}} + R_{\mathrm{R}})^n
\end{aligned}
\tag{C.3}
$$

Here we used the fact that the number of strips with a certain combination of reflectivities $R_{\mathrm{L}}^k R_{\mathrm{M}}^l R_{\mathrm{R}}^{n-k-l}$ is given by the multinomial coefficient $\binom{n}{k,l} := \frac{n!}{k!l!(n-k-l)!}$.

Now we focus on the multifractal dimension spectrum (3.3) of the distribution generated by this map. First, since the measure is constant in the horizontal direction, we can restrict ourselves to a vertical line and calculate the partial dimensions d_q along this line. Assume this line is covered by disjoint segments of length $\varepsilon = 3^{-n}$. The dimensions of the full distributions are then simply obtained from

$$D_q = 1 + d_q \tag{C.4}$$

with

$$d_q = \frac{1}{1-q} \lim_{n \to \infty} \frac{\ln \sum_{i=1}^{3^n} \mu_i^q}{n \ln 3}. \tag{C.5}$$

Here μ_i is the intensity on the i-th segment normalised by $I_{\text{tot},n}$, so that

$$\sum_{i=1}^{3^n} \mu_i = 1 \tag{C.6}$$

Or, again using multinomial factors:

$$\sum_{k=0}^{n} \sum_{l=0}^{n-k} \binom{n}{k,l} \mu_{n;k,l} = 1 \tag{C.7}$$

with

$$\mu_{n;k,l} = \frac{R_{\text{L}}^k R_{\text{M}}^l R_{\text{R}}^{n-k-l}}{I_{\text{tot},n}} \tag{C.8}$$

With that we can write the sum in (C.5) as

$$\ln \sum_{i=1}^{3^n} \mu_i^q = \tag{C.9}$$

$$\ln \sum_{k=0}^{n} \sum_{l=0}^{n-k} \frac{\binom{n}{k,l} \left(R_{\text{L}}^k R_{\text{M}}^l R_{\text{R}}^{n-k-l}\right)^q}{(R_{\text{L}} + R_{\text{M}} + R_{\text{R}})^{nq}} = \tag{C.10}$$

$$\ln \frac{\left(R_{\text{L}}^q + R_{\text{M}}^q + R_{\text{R}}^q\right)^n}{(R_{\text{L}} + R_{\text{M}} + R_{\text{R}})^{nq}} = \tag{C.11}$$

$$n \ln \frac{\left(R_{\text{L}}^q + R_{\text{M}}^q + R_{\text{R}}^q\right)}{(R_{\text{L}} + R_{\text{M}} + R_{\text{R}})^q} \tag{C.12}$$

Thus we obtain for d_q

$$d_q = \frac{1}{1-q} \lim_{n\to\infty} \frac{n \ln \frac{\left(R_{\text{L}}^q + R_{\text{M}}^q + R_{\text{R}}^q\right)}{(R_{\text{L}} + R_{\text{M}} + R_{\text{R}})^q}}{n \ln 3}. \tag{C.13}$$

This is independent of n so we can drop the limit and get

$$d_q = \frac{\ln \frac{\left(R_{\text{L}}^q + R_{\text{M}}^q + R_{\text{R}}^q\right)}{(R_{\text{L}} + R_{\text{M}} + R_{\text{R}})^q}}{(1-q) \ln 3}. \tag{C.14}$$

The limit $q \to 1$ can be obtained using L'Hôpital's rule.

$$d_1 := \lim_{q\to 1} \frac{1}{1-q} \frac{\ln \sum_{i=1}^{3^n} \mu_i^q}{n \ln 3}$$

$$\Rightarrow d_1 = \frac{\ln (R_{\text{L}} + R_{\text{M}} + R_{\text{R}})}{\ln 3} \tag{C.15}$$

$$- \frac{R_{\text{L}} \ln R_{\text{L}} + R_{\text{M}} \ln R_{\text{M}} + R_{\text{R}} \ln R_{\text{R}}}{(R_{\text{L}} + R_{\text{M}} + R_{\text{R}}) \ln(3)}.$$

Asymptotically d_q goes to

$$\lim_{q\to\infty} d_q = \frac{\ln (R_{\text{L}} + R_{\text{M}} + R_{\text{R}}) - \ln (R_{\text{max}})}{\ln 3}, \tag{C.16}$$

where $R_{\text{max}} := \max \{R_{\text{L}}, R_{\text{M}}, R_{\text{R}}\}$.

Appendix D

Additional notes on the Sampling in Quantum Maps

D.1 Derivation of Expected Value

Starting from the general equation (6.9) for the expected number of accepted boxes here we show how to arrive at the formula for the baker map (6.11).

The i-th box is found with a probability $p_i = 1 - (1 - \mu_i)^S$. Analogous to (C.8) we can restrict ourselves to *different* boxes and define $p_{n:k,l} := 1 - (1 - \mu_{n;k,l})^S$. The expected value of the number of found boxes is

$$\mathrm{E}\left[N_b\right] = \sum_{i=1}^{3^n} p_i = \sum_{k=0}^{n} \sum_{l=0}^{n-k} \binom{n}{k,l} p_{n;k,l}. \tag{D.1}$$

Plugging in the expression for $\mu_{n;k,l}$ we get

$$\mathrm{E}\left[N_b\right] = \tag{D.2}$$
$$\sum_{k=0}^{n} \sum_{l=0}^{n-k} \binom{n}{k,l} \left(1 - \left(1 - \frac{R_\mathrm{L}^k R_\mathrm{M}^l R_\mathrm{R}^{n-k-l}}{(R_\mathrm{L} + R_\mathrm{M} + R_\mathrm{R})^n}\right)^S\right).$$

Equation (6.11) follows from setting $R_\mathrm{L,R} = 1$, $R_M = R$, carrying out the inner sum, and renaming the indices.

D.2 Discussion of Alternatives to Sampling

Here we want to show that taking into account only the regions of phase-space with the highest measures by a cutoff in the measure can not reproduce the scaling observed in the quantum maps.

First, let us consider a fixed cutoff. In this case it is easy to see that for any value of $\mu_{\text{cutoff}} = const.$ there exists a n^* with

$$\mu_{n;k,l} < \mu_{\text{cutoff}}, \ \forall n > n^*.$$

Therefore $d_0 \xrightarrow{n \to \infty} 0$.

The second case is an n-dependent cutoff value $\mu_{\text{cutoff},n} = \frac{I_{\text{cutoff}}}{I_{\text{tot},n}}$ with constant I_{cutoff}. In this case if all $R_{\text{L,M,R}} < 1$ there also exists a n^* with $\mu_{n;k,l} < \mu_{\text{cutoff},n}, \ \forall n > n^*$. In other words: $d_0 \xrightarrow{n \to \infty} 0$. An exception here arises if $R_{\text{L,R}} = 1$ and $R_{\text{M}} \in [0,1)$. Then, for all $0 < I_{\text{cutoff}} < 1$ after a number of iterations n^* all middle thirds fall below the cutoff $d_0 \xrightarrow{n \to \infty} \ln 2/\ln 3$ from above.

So, by associating the number of long-lived eigenstates of boxes above a given threshold we obtain an effective dimension contradicting our numerical observations. This indicates that the (large) regions with low measure μ still contain substantial portions of the eigenstates.

The third alternative we want to discuss is the case where each box contributes to the long-living phase-space volume proportionally to its intensity

$$p_{n;k,l} \propto I_{n;k,l} = \mu_{n;k,l} I_{\text{tot},n}. \tag{D.3}$$

As before we identify $M = 3^n$. In this context we need to limit the contribution of each box $p_{n;k,l} = \min\{1, \alpha I_{n;k,l}\}$ and compute $\text{E}[N_b] = \sum_{k=0}^{n} \sum_{l=0}^{n-k} \binom{n}{k,l} p_{n:k,l}$. The factor α plays a similar role as the cutoff in the sense that for $\alpha \to \infty$ ($\alpha \to 0$) we count all (zero) boxes. This method reproduces the correct scalings in the cases $R_{\text{L,M,R}} = 1$, and $R_{\text{L,R}} = 1, R_{\text{M}} = 0$. However, it fails to reproduce the increase of the effective dimension with R and M and the oscillating behaviour of d_{loc} with $|\nu|_{\text{cutoff}}$.

Bibliography

[AFM$^+$08] E. G. Altmann, T. Friedrich, A. E. Motter, H. Kantz, and A. Richter. Prevalence of marginally unstable periodic orbits in chaotic billiards. *Physical Review E*, 77(1):016205, 2008.

[AHLM07] K. B. Athreya, J. M. Hitchcock, J. H. Lutz, and E. Mayordomo. Effective strong dimension in algorithmic information and computational complexity. *SIAM Journal on Computing*, 37(3):671–705, 2007.

[AK07] E. G. Altmann and H. Kantz. Hypothesis of strong chaos and anomalous diffusion in coupled symplectic maps. *Europhysics Letters (EPL)*, 78(1):10008, 2007.

[ALV12] E. G. Altmann, J. C. Leitão, and J. Viana Lopes. Effect of noise in open chaotic billiards. *Chaos: An Interdisciplinary Journal of Nonlinear Science*, 22(2):026114, 2012.

[AMK05] E. G. Altmann, A. E. Motter, and H. Kantz. Stickiness in mushroom billiards. *Chaos: An Interdisciplinary Journal of Nonlinear Science*, 15(3):033105, 2005.

[AOCO95] T. M. Antonsen, E. Ott, Q. Chen, and R. N. Oerter. Statistics of wavefunction scars. *Physical Review E*, 51(1):111–121, 1995.

[APT13a] E. G. Altmann, J. S. E. Portela, and T. Tél. Chaotic systems with absorption. *Physical Review Letters*, 111(14):144101, 2013.

[APT13b] E. G. Altmann, J. S. E. Portela, and T. Tél. Leaking chaotic systems. *Reviews of Modern Physics*, 85(2):869–918, 2013.

[AS81] J. E. Avron and B. Simon. Almost periodic hill's equation and the rings of saturn. *Physical Review Letters*, 46(17):1166–1168, 1981.

[AS09] A. Akaishi and A. Shudo. Accumulation of unstable periodic orbits and the stickiness in the two-dimensional piecewise linear map. *Physical Review E*, 80(6):066211, 2009.

[AVS09] J. Aguirre, R. Viana, and M. Sanjuán. Fractal structures in nonlinear dynamics. *Reviews of Modern Physics*, 81(1):333–386, 2009.

[Bäc03] A. Bäcker. Numerical aspects of eigenvalue and eigenfunction computations for chaotic quantum systems. In *The Mathematical Aspects of Quantum Maps*, pages 91–144. Springer Berlin Heidelberg, 2003.

[BAE13] T. Bódai, E. G. Altmann, and A. Endler. Stochastic perturbations in open chaotic systems: Random versus noisy maps. *Physical Review E*, 87(4):042902, 2013.

[Ber81] M. V. Berry. Regularity and chaos in classical mechanics, illustrated by three deformations of a circular 'billiard'. *European Journal of Physics*, 2(2):91–102, 1981.

[BGOB88] S. Bleher, C. Grebogi, E. Ott, and R. Brown. Fractal boundaries for exit in hamiltonian dynamics. *Physical Review A*, 38(2):930–938, 1988.

[BOPG07] A. Bueno-Orovio and V. M. Pérez-García. Enhanced box and prism assisted algorithms for computing the correlation dimension. *Chaos, Solitons & Fractals*, 34(2):509–518, 2007.

[BS78] G. Benettin and J. M. Strelcyn. Numerical experiments on the free motion of a point mass moving in a plane convex region: Stochastic transition and entropy. *Physical Review A*, 17(2):773–785, 1978.

[BV89] N. L. Balazs and A. Voros. The quantized baker's transformation. *Annals of Physics*, 190(1):1–31, 1989.

[BVA12] L. A. Bunimovich and L. V. Vela-Arevalo. Many faces of stickiness in hamiltonian systems. *Chaos: An Interdisciplinary Journal of Nonlinear Science*, 22(2):026103, 2012.

[CH94] A. G. Constantine and P. Hall. Characterizing surface smoothness via estimation of effective fractal dimension. *Journal of the Royal Statistical Society. Series B (Methodological)*, 56(1):97–113, 1994.

[CKP+14] P. Charbonneau, J. Kurchan, G. Parisi, P. Urbani, and F. Zamponi. Fractal free energy landscapes in structural glasses. *Nature Communications*, 5:3725, 2014.

[CM06] N. Chernov and R. Markarian. *Chaotic Billiards*. Mathematical surveys and monographs. American Mathematical Society, 2006.

[CMS97] G. Casati, G. Maspero, and D. L. Shepelyansky. Quantum fractal eigenstates. *Physica D: Nonlinear Phenomena*, 131(1-4):3, 1997.

[Cor00] A. Corana. Adaptive box-assisted algorithm for correlation-dimension estimation. *Physical Review E*, 62(6):7872–7881, 2000.

[CS84] B. V. Chirikov and D. L. Shepelyansky. Correlation properties of dynamical chaos in hamiltonian systems. *Physica D: Nonlinear Phenomena*, 13(3):395–400, 1984.

[CW15] H. Cao and J. Wiersig. Dielectric microcavities: Model systems for wave chaos and non-hermitian physics. *Reviews of Modern Physics*, 87(1):61–111, 2015.

[DB01] H. R. Dullin and A. Bäcker. About ergodicity in the family of limaçon billiards. *Nonlinearity*, 14(6):1673–1687, 2001.

[DFJ00] M. Dellnitz, G. Froyland, and O. Junge. The algorithms behind gaio - set oriented numerical methods for dynamical systems. In *Ergodic theory, analysis, and efficient simulation of dynamical systems*, pages 145–174. Springer, 2000.

[DG09] C. P. Dettmann and O. Georgiou. Survival probability for the stadium billiard. *Physica D: Nonlinear Phenomena*, 238(23-24):2395–2403, 2009.

[DG11a] C. P. Dettmann and O. Georgiou. Open mushrooms: stickiness revisited. *Journal of Physics A: Mathematical and Theoretical*, 44(19):195102, 2011.

[DG11b] C. P. Dettmann and O. Georgiou. Transmission and reflection in the stadium billiard: Time-dependent asymmetric transport. *Physical Review E*, 83(3):036212, 2011.

[DG12] C. P. Dettmann and O. Georgiou. Quantifying intermittency in the open drivebelt billiard. *Chaos: An Interdisciplinary Journal of Nonlinear Science*, 22(2):026113, 2012.

[dMdA95] M. B. de Matos and A. M. O. de Almeida. Quantization of anosov maps. *Annals of Physics*, 237(1):46–65, 1995.

[dMG01] A. P. S. de Moura and C. Grebogi. Output functions and fractal dimensions in dynamical systems. *Physical Review Letters*, 86(13):2778–2781, 2001.

[DR15] B. Dietz and A. Richter. Quantum and wave dynamical chaos in superconducting microwave billiards. *Chaos: An Interdisciplinary Journal of Nonlinear Science*, 25(9):097601, 2015.

[DS92] E. Doron and U. Smilansky. Chaotic spectroscopy. *Chaos: An Interdisciplinary Journal of Nonlinear Science*, 2(1):117, 1992.

[EM08] F. Evers and A. D. Mirlin. Anderson transitions. *Reviews of Modern Physics*, 80(4):1355–1417, 2008.

[FKYY83] P. Frederickson, J. L. Kaplan, E. D. Yorke, and J. A. Yorke. The liapunov dimension of strange attractors. *Journal of Differential Equations*, 49(2):185–207, 1983.

[Fot05] A. Fotios. Definitions of deterministic chaos. Master's thesis, Queen Mary University of London, 2005.

[FRS94] A. J. Fendrik, A. M. F. Rivas, and M. J. Sánchez. Decay of quasibounded classical hamiltonian systems and their internal dynamics. *Physical Review E*, 50(3):1948–1958, 1994.

[FSM01] R. M. Füchslin, Y. Shen, and P. F. Meier. An efficient algorithm to determine fractal dimensions of point sets. *Physics Letters A*, 285(1-2):69–75, 2001.

[GD95] P. Gaspard and J. R. Dorfman. Chaotic scattering theory, thermodynamic formalism, and transport coefficients. *Physical Review E*, 52(4):3525–3552, 1995.

[GOPY84] C. Grebogi, E. Ott, S. Pelikan, and J. A. Yorke. Strange attractors that are not chaotic. *Physica D: Nonlinear Phenomena*, 13(1-2):261–268, 1984.

[GOY82] C. Grebogi, E. Ott, and J. A. Yorke. Chaotic attractors in crisis. *Physical Review Letters*, 48(22):1507–1510, 1982.

[GOY83] C. Grebogi, E. Ott, and J. A. Yorke. Fractal basin boundaries, long-lived chaotic transients, and unstable-unstable pair bifurcation. *Physical Review Letters*, 51(10):942–942, 1983.

[GP83] P. Grassberger and I. Procaccia. Measuring the strangeness of strange attractors. *Physica D: Nonlinear Phenomena*, 9(1-2):189–208, 1983.

[Gra88] P. Grassberger. Finite sample corrections to entropy and dimension estimates. *Physics Letters A*, 128(6-7):369–373, 1988.

[Gra90] P. Grassberger. An optimized box-assisted algorithm for fractal dimensions. *Physics Letters A*, vol.148(1-2):63–68, 1990.

[GWSP82] H. S. Greenside, A. Wolf, J. Swift, and T. Pignataro. Impracticality of a box-counting algorithm for calculating the dimensionality of strange attractors. *Physical Review A*, 25(6):3453–3456, 1982.

[HJK$^+$86a] T. C. Halsey, M. H. Jensen, L. P. Kadanoff, I. Procaccia, and B. I. Shraiman. Erratum: Fractal measures and their singularities: The characterization of strange sets [phys. rev. a 33 , 1141 (1986)]. *Physical Review A*, 34(2):1601–1601, 1986.

[HJK$^+$86b] T. C. Halsey, M. H. Jensen, L. P. Kadanoff, I. Procaccia, and B. I. Shraiman. Fractal measures and their singularities: The characterization of strange sets. *Physical Review A*, 33(2):1141–1151, 1986.

[HP83] H. G. E. Hentschel and I. Procaccia. The infinite number of generalized dimensions of fractals and strange attractors. *Physica D: Nonlinear Phenomena*, 8(3):435–444, 1983.

[HRO02] J. P. Haskell, M. E. Ritchie, and H. Olff. Fractal geometry predicts varying body size scaling relationships for mammal and bird home ranges. *Nature*, 418(6897):527–530, 2002.

[IAG$^+$99] P. C. Ivanov, L. A. Amaral, A. L. Goldberger, S. Havlin, M. G. Rosenblum, Z. R. Struzik, and H. E. Stanley. Multifractality in human heartbeat dynamics. *Nature*, 399(6735):461–5, 1999.

[IM06] V. S. Ilchenko and A. B. Matsko. Optical resonators with whispering-gallery modes-part ii: applications. *IEEE Journal of Selected Topics in Quantum Electronics*, 12(1):15–32, 2006.

[JT91] C. Jung and T. Tél. Dimension and escape rate of chaotic scattering from classical and semiclassical cross section data. *Journal of Physics A: Mathematical and General*, 24(12):2793–2805, 1991.

[KG85] H. Kantz and P. Grassberger. Repellers, semi-attractors, and long-lived chaotic transients. *Physica D: Nonlinear Phenomena*, 17(1):75–86, 1985.

[KL01]   Z. Kaufmann and H. Lustfeld. Comparison of averages of flows and maps. *Physical Review E*, 64(5):055206, 2001.

[KMBK13]   M. J. Körber, M. Michler, A. Bäcker, and R. Ketzmerick. Hierarchical fractal weyl laws for chaotic resonance states in open mixed systems. *Physical Review Letters*, 111(11):114102, 2013.

[KNPS06]   J. P. Keating, M. Novaes, S. D. Prado, and M. Sieber. Semiclassical structure of chaotic resonance eigenfunctions. *Physical Review Letters*, 97(15):150406, 2006.

[Kuz00]   S. P. Kuznetsov. Disheveled arnold's cat and the problem of quantum-classic correspondence. *Physica D: Nonlinear Phenomena*, 137(3-4):205–227, 2000.

[LFO91]   Y.-T. Lau, J. M. Finn, and E. Ott. Fractal dimension in nonhyperbolic chaotic scattering. *Physical Review Letters*, 66(8):978–981, 1991.

[LKK+15]   J. F. Lindner, V. Kohar, B. Kia, M. Hippke, J. G. Learned, and W. L. Ditto. Strange nonchaotic stars. *Physical Review Letters*, 114(5):054101, 2015.

[LS90]   O. Legrand and D. Sornette. Test of sabine's reverberation time in ergodic auditoriums within geometrical acoustics. *The Journal of the Acoustical Society of America*, 88(2):865–870, 1990.

[LSZ03]   W. Lu, S. Sridhar, and M. Zworski. Fractal weyl laws for chaotic open systems. *Physical Review Letters*, 91(15):1–4, 2003.

[LT89]   L. S. Liebovitch and T. Toth. A fast algorithm to determine fractal dimensions by box counting. *Physics Letters A*, 141(8-9):386–390, 1989.

[LT11]   Y.-C. Lai and T. Tél. *Transient Chaos*. Springer New York, 2011.

[Lut05]   J. H. Lutz. Effective fractal dimensions. *Mathematical Logic Quarterly*, 51(1):62–72, 2005.

[LVA13]   J. C. Leitão, J. M. Viana Parente Lopes, and E. G. Altmann. Monte carlo sampling in fractal landscapes. *Physical Review Letters*, 110(22):220601, 2013.

[MA84]   D. M. Mark and P. B. Aronson. Scale-dependent fractal dimensions of topographic surfaces: An empirical investigation, with applications in geomorphology and computer mapping. *Journal of the International Association for Mathematical Geology*, 16(7):671–683, 1984.

[Man67]   B. Mandelbrot. How long is the coast of britain? statistical self-similarity and fractional dimension. *Science*, 156(3775):636–638, 1967.

[Man04]   B. B. Mandelbrot. *Fractals and Chaos*. Springer New York, 2004.

[MdMGK05]   A. E. Motter, A. P. S. de Moura, C. Grebogi, and H. Kantz. Effective dynamics in hamiltonian systems with mixed phase space. *Physical Review E*, 71(3):1–5, 2005.

[Mei92] J. D. Meiss. Symplectic maps, variational principles, and transport. *Reviews of Modern Physics*, 64(3):795–848, 1992.

[MGMGG10] J. Martin, I. García-Mata, O. Giraud, and B. Georgeot. Multifractal wave functions of simple quantum maps. *Physical Review E*, 82(4):046206, 2010.

[MLCVHÁ02] F. Martínez-López, M. A. Cabrerizo-Vílchez, and R. Hidalgo-Álvarez. A study of the different methods usually employed to compute the fractal dimension. *Physica A: Statistical Mechanics and its Applications*, 311(3-4):411–428, 2002.

[MLG03] A. E. Motter, Y.-C. Lai, and C. Grebogi. Reactive dynamics of inertial particles in nonhyperbolic chaotic flows. *Physical Review E*, 68(5):056307, 2003.

[MLS93] F. Mortessagne, O. Legrand, and D. Sornette. Transient chaos in room acoustics. *Chaos: An Interdisciplinary Journal of Nonlinear Science*, 3(4):529, 1993.

[MO85] J. D. Meiss and E. Ott. Markov-tree model of intrinsic transport in hamiltonian systems. *Physical Review Letters*, 55(25):2741–2744, 1985.

[MO86] J. D. Meiss and E. Ott. Markov tree model of transport in area-preserving maps. *Physica D: Nonlinear Phenomena*, 20(2-3):387–402, 1986.

[MSKB⁺03] R. A. Méndez-Sánchez, U. Kuhl, M. Barth, C. H. Lewenkopf, and H.-J. Stöckmann. Distribution of reflection coefficients in absorbing chaotic microwave cavities. *Physical Review Letters*, 91(17):174102, 2003.

[NKL⁺07] J. Nagler, M. Krieger, M. Linke, J. Schönke, and J. Wiersig. Leaking billiards. *Physical Review E*, 75(4):046204, 2007.

[NOA96] A. Namenson, E. Ott, and T. M. Antonsen. Fractal dimension fluctuations for snapshot attractors of random maps. *Physical Review E*, 53(3):2287–2291, 1996.

[Nov13] M. Novaes. Resonances in open quantum maps. *Journal of Physics A: Mathematical and Theoretical*, 46(14):143001, 2013.

[NS08] S. Nonnenmacher and E. Schenck. Resonance distribution in open quantum chaotic systems. *Physical Review E*, 78(4):045202, 2008.

[OSA⁺93] E. Ott, J. Sommerer, J. Alexander, I. Kan, and J. A. Yorke. Scaling behavior of chaotic systems with riddled basins. *Physical Review Letters*, 71(25):4134–4137, 1993.

[Ott02] E. Ott. *Chaos in Dynamical Systems Second edition*. Cambridge University Press, 2002.

[Ott08] E. Ott. Attractor dimensions. *Scholarpedia*, 3(3):2110, 2008.

[Ozo90] A. M. Ozorio de Almeida. *Hamiltonian Systems: Chaos and Quantization*. Cambridge University Press, 1990.

[Pfe84]   P. Pfeifer. Fractal dimension as working tool for surface-roughness problems. *Applications of Surface Science*, 18(1-2):146–164, 1984.

[PWCN12] J. M. Pedrosa, D. Wisniacki, G. G. Carlo, and M. Novaes. Short periodic orbit approach to resonances and the fractal weyl law. *Physical Review E*, 85(3):1–5, 2012.

[PY79]   G. Pianigiani and J. A. Yorke. Expanding maps on sets which are almost invariant. decay and chaos. *Transactions of the American Mathematical Society*, 252:351–351, 1979.

[Rén55]   Alfréd Rényi. On a new axiomatic theory of probability. *Acta Mathematica Academiae Scientiarum Hungaricae*, 6(3-4):285–335, 1955.

[Ric99]   A. Richter. Playing billiards with microwaves - quantum manifestations of classical chaos. In *Emerging Applications of Number Theory*, pages 479–523. Springer, 1999.

[Rob83]   M. Robnik. Classical dynamics of a family of billiards with analytic boundaries. *Journal of Physics A: Mathematical and General*, 16(17):014, 1983.

[RPBF09] J. A. Ramilowski, S. D. Prado, F. Borondo, and D. Farrelly. Fractal weyl law behavior in an open hamiltonian system. *Physical Review E*, 80(5):1–4, 2009.

[RT71]   D. Ruelle and F. Takens. On the nature of turbulence. *Communications in Mathematical Physics*, 20(3):167–192, 1971.

[SA15]   M. Schönwetter and E. G. Altmann. Quantum signatures of classical multifractal measures. *Physical Review E*, 91(1):012919, 2015.

[SHF+11] S. Shinohara, T. Harayama, T. Fukushima, M. Hentschel, S. Sunada, and Evgenii E. Narimanov. Chaos-assisted emission from asymmetric resonant cavity microlasers. *Physical Review A*, 83(5):053837, 2011.

[SHW+09] S. Shinohara, M. Hentschel, J. Wiersig, T. Sasaki, and T. Harayama. Ray-wave correspondence in limaçon-shaped semiconductor microcavities. *Physical Review A*, 80(3):031801, 2009.

[SM14]   G. Schehr and S. N. Majumdar. Exact record and order statistics of random walks via first-passage ideas. In *First-Passage Phenomena and Their Applications*, pages 226–251. World Scientific, 2014.

[Sor98]   D. Sornette. Discrete-scale invariance and complex dimensions. *Physics Reports*, 297(5):239–270, 1998.

[SSFH16] S. Sunada, S. Shinohara, T. Fukushima, and T. Harayama. Signature of wave chaos in spectral characteristics of microcavity lasers. *Physical Review Letters*, 116(20):203903, 2016.

[ST04]   H. Schomerus and J. Tworzydło. Quantum-to-classical crossover of quasibound states in open quantum systems. *Physical Review Letters*, 93(15):1–4, 2004.

[Stö99]   H.-J. Stöckmann. *Quantum Chaos: An Introduction.* Cambridge University Press, 1999.

[Sto10]   A. D. Stone. Nonlinear dynamics: Chaotic billiard lasers. *Nature*, 465(7299):696–697, 2010.

[Str94]   S. H. Strogatz. *Nonlinear dynamics and chaos, with applications to physics, biology, chemistry, and engineering.* Westview Press, 1994.

[Tél15]   T. Tél. The joy of transient chaos. *Chaos: An Interdisciplinary Journal of Nonlinear Science*, 25(9):097619, 2015.

[TG06]   T. Tél and M. Gruiz. *Chaotic Dynamics: An Introduction Based on Classical Mechanics.* Cambridge University Press, 2006.

[The86]   J. Theiler. Spurious dimension from correlation algorithms applied to limited time-series data. *Physical Review A*, 34(3):2427–2432, 1986.

[The87]   J. Theiler. Efficient algorithm for estimating the correlation dimension from a set of discrete points. *Physical Review A*, 36(9):4456–4462, 1987.

[The90]   J. Theiler. Estimating fractal dimension. *Journal of the Optical Society of America A*, 7(6):1055, 1990.

[VGL$^+$15]   B. E. Varga, W. Gao, K. L. Laurik, E. Tátrai, M. Simó, G. M. Somfai, and D. Cabrera DeBuc. Investigating tissue optical properties and texture descriptors of the retina in patients with multiple sclerosis. *PLOS ONE*, 10(11):e0143711, 2015.

[WBK$^+$14]   T. Weich, S. Barkhofen, U. Kuhl, C. Poli, and H. Schomerus. Formation and interaction of resonance chains in the open three-disk system. *New Journal of Physics*, 16(3):033029, 2014.

[WC08]   D. Wisniacki and G. G. Carlo. Scarring in open quantum systems. *Physical Review E*, 77(4):45201, 2008.

[Wes99]   G. B. West. The fourth dimension of life: Fractal geometry and allometric scaling of organisms. *Science*, 284(5420):1677–1679, 1999.

[WH06]   J. Wiersig and M. Hentschel. Unidirectional light emission from high- q modes in optical microcavities. *Physical Review A*, 73(3):031802, 2006.

[WHK02]   M. Weiss, L. Hufnagel, and R. Ketzmerick. Universal power-law decay in hamiltonian systems? *Physical Review Letters*, 89(23):239401, 2002.

[WHK03]   M. Weiss, L. Hufnagel, and R. Ketzmerick. Can simple renormalization theories describe the trapping of chaotic trajectories in mixed systems? *Physical Review E*, 67(4):046209, 2003.

[WM08]   J. Wiersig and J. Main. Fractal weyl law for chaotic microcavities: Fresnel's laws imply multifractal scattering. *Physical Review E*, 77(3):036205, 2008.

[Zaa10]   J. Zaanen. High-temperature superconductivity: The benefit of fractal dirt. *Nature*, 466(7308):825–827, 2010.

[Zas02]   G. Zaslavsky. Chaos, fractional kinetics, and anomalous transport. *Physics Reports*, 371(6):461–580, 2002.

Acknowledgements

First of all I want to thank Eduardo Altmann for supervising the research that lead to this thesis, for all the interesting discussions, and for all the encouragement and insightful suggestions he provided while at the same letting me have so much freedom to develop and follow my own ideas. But the athmosphere in our research group would not have been so inspiring and friendly if it were not for my fellow PhD students Jorge, José, and Martin, and all the postdocs and guests that worked with us over the time of my stay here.

Furthermore, I want to thank Roland Ketzmerick, Arnd Bäcker and all the other members of the Computational Physics Group and the members of the Center for Dynamics at TU Dresden with whom I had the pleasure to discuss and who provided me with a lot of fruitful input.

I also want to thank all my colleages at the Max Planck institute for the physics of complex systems. It is a really pleasant place to work at.

And of course I want to thank Anna for taking the step of coming to Dresden with me and for being so supportive all the time.

Erklärung

Diese Arbeit wurde am Max-Planck-Institut für Physik komplexer Systeme unter der wissenschaftlichen Betreuung von Prof. Dr. Roland Ketzmerick durchgeführt.

Hiermit versichere ich, dass ich die vorliegende Arbeit ohne unzulässige Hilfe Dritter und ohne Benutzung anderer als der angegebenen Hilfsmittel angefertigt habe; die aus fremden Quellen direkt oder indirekt übernommenen Gedanken sind als solche kenntlich gemacht. Die Arbeit wurde bisher weder im Inland noch im Ausland in gleicher oder ähnlicher Form einer anderen Prüfungsbehörde vorgelegt.

Ich erkenne die Promotionsordnung der Fakultät Mathematik und Naturwissenschaften der Technischen Universität Dresden vom 23. Februar 2011 an.

Dresden, den

(Moritz Schönwetter)